

Complex dynamics of Physical, Biological and Socio-Economical systems.

Víctor Martínez Eguíluz
Departament de Física
Universitat de les Illes Balears

5 de octubre de 1999

Memoria presentada por
Víctor Martínez Eguíluz para optar
al grado de Doctor en Ciencias Físicas
por la Universidad de las Islas Baleares.

La presente Tesis ha sido dirigida
por los Doctores *Emilio Hernández García* y *Oreste Piro*.

A mi pequeña familia
por su inmensa paciencia.

Contents

Resumen	xi
Abstract	xiii
1 Introducción	1
2 Essential nonlinearities in hearing	17
2.1 Introduction.	18
2.2 Periodically forced Hopf oscillator.	20
2.3 Physiological justification.	23
2.4 Conclusions.	24
3 ‘Sausage-String’ Patterns in Blood Vessels at High Blood Pressures	25
3.1 Introduction	26
3.2 Cylindrical blood vessels	29
3.3 Conclusions	38
4 Frozen spatial chaos induced by boundaries	41
4.1 Introduction	42
4.2 A reaction-diffusion equation in a strip-shaped domain	43
4.3 Single-transverse-mode approximation	48
4.4 Numerical STMA and two-dimensional time-integrations	53
4.5 Conclusions	56
5 Time averages of spatio-temporal chaos: a boundary effect	59
5.1 Introduction	60
5.2 Previous results	62
5.2.1 Faraday waves.	63
5.2.2 Experimental observations	68
5.3 Time averages on the Kuramoto-Sivashinsky equation	71
5.3.1 The Kuramoto-Sivashinsky equation.	71
5.3.2 Results.	74
5.3.3 Discussion and conclusion.	77

6	Boundary Effects in The Complex Ginzburg-Landau Equation	83
6.1	Introduction	84
6.2	Boundary effects	85
6.3	Conclusions	90
7	Self-organized evolution in financial systems.	93
7.1	Introduction.	94
7.2	Evolution of agent's information network.	95
7.3	The model.	96
7.4	Price dynamics.	96
7.5	Discussion.	99
	Appendix A: Numerical simulations in arbitrary domains	103
	Bibliography	107

Emilio Hernández García, profesor titular de la Universidad de las Islas Baleares,
y Oreste Piro, profesor asociado extranjero permanente de la misma Universidad,

CERTIFICAN

que la presente memoria ha sido realizada por Víctor Martínez Eguíluz bajo su
dirección en este departamento y que constituye su Tesis para optar al título de
Doctor en Ciencias Físicas.

Y, para que conste, firman la presente en Palma de Mallorca a 14 de octubre
de 1999.

Emilio Hernández García

Oreste Piro

Agradecimientos

Empezaré por el principio, o casi ...

Y el principio fue una cuestión de azar. Por ello mi primer agradecimiento es para todo ese grupo de personas que, como se suele decir, confiaron en mis posibilidades. Supongo que para quien elige puede que no haya muchas diferencias, al fin y al cabo elige, sin embargo desde la otra perspectiva de aspirante todo se ve de otra forma. Espero que su elección haya sido tan edificante, en todos sus aspectos, como para mí. En cualquier caso ha sido una experiencia que se la recomiendo a quien esté dispuesto a coger un avión y vivir a casi 40 grados en verano. En este punto quiero dedicar un agradecimiento especial a los dos directores que han sabido dirigir mi trabajo dándome suficiente libertad para saciar mi curiosidad. espero que el resultado haya colmado en parte sus expectativas.

De los numerosos viajes que he tenido la suerte de realizar, guardo un gratísimo recuerdo de todos ellos ya que me han dado la oportunidad de conocer gente, maneras de pensar y lugares, absolutamnete distintos a lo que uno está acostumbrado. En este aspecto, destacaría especialmente a todos los argentinos que me acogieron durante mis meses de exilio.

Son muchas las situaciones que se dan durante cuatro años. Una gran parte de todo ese tiempo la he pasado en una gran sala donde, muchas veces, más de veinte personas tienen que convivir y trabajar, sin más barreras que las paredes exteriores. En este clima, lejos, muy lejos del ideal, en el que los sonidos se propagan sin barreras por toda la sala, sin embargo el ambiente creado por sus habitantes ha sido tal que me he hecho olvidar las restricciones física y me han hecho sentir muy a gusto en él. Es por ello que les doy un agradecimiento sincero a todos los compañeros que compartieron el mismo lugar de trabajo e hicieron que los minutos pasaran con más facilidad.

Casi para acabar, y por ello lo más importante, y aunque se merece un libro entero, tendré que limitarme a unas líneas, mi agradecimiento más especial a la persona que me ha tenido que aguantar (y espero que lo siga haciendo por muchos años) antes y durante la realización de esta Tesis. A la persona que ha sufrido mis cansancios, que ha sacrificado sus días para tener sólo las noches..., a ella va dedicado todo el trabajo.

Resumen

En esta Tesis estudio distintos aspectos de la Ciencia No Lineal, concentrándome en aplicaciones en otros campos paralelos a la Física. El hilo conductor de este trabajo es el tipo de bifurcaciones que aparecen en cada uno de los sistemas estudiados.

En el Capítulo 2 estudio dinámicamente el comportamiento de las células ciliadas de la cóclea (oído interno) encargadas de la transducción de las ondas sonoras en impulsos nerviosos. Presento propiedades universales de osciladores muy cerca de una *bifurcación de Hopf* que explican comportamientos observados experimentalmente. En particular muestro que las curvas de respuesta en amplitud de un oscilador forzado periódicamente presentan las mismas características que las curvas de sensibilidad de nuestro sistema auditivo. En el Capítulo 3, explico mediante el mecanismo de una *bifurcación de Turing* la formación de una estructura en forma de salchichas que aparecen al aumentar la presión sanguínea en arteriolas. Dicha estructura aparece como una inestabilidad debida a la relación no lineal entre la tensión y el desplazamiento de las paredes de los vasos sanguíneos. En el marco de sistemas no lineales extendidos con algún tipo de desorden, el Capítulo 4 está dedicado a la formación de estructuras desordenadas espacialmente pero estacionarias en tiempo, comúnmente llamadas *caos espacial*. Aunque dichas estructuras se han encontrado con anterioridad en otros contextos, la originalidad de nuestro trabajo radica en que es la primera vez que se muestra un ejemplo en que la aparición de caos espacial es inducida por la forma del dominio y las condiciones de contorno. En el Capítulo 5, estudio sistemas caóticos tanto espacial como temporalmente en dominios acotados. La ecuación de Kuramoto-Sivashinsky, que es un sistema modelo de comportamiento caótico, en un dominio acotado y con condiciones de contorno distintas de periódicas muestra promedios temporales estructurados similares a los encontrados experimentalmente. Cambiando las condiciones de contorno veo que el promedio también cambia y se ajusta a la simetría global del problema, es decir a las simetrías de las ecuaciones de evolución y de las condiciones de contorno. El Capítulo 6, está dedicado a la ecuación compleja de Ginzburg-Landau, una ecuación modelo de sistema extendido con una gran riqueza de regímenes dinámicos. Estudiando este sistema en contornos cuadrados, circulares y en forma de estadio se ven nuevas soluciones como es el caso de soluciones tipo diana, que difícilmente se ven en el caso sin contornos. Finalmente, el Capítulo 7 está dedicado al estudio de un sistema dinámico de muchos componentes en interacción. Se propone un modelo para la formación de grupos de opinión en mercados financieros que presenta cualitativamente varias propiedades encontradas empíricamente en dichos mercados.

Abstract

In this Thesis, I study different aspects of Nonlinear Science, focusing on applications to other fields parallel to Physics. The common thread through this work is the type of bifurcations that appear in each studied system.

In Chapter 2, I study the dynamical behavior of the hair cells in the cochlea (inner ear). These cells are responsible of the transduction of sound pressure waves into nervous impulses. I investigate the universal properties of oscillators in the vicinity of a *Hopf bifurcation* to explain the behavior observed experimentally. In particular, I show that the amplitude-response curves of periodically forced oscillators have the same characteristics as the sensitivity curves of our auditory system. In Chapter 3, I present a mechanism that explains via a *Turing bifurcation* the formation of a ‘sausage-string’ pattern that appears when increasing the arterial pressure in small blood vessels. This structure appears as an instability due to the nonlinear stress-strain relation of the blood vessel walls. In the context of extended dynamical systems with some kind of disordered behavior, Chapter 4 is dedicated to the formation of disordered structures in space but stationary in time, the so called *spatial chaos*. Although frozen spatial chaos has been previously observed in other contexts, our work is the first to show an example where its appearance is a consequence of the shape of the domain and the boundary conditions. In Chapter 5, I study spatio-temporally chaotic systems in bounded domains. A generic system displaying a chaotic regime in a domain with boundary conditions other than periodic gives rise to a structured time-averaged pattern similar to the ones experimentally observed. Changing the boundary conditions, I find that the average also changes adjusting to the global symmetry of the problem, including both the evolution equations and the boundary conditions. Chapter 6 is dedicated to the complex Ginzburg-Landau equation that is a model equation of extended dynamical system with a great wealth of dynamical regimes. Studying this system in square, circular and stadium-like shaped domains there appear solutions like targets, that are difficult to obtain without these contours. Finally, Chapter 7 is dedicated to the study of dynamical systems with many interacting components. In particular, I propose a model for the formation of opinion groups in a financial market. The model displays several qualitative properties empirically found in real markets.

Capítulo 1

Introducción

Durante muchos años la ciencia ha seguido una ruta hacia la especialización, en donde los investigadores son capaces de entender hasta los últimos detalles de una parcela muy pequeña dentro de un subcampo restringido en un campo mucho más extenso. Con esta filosofía son muchos los avances que se han producido en este final de siglo y los resultados obtenidos auguran un futuro donde los avances tecnológicos moldearán la forma de relacionarse en la sociedad. A pesar de todas estas virtudes, también es cierto que cada vez es más difícil la interacción entre investigadores de distintos campos, e incluso a veces entre investigadores del mismo campo pero distintas especialidades. Esta división en parcelas de la Ciencia tiene como inconveniente la dificultad en el trasvase de conocimientos entre campos lo que hace que a veces se tengan que redescubrir problemas ya resueltos. Como una pequeña muestra de lo fértil que puede llegar a ser la interacción entre diversas disciplinas científicas, en esta Tesis presentamos aplicaciones de lo que se suele llamar Ciencia No lineal en Física, Biología y sistemas complejos en Socio-Economía.

Presentación.

Cualquier persona que haya puesto a hervir un puchero de agua se habrá percatado que el agua que estaba en reposo sobre el fuego empieza a moverse a medida que se calienta. Esta sencilla observación de que aumentado una magnitud externa (en este caso dando calor al agua) se produce un cambio cualitativo en el estado del sistema (en este caso el agua en reposo empieza a moverse) puede extenderse a muchos otros sistemas. Un físico utiliza el concepto de *bifurcación*: una solución que es estable se desestabiliza cuando el valor de un parámetro supera cierta cantidad, denominada umbral. Normalmente con la pérdida de estabilidad viene asociado el nacimiento de nuevas soluciones. El tipo de bifurcaciones que pueden sufrir soluciones homogéneas y estacionarias han sido clasificadas y existen ecuaciones modelo que las describen.

Una primera división que podemos hacer es entre sistemas con dependencia espacial, llamados *sistemas dinámicos extendidos espacialmente*, y los que no tienen dependencia espacial, denominados *sistemas de baja dimensión*. Las soluciones más simples de un sistema sin dependencia espacial son puntos fijos, soluciones cuyo valor no varía en el tiempo. Si pensamos en la temperatura de un punto en una habitación, veremos que variará en tiempo, más alta de día y más baja de noche. Una temperatura fija correspondería a una solución punto fijo. Situaciones un poco más complicadas son las periódicas, en el que el valor en un instante dado es el mismo un período más tarde. Si P es el período, T la temperatura y t el tiempo, las soluciones periódicas cumplen: $T(t + P) = T(t)$. En el ejemplo anterior el período podría ser $P = 1$ día y la temperatura se repetiría al día siguiente. Situaciones más complicadas pueden ocurrir, e.g. soluciones cuasi-periódicas, llegando a situaciones caóticas en el que las soluciones no están sujetas a ningún patrón, aun siguiendo ecuaciones deterministas.

Sistemas extendidos pueden presentar como soluciones más sencillas las soluciones homogéneas estacionarias, i.e. soluciones independientes del espacio y del tiempo. Si $A = A(\mathbf{x}, t)$ es un campo con dependencia espacial y temporal, $A = a_0$, donde a_0 es una constante representa una solución homogénea estacionaria. En el ejemplo de la temperatura, corresponde a una situación en el que la temperatura es la misma en todos los puntos de la habitación y no varía con el tiempo. La presencia de la dependencia espacial permite la aparición de soluciones periódicas en espacio pero estacionarias en tiempo, que cumplen $A(x, t) = A(x + L, t)$, para todo t y donde L es el período espacial. Soluciones mucho más complicadas pueden aparecer, como por ejemplo soluciones oscilatorias y espacio-temporalmente caóticas.

A lo largo de esta Tesis vamos a ir visitando distintos escenarios tomados de la Física, Biología y Socio-Economía, donde el tipo de bifurcación que gobierna su dinámica va aumentando en complejidad. Empezaré por estudiar un sistema puntual, para pasar posteriormente a estudiar sistemas extendidos, desde una bifurcación de Turing a regímenes espacio-temporalmente caóticos, y finalizar con un modelo de agentes que se caracteriza por presentar una transición para la distribución de grupos.

En lo que queda de Sección presentaré un resumen de los temas que se desarrollan posteriormente en los Capítulos 2-7. En el Capítulo 2, empezaré por presentar un ejemplo de oscilador cerca de una *bifurcación de Hopf* y su aplicación en el estudio del funcionamiento del sistema auditivo. Los siguientes capítulos tratarán sobre sistemas

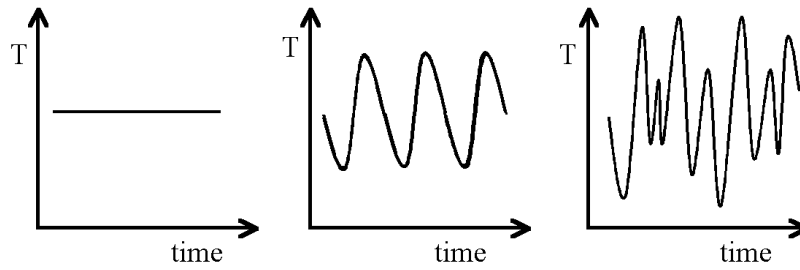


Figura 1.1: Ejemplos sencillos de evolución de una magnitud. De izquierda a derecha: soluciones estacionaria, periódica y desordenada.

extendidos espacialmente y donde las condiciones de contorno pueden llegar a tener un papel importante. En primer lugar en el Capítulo 3, presento una explicación de un fenómeno de formación de estructuras en forma de salchichas en arteriolas en términos de un *bifurcación de Turing*. Dentro de sistemas extendidos que presentan algún tipo de desorden, de un lado el estudio de soluciones desordenadas espacialmente pero estacionarias en tiempo se estudian en el Capítulo 4. En él, las estructuras aparecen debido a las condiciones de contorno y geometría del dominio de integración. Por otro lado, comportamientos muy desordenados pueden dar promedios temporales no triviales cuando el sistema se encuentra en un dominio finito como se muestra en el Capítulo 5. Para finalizar el estudio de sistemas extendidos, en el Capítulo 6 se presenta un trabajo sobre la interacción de espirales con los contornos en un sistema auto-oscilante. Finalmente, el Capítulo 7 está dedicado a los llamados *sistemas complejos*: sistemas dinámicos de muchos componentes en interacción. En particular propongo un modelo para la formación de grupos de opinión en un sistema financiero que presenta cualitativamente algunas propiedades encontradas empíricamente en mercados financieros. Dependiendo del valor de los parámetros, dicho modelo presenta una bifurcación en la distribución de grupos.

El oído como sistema dinámico

El oído constituye un ejemplo de miniaturización y precisión llevado a cabo por la evolución. En humanos, es capaz de funcionar entre los 20 Hz y los 20 kHz, y funcionar correctamente hasta intensidades que van desde 0 dB (*umbral de audición*) a los 140 dB, es decir, es capaz de trabajar en 7 órdenes de magnitud de intensidad (Fig. (1.2)). El viaje del sonido en los diferentes órganos del oído acaba en el oído interno y más concretamente en la *cóclea* (Fig. (1.3)). La *cóclea* es un órgano en forma de caracol cuyo interior está separado por una membrana llamada *membrana basilar*. Dicha membrana oscila dependiendo del movimiento del fluido que hay en su interior que a su vez se mueve impulsado por el sonido que le ha llegado al tímpano. Dentro de la membrana basilar se hayan las células responsables de la transducción de las ondas de presión que es el sonido a impulsos nerviosos para que el cerebro los manipule. Dichas células se llaman *células ciliadas*. Su forma está esquematizada en la Fig. (1.4). El cuerpo de la célula está en contacto con los axones de las células nerviosas que codifican y mandan la información al cerebro. También pueden servir para que el cerebro mande señales y controle el movimiento del manojito de cilios. El manojito de cilios se mueve con el movimiento de la membrana basilar y su movimiento desencadena un flujo de iones que produce que el potencial de membrana varíe, su variación hace que se expulsen neurotransmisores y éstos a su vez son recogidos por las células nerviosas que producen los impulsos nerviosos. De esta descripción tan rudimentaria del funcionamiento del oído interno, podemos sacar la conclusión que el conocimiento de cómo funcionan las células ciliadas es fundamental para tener un conocimiento claro del funcionamiento global del oído.

Si extendemos la *cóclea* a lo largo como una regla, podemos asignar a cada punto una *frecuencia característica*, es la frecuencia a la cual resuena dicho punto de la *cóclea* cuando el oído es expuesto a un tono puro de la misma frecuencia. Así, las frecuencias se ordenan en orden decreciente desde la parte más cercana al exterior (altas frecuencias) hasta el centro del caracol (bajas frecuencias).

Modelos recientes [3] sugieren que las células ciliadas se comportan dinámicamente como osciladores cerca de una *bifurcación de Hopf*. Una bifurcación de Hopf es la bifurcación que ocurre cuando un punto fijo estable pierde su estabilidad y aparece una nueva solución oscilatoria. Un ejemplo sencillo de oscilador es un reloj de péndulo. El mecanismo de un reloj de péndulo consiste en unas pesas que suministran energía al péndulo a medida que éste la va necesitando, de tal forma que la trayectoria que describe el reloj de péndulo es un *ciclo límite*, que se caracteriza por tener un período y una amplitud de oscilación del péndulo bien definida, independiente de la condición inicial. Incluso si le damos un empujón (o lo frenamos un poco) el período volverá a ser el mismo después de unas oscilaciones transitorias. Los osciladores lineales no tienen este comportamiento: la amplitud de oscilación depende del impulso inicial. La independencia de la amplitud de oscilación es un efecto de la presencia de términos no lineales en las ecuaciones de movimiento¹. Volviendo a nuestro reloj de péndulo, si

¹Existen otros tipos de osciladores no lineales que no presentan ciclos límites (i.e. órbitas periódicas atractivas). Por ejemplo los sistemas conservativos presentan familias continuas de órbitas periódicas estables que no atraen a las trayectorias vecinas. Sin embargo, estos ejemplos no son

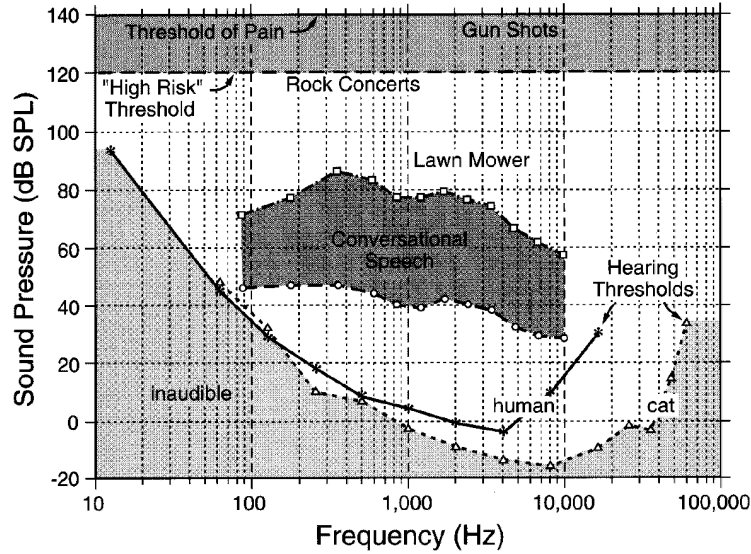


Figura 1.2: Gráfica que muestra niveles de presión de sonido y frecuencia de los tonos relevantes para la audición para la mayoría de mamíferos, en particular humanos y gatos. Sólo aquellos tonos cuyos parámetros caen por encima de la curva del “umbral de audición” son audibles. El rango de parámetros que comprende la conversación normal en inglés [1] está marcada en la zona sombreada. De [2]

mientras oscila le quitamos una pesa veremos que lentamente se irá disminuyendo la amplitud de oscilación hasta pararse. Cualquier perturbación que le demos al sistema hará que éste oscile por un momento y volverá a pararse. Parece interesante estudiar la respuesta de este tipo de osciladores cuando están sometidos a un forzamiento externo periódico a una frecuencia ω . La respuesta en frecuencia, es decir, cuándo el sistema es capaz de seguir la frecuencia externa en función de la amplitud y frecuencia de forzado, da lugar a lo que se conoce como *lenguas de Arnold* que son regiones en las que el oscilador sigue al forzado.

Desde un punto de vista del sistema auditivo es muy interesante saber cuál es la respuesta del sistema en amplitud, es decir, cuál es la relación entre la amplitud de forzado y la de respuesta del sistema, que corresponde en el caso del oído a estudiar la respuesta del sistema auditivo (por ejemplo intensidad nerviosa) en función de la intensidad del sonido. Se ha encontrado experimentalmente que la respuesta de las células ciliadas a distintas intensidades del sonido (amplitud del forzado) está caracterizado por una compresión no-lineal. Dicha compresión se puede entender desde otro punto de vista: la ganancia en respuesta para intensidades pequeñas es mucho más grande que para intensidades grandes lo que da un comportamiento saturado para amplitudes intermedias. Este comportamiento no se puede explicar con un oscilador (lineal o no-lineal) de relajación rápida sometido a un forzado externo, porque la respuesta es lineal con la intensidad. Otros efectos que se observan son: sintonización

relevantes en el estudio de sistemas disipativos fuera del equilibrio.

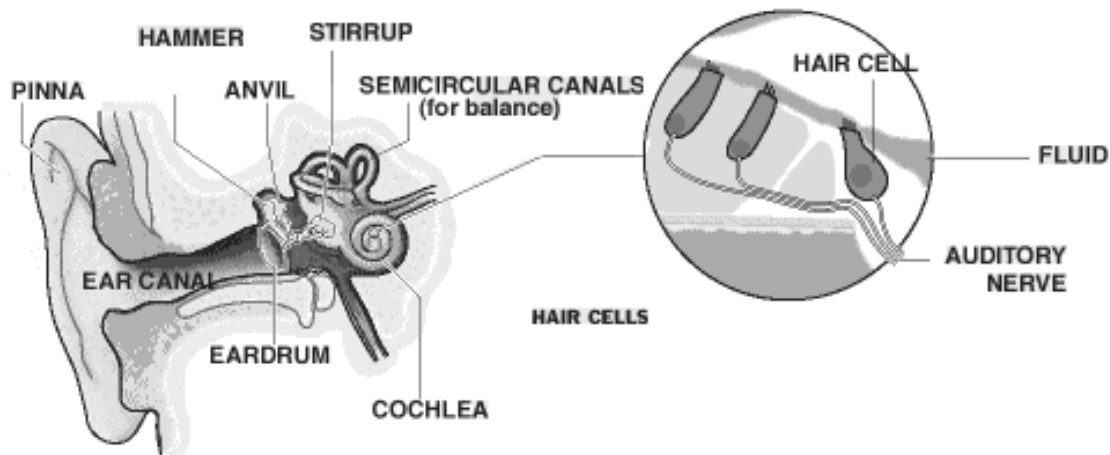


Figura 1.3: El oído externo (*pinna*) dirige el sonido dentro del canal (*ear canal*). El sonido viaja hasta el tímpano (*eardrum*) haciéndolo vibrar, transmitiendo el movimiento al oído interno. Mediante una serie de huesecillos, la vibración se transmite finalmente al interior de la cóclea. Dentro de la cóclea están las células sensitivas llamadas células ciliadas (*hair cells*). Cuando el fluido del interior de la cóclea se mueve, la membrana situada en la base de las células ciliadas también se mueve. Distinta cantidad de movimiento en distintas posiciones de la membrana corresponde a diferentes frecuencias del sonido. Estos movimientos hacen que las células ciliadas se muevan a su vez produciendo señales que eventualmente alcanzan el cerebro a través del nervio auditivo (*auditory nerve*) para ser interpretados como sonidos.

muy fina para señal nula y generación de tonos de combinación.

Nuestra propuesta para explicar las propiedades del sistema auditivo: compresión del régimen dinámico, sintonización muy fina para amplitud nula y generación de tonos de combinación, se basa en la observación de que si el comportamiento de las células ciliadas se describe como un sistema dinámico próximo a una bifurcación de Hopf, se permite una fuerte ganancia cuando el sistema está forzado con bajas intensidades. El mecanismo por el cual se produce dicha amplificación fue ya sugerido por Gold [4] en 1948 y se denomina *regeneración*.

El mecanismo propuesto en este trabajo encaja con otros modelos recientes. Por ejemplo, en [3] proponen un modelo tal que variando los parámetros dentro de los márgenes fisiológicos permite estar en una situación anterior o posterior a la bifurcación, es decir, cuyo comportamiento en reposo es de punto fijo u oscilante. Esto concuerda con nuestra hipótesis en que la vecindad de una Hopf es un lugar que permite gran ganancia para pequeñas intensidades de estímulo. Por otro lado recientes estudios [5] sugieren que propiedades no-lineales son capaces de explicar experimentos psicofónicos sin necesidad de recurrir a elementos más sofisticados de nuestro cerebro como el cortex.

En resumen, en el Capítulo 2, se estudia un modelo que describe el comportamien-

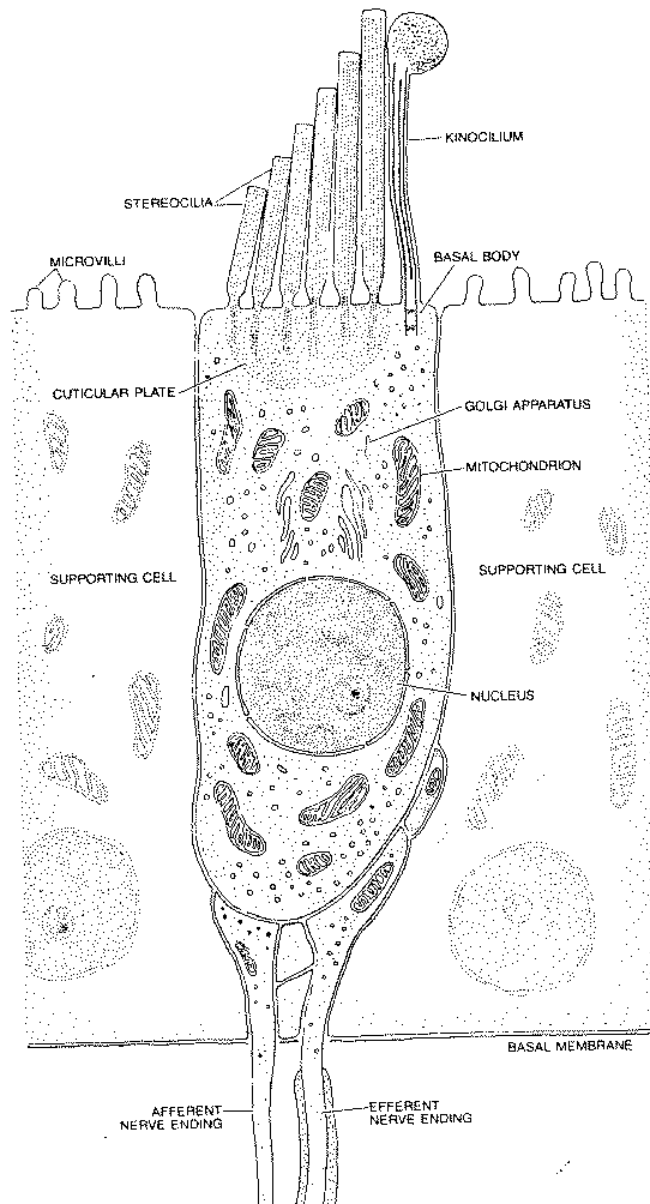


Figura 1.4: Corte transversal de una célula ciliada. La célula es generalmente cilíndrica o en forma de ampolla. Aunque están relacionadas con las células nerviosas, las células ciliadas no tienen dendritas ni axones. La organización del ramo de cilios varía entre especies en sus detalles pero su estructura general es la misma en todos los vertebrados. A lo largo de un eje hay un progresivo incremento de la longitud del estereocilio. Sin embargo, a lo largo del eje perpendicular los estereocilios tienen la misma longitud. Como resultado, el ramo de cilios tiene un plano de simetría; la ilustración es una sección a lo largo de dicho plano. El kinocilio está situado en el plano de simetría en el lado más alto del cono. Los nervios aferentes que terminan en la superficie basal de la célula transmiten la respuesta del receptor al cerebro. De [6].

to de un sistema cerca de una bifurcación de Hopf sometida a una fuerza periódica, centrándonos en la amplitud de la respuesta. Los resultados encontrados en este modelo se ajustan a los datos experimentales de las curvas de respuesta del oído en mamíferos y da un posible mecanismo para explicar la compresibilidad no lineal encontrada en el oído humano (y de los mamíferos en general). Hemos encontrado que dicho mecanismo se ha utilizado hace muchos años en el diseño de radios para amplificar la señal recibida, denominándose en este contexto *super-regeneración*.

Inestabilidad en arteriolas

Una elevada presión arterial en pequeñas arterias y arteriolas pueden producir un daño importante en el sistema circulatorio. Un aumento de la presión en arteriolas produce primero un estrechamiento de los conductos seguido del desarrollo consecutivo de dilataciones y contracciones, al estilo de una “ristra de chorizos”. Los segmentos dilatados aumentan su permeabilidad a macromoléculas de la sangre con lo que puede llegar a difundir proteínas en las paredes de los conductos.

La forma asalchichada que presentan las arteriolas sometidas a alta presión es un ejemplo de estructura periódica. Se puede definir un tamaño típico como la distancia promedio entre contracciones, y se suele denominar *longitud de onda*. Abstrayéndonos de elementos fisiológicos, lo que ocurre no parece ser muy distinto del ejemplo que mostraba al inicio de esta presentación en el caso del agua al irse calentado empezaba a agitarse. En este caso, un aumento en la presión (parámetro externo) produce que el sistema que inicialmente presentaba un estado “trivial” de reposo, se inestabilice dando lugar a la aparición de una nueva estructura. Las características particulares de esta bifurcación, i.e. que la forma espacial no varía en el tiempo pero con una longitud de onda típica, se denomina *bifurcación de Turing*. Para caracterizar la bifurcación de una solución homogénea estacionaria, tenemos que saber si la estructura nueva que aparece tiene longitud de onda cero o distinta de cero, y si oscila o no. A veces en vez de usar longitudes de onda se utiliza *vectores de onda* que esencialmente son el inverso de la longitud de onda. Si λ es la longitud de onda y k su vector de onda, $k = 2\pi/\lambda$. También se suele utilizar la frecuencia $\omega = 2\pi/T$, siendo T el período de oscilación. En otras palabras, una bifurcación de Turing se caracteriza por $k \neq 0$ y $\omega = 0$.

Nosotros proponemos un modelo sencillo para un fluido en un canal cilíndrico cuyas paredes tiene características no lineales en la relación esfuerzo-deformación. Este modelo dinámico sencillo da buena cuenta de la bifurcación cuando varía la presión ejercida sobre el fluido y da una predicción para la longitud típica de las “salchichas”.

Caos espacial inducido por contornos

Hasta este punto hemos presentado comportamientos regulares como son las soluciones periódicas, que vimos con el oscilador para en el oído, y las estacionarias en

tiempo y periódicas en espacio. En ambos casos vimos cómo dicho comportamiento surgía de una inestabilidad de la solución estacionaria (homogénea en el caso de las arteriolas). Sin embargo es bien conocido que comportamientos más complicados también son posibles incluso en sistemas gobernados por ecuaciones deterministas. Uno de los ejemplos más sencillos de comportamiento caótico es el que se da al lanzar una moneda. La moneda puede dar cara o cruz. Si cara lo representamos por 1 y cruz por 0, una serie de lanzamientos corresponderá a una sucesión de ceros y unos. Esta sucesión no tiene orden aparente y ha sido generada por un proceso estocástico (realmente es mecánico). Pues bien, hay sistemas dinámicos deterministas que pueden hacerse corresponder con el ejemplo anterior.

Un sistema dinámico extendido (i.e. con dependencia espacial y temporal) además del desorden temporal también puede presentar desorden espacial. El ejemplo más paradigmático es el de la turbulencia en fluidos. Un caso interesante intermedio entre el caos temporal y el espacio-temporal es el llamado *caos espacial*, en el que el desorden espacial aparece sin desorden temporal. Este tipo de soluciones se situaría, a su vez, entre el *caos Lagrangiano* y el *caos Euleriano*. En el primero, el Lagrangiano, el campo de velocidades del fluido puede presentar un comportamiento ordenado y simple, y sin embargo las trayectorias de las partículas pueden recorrer órbitas caóticas. Esto puede ocurrir en un sistema tridimensional para un campo de velocidades estacionario. Es bien sabido que la mínima dimensionalidad que se necesita para presentar caos es tres. Si escribimos las ecuaciones de movimiento para una partícula en un campo de velocidades estacionario $\mathbf{v}(\mathbf{x}) = (v_x, v_y, v_z)$:

$$\begin{aligned}\dot{x} &= v_x(x, y, z) \\ \dot{y} &= v_y(x, y, z) \\ \dot{z} &= v_z(x, y, z)\end{aligned}\tag{1.1}$$

se ve que algunos campos de velocidades pueden dar lugar a trayectorias caóticas. En dos dimensiones, un campo con dependencia temporal (por ejemplo un campo temporalmente periódico) también puede dar lugar a trayectorias temporalmente caóticas. Caos Euleriano se refiere a que el campo de velocidades es caótico. Así pues, soluciones que presentan un desorden espacial a la vez que estacionarios temporalmente se encontrarían entre los dos tipos de comportamiento señalados anteriormente.

Nuestro interés en el Capítulo 4 está en la búsqueda de soluciones desordenadas en espacio pero estacionarias en el tiempo. En particular, encontraremos una situación en que el desorden espacial viene impuesto por la existencia de condiciones de contorno no periódicas. Es decir, que si cambiamos las condiciones de contorno las estructuras desordenadas desaparecen.

El sistema que estudiamos es del tipo de Fisher-Kolmogorov

$$\psi(x, t) = \nabla^2 \psi + f(\psi) ,$$

donde nosotros estudiamos el caso de $f(\psi) = \psi - \psi^3$ que tomamos como ecuación modelo. Sin dependencia espacial dicha ecuación presenta dos soluciones estables estacionarias $\psi_{\pm} = \pm 1$. Cualquier condición inicial distinta de la nula lleva a una

de las dos. En presencia del término de difusión, el sistema también intenta ordenarse en dos fases, las correspondientes a las soluciones homogéneas ψ_{\pm} , y se forman frentes entre dominios de distintas fases. El tamaño típico de los dominios crece con el tiempo hasta que al final sólo queda una de las fases. Dicha ecuación no presenta estructuras desordenadas estacionarias en sistemas infinitos o con condiciones de contorno periódicas.

Por similitud con forzamientos periódicos en sistemas de baja dimensión tomamos un contorno en forma de canal ondulado, con condiciones de contorno cero en los laterales ondulados. Como nos interesamos por soluciones estacionarias, podemos olvidarnos de la variable temporal. Así nos quedan dos variables espaciales x e y . La idea es interpretar una de las variables espaciales, digamos la x , como la variable temporal. En las ecuaciones, con esta interpretación, queda claro cómo las condiciones de contorno en la dirección y juegan el papel de forzamiento temporal. Siguiendo con el paralelismo, para anchuras pequeñas del canal, podemos hacer aproximaciones a la forma transversal de la solución y llegamos a una ecuación del tipo oscilador forzado paramétrico.

Para un gran rango de parámetros demostramos la aparición de estructuras desordenadas inducidas por la presencia de los contornos.

Mirando un corte longitudinal a las soluciones que aparecen, podemos asociar una sucesión de ψ_{\pm} a cada oscilación en función del valor que tome el campo mayoritariamente en ese período. Si a ψ_{+} le llamamos cara y a ψ_{-} cruz, tenemos el equivalente al ejemplo inicial de la moneda. Podemos generar cualquier sucesión de caras y cruces cambiando la condición inicial. Es por ello que los denominamos soluciones caóticas.

Promedios temporales en sistemas extendidos

Comportamientos más complejos se dan en sistemas *espacio-temporalmente caóticos*, que son sistemas que presentan desorden tanto en su evolución temporal como en las dimensiones espaciales.

Muchos trabajos han sido dedicados a la caracterización, tanto desde un punto de vista experimental como teórico y numérico de dicho régimen. Medidas estadísticas se han utilizado para describir tales sistemas y para comparar resultados experimentales con modelos numéricos. En esta dirección una de las medidas más sencillas de tomar es la de promedios temporales, i.e. asignar a cada punto del espacio el valor del promedio temporal de ese punto. Está claro que con condiciones de contorno periódicas, donde todos los puntos son equivalentes siempre que no haya una rotura espontánea de simetría, asintóticamente el promedio temporal es una función homogénea que toma el mismo valor en todos los puntos. Sin embargo, ¿qué pasa en un sistema real donde no hay condiciones de contorno periódicas?

Un ejemplo ilustrativo del comportamiento que se observa en presencia de contornos se da en el comportamiento de los líquidos cerca de las paredes. Experimentalmente [7] se ha comprobado mediante rayos X, que un líquido cerca de las paredes de su recipiente no es un líquido. Se ha mostrado que cerca del límite sólido-líquido las moléculas del líquido forman capas, parecidas a las que forman algunos cristales

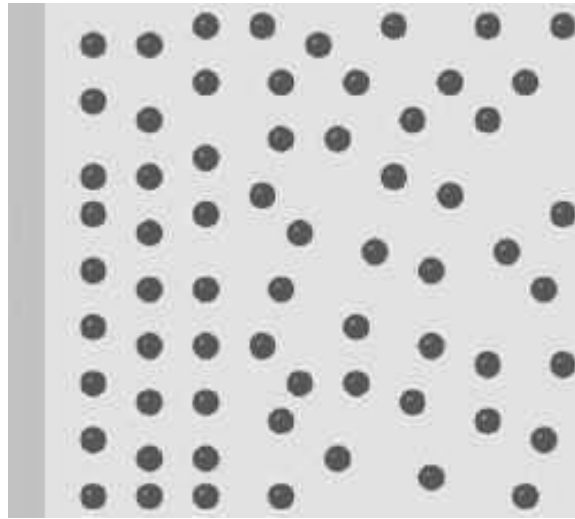


Figura 1.5: Near the surface of a solid, liquid molecules form layers, which have different properties from the liquid as a whole [7].

líquidos (Fig. (1.5)). Simulaciones numéricas de dinámica molecular [8] de fluidos con superficies sólidas muestran también un perfil no trivial para la densidad de partículas como se puede apreciar en la Fig. (1.6).

Ya en el contexto de sistemas macrocópicos no lineales, Gluckman *et al.* [9] realizaron un experimento de ondas de Faraday² en el régimen desordenado donde presentaban una estructura promediada temporalmente. Lejos de tener una forma homogénea, que es lo que se espera con condiciones de contorno periódicas, la estructura promedio presentaba una forma que se asemejaba a la del modo más inestable de la primera bifurcación. A este experimento le siguieron otros en diferentes sistemas. Una de las conclusiones interesantes de dichos experimentos es que en la estructura promedio se recupera la simetría global, es decir, la simetría de las ecuaciones de evolución y las condiciones de contorno. Así se puede apreciar que un experimento de Faraday en un recinto circular da un promedio temporal con simetría circular.

En el Capítulo 5 estudiamos numéricamente la ecuación de Kuramoto-Sivashinsky en una y dos dimensiones, que la tomamos como una ecuación modelo que presenta caos espacio-temporal. Dicha ecuación aparece cuando se estudia la altura de un líquido cayendo por una pared inclinada, frentes de llamas... Importante por lo que se ha dicho anteriormente van a ser las condiciones de contorno, ya que deben ser distintas de las periódicas para romper la invarianza de traslación y que alguna estructura pueda surgir. Vamos a estudiar dos conjuntos de condiciones de contorno distintos que tienen dos simetrías distintas: unas son *pares*, es decir hay una simetría especular por el centro del dominio; otras son *impares*, en el centro del dominio hay un centro de inversión. Vemos que en esas condiciones aparece una estructura no trivial en los

²Un experimento de ondas de Faraday consiste en la agitación vertical controlada de un fluido en un contenedor. Ver Capítulo 5.

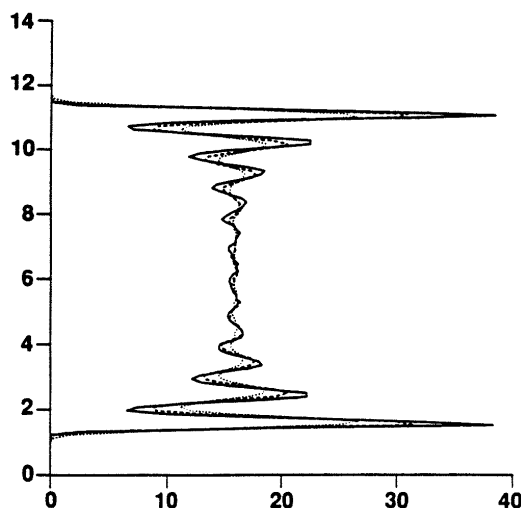


Figura 1.6: El perfil de la densidad promedio (línea continua) de un líquido en equilibrio entre paredes (de [8]). Las paredes están situadas en $y = 0$ and 14 . En el eje horizontal se representa la densidad promedio.

promedios temporales, como ocurre en los experimentos. Dicha estructura es más pronunciada cerca de los bordes y decae hacia el interior. Somos capaces de definir una longitud de onda típica y vemos que está cuantizada en función de la longitud del sistema.

Defectos, espirales y contornos.

Un sistema paradigmático de la Física No lineal actual es la ecuación compleja de Ginzburg-Landau (CGLE). Su generalidad y riqueza de comportamientos es tal que la cantidad de artículos publicados relacionados en algún aspecto con esta ecuación es enorme. La generalidad le viene porque describe la inestabilidad de un campo homogéneo en una *bifurcación de Hopf*, es decir, cuando se pone a oscilar. Esta es la segunda vez que hablamos de una bifurcación de Hopf, la anterior fue en el Capítulo 2 sobre oído. La diferencia es que ahora estamos estudiando un sistema con dependencia espacial, es decir un conjunto de osciladores acoplados difusiva o dispersivamente.

El interés de estudiar una ecuación tan genérica como la CGLE es doble. Primero, porque describe situaciones similares en sistemas tan aparentemente alejados como flúidos y óptica de láseres, con lo que todo lo que uno consigue aprender de ella puede ser utilizado en distintos casos. Segundo, porque al ser más sencilla que las ecuaciones que describen completamente el sistema permite un análisis teórico más profundo de otra manera inviable. Es por estas razones por la que nos centramos en el estudio numérico de la CGLE.

En una dimensión su diagrama de fases se puede dividir en 4 regiones: una zona de *no caos*, donde las ondas planas son estables, *turbulencia de fase*, *turbulencia de de-*

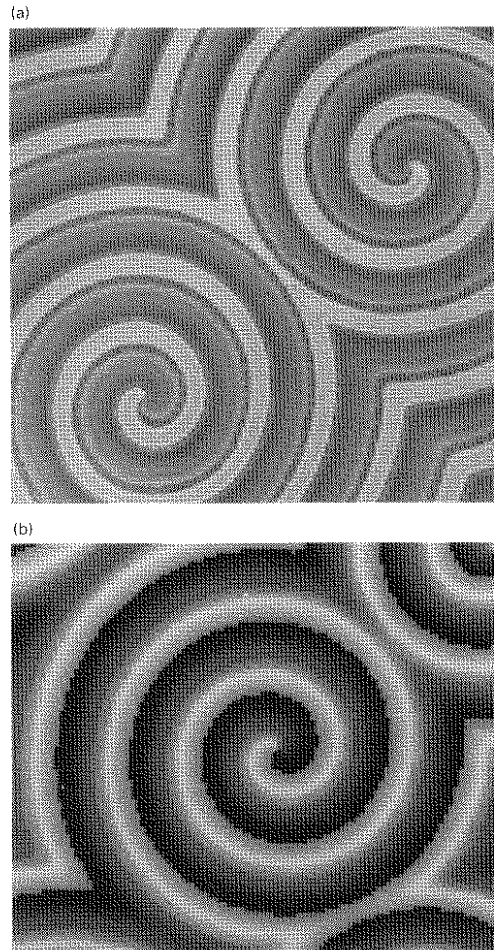


Figura 1.7: Dos ejemplos de espirales en sistemas distintos: (a) Espirales en la reacción de Belousov-Zhabotinsky (sistema excitable). (b) Simulación de la ecuación compleja de Ginzburg-Landau (sistema auto-oscilante). La escala de grises corresponde a la fase del campo complejo. De [10].

fectos, intermitencia espacio-temporal y bicaos. Ejemplos de dichos comportamientos se pueden encontrar en multitud de lugares y no los repetiremos aquí.

En dos dimensiones el comportamiento es un poco más complicado. Además de las fases anteriormente comentadas, tenemos la complicación extra de los defectos topológicos. Los defectos topológicos no pueden desaparecer espontáneamente en dos dimensiones, sino que se deben aniquilar por pares defectos de carga opuesta. Un ejemplo de defectos topológico son las espirales en sistemas auto-oscilantes (Fig. (1.7)). Por lo tanto, siguiendo el comentario anterior, una espiral no puede desaparecer sola espontáneamente sino que debe aniquilarse con otra espiral de carga opuesta. Una consecuencia de esta regla es que en dos dimensiones la carga topológica global se conserva a lo largo de la evolución del sistema y viene determinada por la carga topológica de la condición inicial.

En el Capítulo 6, estudiamos cómo la geometría y las condiciones de contorno influyen en la dinámica de la ecuación compleja de Ginzburg-Landau. En particular, estudiamos dicha ecuación en recintos cuadrados, circulares y de tipo estadio, con condiciones de contorno de Dirichlet, es decir, que el valor del campo complejo se fija en los contornos a cero. En estas circunstancias las paredes pueden comportarse como emisores o sumideros de defectos, y se verá que son fundamentales para entender la dinámica observada. Uno de los fenómenos interesantes que vemos es el papel que juegan las esquinas como directores en la emisión de ondas planas desde las paredes adyacentes. También hemos observado la formación de soluciones tipo *'target'* que no se observan en la Ginzburg-Landau sin forzamiento externo.

Teoría de juegos y redes en Economía.

Para acabar, se presenta un ejemplo de otro tipo de dinámica basada en teoría de juegos con aplicaciones en sistemas financieros. Presento un modelo muy simplificado para la formación de grupos de opinión. Una forma de colocar a los participantes en un mercado financiero, *agentes*, es una red ordenada, por ejemplo una red rectangular bidimensional. Si nuestro interés es el de estudiar la interacción entre agentes cabe preguntarse sobre la validez de suponer una red tan ordenada y estacionaria. En este Capítulo, intentamos plantear una dinámica en el que no hay restricciones en cuanto a la interacción entre agentes: todos pueden, si así lo eligen, interactuar con el resto de agentes. El proceso de transmisión de información entre agentes lo modelo como un proceso de formación de *enlaces*. Así si dos individuos se transmiten información o la comparten, existirá un enlace entre ellos. La formación de enlaces en este modelo es un proceso aleatorio, en cada paso de tiempo, se crea un enlace entre dos cualesquiera agentes del mercado. Mediante este proceso se da una formación de grupos, considerando como tales a todos los individuos que comparten la misma información. Añadiendo a esta dinámica de formación de grupos, otra de poner órdenes de compra y venta de valores del mercado, conseguimos montar un mercado financiero en el que el precio de un valor fluctúa dependiendo de la oferta (venta) y demanda (compra) de los agentes.

El único parámetro de control del sistema es la velocidad de propagación de la información entre agentes. Cuando dicha velocidad es pequeña, la distribución de ganancias sigue una ley de potencias truncada. Si la velocidad es muy rápida, aparecen fluctuaciones muy grandes, llamados *crashes*, debidas a que todo los agentes forman un gran cluster y actúan al unísono. En otras palabras, variando la velocidad de propagación el sistema sufre una bifurcación de un estado subcrítico a uno supercrítico.

En el Capítulo 7 aplicamos este mecanismo al proceso de propagación de información en un mercado financiero. Con este modelo sencillo de mercado conseguimos que haya una distribución libre de escalas, *ley de potencias*, para un amplio rango de tamaños de grupos y de retornos³.

³Se llama retornos a las variaciones del logaritmo del precio.

Conclusiones.

A lo largo de esta Tesis he presentado diferentes aplicaciones en campos colindantes a la Física de los conocimientos adquiridos en el marco de lo que suele llamar Ciencia No-lineal. Hemos visto cómo comportamientos sencillos que se conocían desde hace años en Física tienen una rápida y gratificante aplicación para entender el funcionamiento de sistemas que de otra forma son muy complejos. Así ocurre por ejemplo en las aplicaciones del oído y de las arteriolas. Físicamente son dos bifurcaciones muy sencillas pero modelos sencillos basados en este hecho pueden explicar muchas de las observaciones experimentales y empíricas.

Dinámicas más complicadas, basadas en regímenes caóticos espacial y/o temporalmente, han sido estudiadas fijándose en los efectos que la presencia de una geometría y unas condiciones de contorno distintas de las periódicas produce en la dinámica de sistemas extendidos.

Finalmente se ha presentado otro tipo de sistemas que no vienen dados por ecuaciones evolutivas sino por reglas pero que también presentan bifurcaciones en su comportamiento. Su interés pasa por campos como la Sociología y la Economía pero también pueden pasar por la Biología para entender la interacción de grupos de especies entre ellos.

Chapter 2

Essential nonlinearities in hearing

The individual elements of our hearing organ evidently poise themselves at a Hopf bifurcation to maximize tuning and amplification. We show that in this condition several effects are expected to be generic: compression of the dynamic range, infinitely sharp tuning at zero input, and generation of combination tones. These effects are “essentially” nonlinear in that they become more marked the smaller the forcing: there is no sound soft enough not to evoke them. All the well-documented nonlinear aspects of hearing therefore appear to be consequences of the same underlying mechanism¹.

¹This Chapter corresponds to *Essential nonlinearities in hearing*, by V.M. Eguíluz, M. Ospeck, Y. Choe, A.J. Husdpeth, M.O. Magnasco, submitted for publication (1999).

2.1 Introduction.

The classic Helmholtz theory [11] posits that our hearing organ, the cochlea, is arranged like a harp or the backplane of a piano, with a number of highly tuned elements arrayed along a frequency scale, performing Fourier analysis of the incoming sound. Although the notion that our hearing organ works like a musical instrument offers a beautiful esthetic symmetry, it has serious flaws. In the 1940s, Gold [4] pointed out that the cochlea’s narrow passageways are filled with fluid, which dampens any hope of simple mechanical tuning. He argued that the ear cannot operate as a passive sensor, but that energy must be put into the system. As in the operation of a regenerative receiver², active amplification of the signal can compensate for damping in order to provide highly tuned responses.

Von Békésy’s classic measurements in the cochlea [12] demonstrated the mapping of sound frequencies to positions along the cochlea. He observed the tuning to be quite shallow and found cochlear responses to behave linearly over the range of physiologically relevant sound intensities. Gold’s notions were largely set aside in favor of the hypothesis of coarse mechanical tuning followed by a “second filter”, whose nature was surmised to be electrical.

Von Békésy performed his measurements on cadavers, whose dead cochleas lacked power sources or amplifiers that might have provided positive feedback. Only fairly recently, laser-interferometric velocimetry performed on live and reasonably intact cochleas has led to a very different picture [13, 14, 15]. There is, in fact, sharp mechanical tuning, but it is *essentially nonlinear*: there is no sound soft enough that the cochlear response is linear. Although the response far from the resonance’s center is linear, at the resonance’s peak the response rises sublinearly, compressing 80 dB into 25-30 dB (Fig. (2.1)). The width of the resonance increases with increasing amplitude, being sharpest for sounds near the threshold of hearing. Observation of the essential nonlinearity of the response at the level of cochlear mechanics contradicts von Békésy’s finding. Furthermore, this nonlinearity does not originate in the rigidity of membranes or in fluid-mechanical effects. Because it disappears if the cochlea is deprived of oxygen, the nonlinearity depends on a biological power supply.

Psychoacoustical experiments have provided another means of probing the nonlinearities of hearing. When two sine waves traverse a system with a nonlinear transfer function, the response shows integer linear combinations of the input frequencies, whose amplitudes scale according to products of the input amplitudes raised to the appropriate integer (>1) powers. If the input is weak enough, a linear “small-amplitude” regime is recovered, in which combination tones are absent. Psychoacoustical experiments showed that the perceived intensity of combination tones is not suppressed in this fashion: although the $2f_1 - f_2$ combination tone should be suppressed by 3 dB

²A regenerative radio receiver amplifies by adding just enough positive feedback that the receiver barely oscillates. The design was abandoned because it emits into the very bandwidth it receives. The superregenerative receiver is a self-quenching version; both were invented by Edwin Armstrong, who also invented broad-band FM. Gold conjectured that a regenerative mechanism for hearing could lead to feedback oscillations so that the ear would actually emit sound. The subsequent discovery of spontaneous otoacoustic emissions gave Gold’s theory some notoriety.

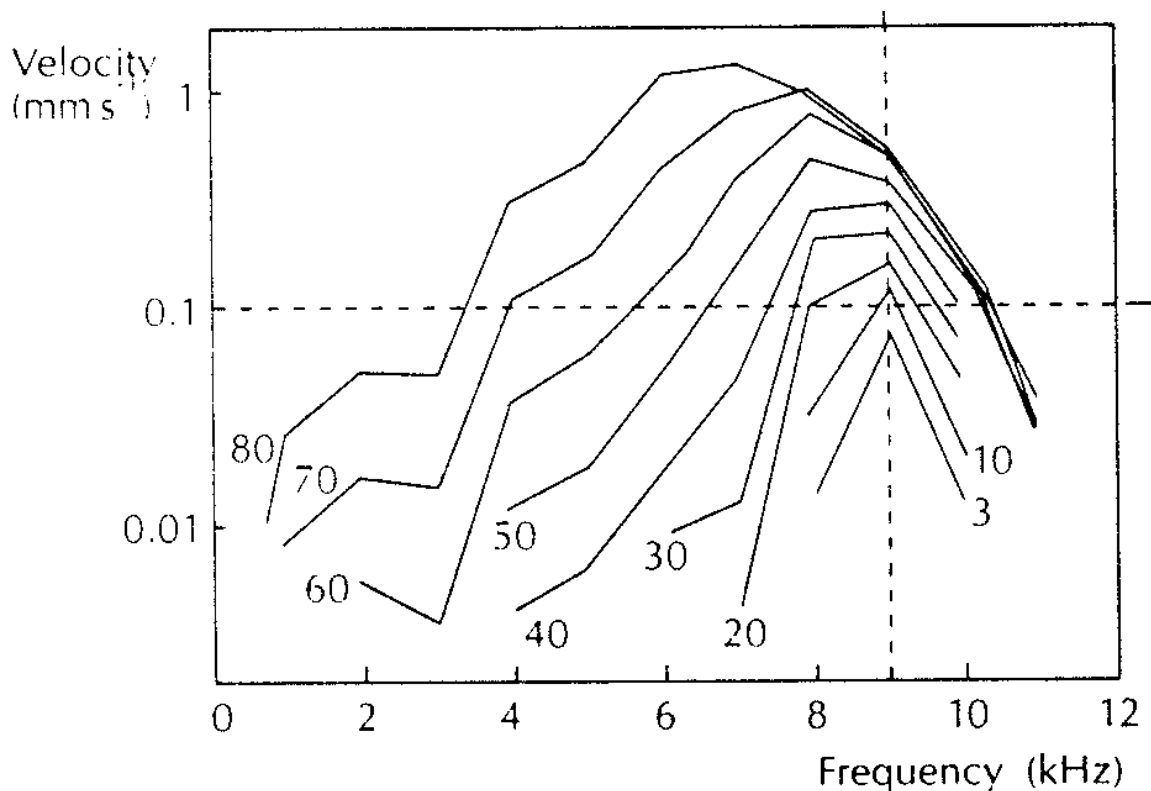


Figure 2.1: Laser velocimetric data from a living chinchilla’s cochlea displaying the root-mean-square velocity of the basal membrane as a function of driving frequency. Each curve represents a different sound level, labelled in decibels sound-pressure level. The “characteristic frequency” at the measured position is 9 kHz. Notice that at 4 kHz, the curves from 40 dB to 80 dB span two decades (40 dB), whereas at 9 kHz the curves from 3 dB to 60 dB span just under one decade (20 dB); at 4 kHz, the response rises an average of 1 dB per decibel, whereas at 9 kHz the response rises only 0.3 dB per decibel. Note furthermore the dramatic increase in bandwidth as the intensity increases. Courtesy of M. A. Ruggero [14].

for each decibel of attenuation in the input sound, the actual attenuation is only 1 dB per decibel [16]. The intensity relative to the fundamental tones remains constant. These observations, too, imply that the system is essentially nonlinear: no sound is faint enough to elicit a small-amplitude, linear regime.

We shall show that all of these apparently disparate characteristics are related to one another, stemming from the same mechanism. In dynamical systems language, we would say that Gold’s theory asserts that the elements of the hearing organ somehow *poise* themselves at a Hopf bifurcation, like a sound technician adjusting the volume at an amplifier to the loudest possible setting before feedback oscillation ensues. We shall show that at a Hopf bifurcation we generically expect essential nonlinearities, compression of dynamic range, sharp tuning for soft input, and broad tuning for loud input. In essence, several nonlinear aspects of hearing may stem from the Hopf bifur-

ation. We shall then argue that it is physiologically plausible that this is occurring, given our current understanding of hair-cell physiology.

2.2 Periodically forced Hopf oscillator.

The cochlea can be roughly approximated by a series of coupled Hopf oscillators with increasing characteristic frequency. A generic equation describing a Hopf bifurcation can be written

$$\dot{z} = (\mu + i\omega_0)z - (1 + i\beta)|z|^2z$$

where $z(t)$ is a complex variable of time, ω_0 is the natural frequency of oscillation, and μ is the control parameter³. For the sake of simplicity we will consider in the following $\beta = 0$. When μ becomes positive, the solution $z \equiv 0$ becomes unstable, and a stable oscillatory solution appears, $z = \sqrt{\mu} \exp(i\omega_0 t)$. If the system is subjected to periodic forcing as $\dot{z} = (\mu + i\omega_0)z - |z|^2z + F e^{i\omega t}$, then for the spontaneously oscillating system a variety of well-studied entrainment behaviors occur. Assuming a 1:1 locked solution of the form $z = R e^{i\omega t + i\phi}$ we obtain

$$F^2 = R^6 - 2\mu R^4 + (\mu^2 + (\omega - \omega_0)^2)R^2 \quad (2.1)$$

This equation is a cubic in R^2 and hence solvable:

$$R^2 = \frac{S^{\frac{1}{3}}}{32^{\frac{1}{3}}} + \frac{\mu}{3} - \frac{2^{\frac{1}{3}}U_2}{3S^{\frac{1}{3}}}$$

where

$$\begin{aligned} S &= D + \sqrt{D^2 + 4U_2^3} & D &= 27F^2 + 16\mu^3 - 18\mu U_1 \\ U_1 &= \mu^2 + (\omega_0 - \omega)^2 & U_2 &= -\mu^2 + 3(\omega_0 - \omega)^2 \end{aligned}$$

If we specialize Eq. (2.1) exactly at the bifurcation we obtain

$$F^2 = R^6 + (\omega - \omega_0)^2 R^2 \quad (2.2)$$

from which we can demonstrate directly one of our main contentions. At the center of the resonance, where $\omega = \omega_0$, $R \approx F^{1/3}$, so no matter how small F might be, the response is nonlinear. Notice that because a cubic root of a small number is much larger than the number, the amplification R/F or the differential amplification dR/dF blows up as $F^{-2/3}$ for infinitesimal forcings. Away from the resonance's center, for sufficiently small F we get $R \approx F/|\omega - \omega_0|$, the standard form for a single pole seen from some distance away: the amplification is constant and independent of F .

The definitions of ‘‘near the resonance’’ and ‘‘far from the resonance’’ depend on the amplitude of the forcing; therefore the interface between the two regimes depends

³Another simple model of the transition in explicit oscillator form can be obtained as a variation of the van der Pol equation: $\ddot{x} + \nu \dot{x}(x^2 - \mu) + \omega^2 x = 0$. Other ‘‘Hopf bifurcations’’ can be constructed with different nonlinearities. If the ODE vector field is to be real analytic, however, then the nonlinearity must be an odd integer; the case we present is generic in this sense. Under different nonlinearities, the specific one-third power law would change, but not our general conclusions.

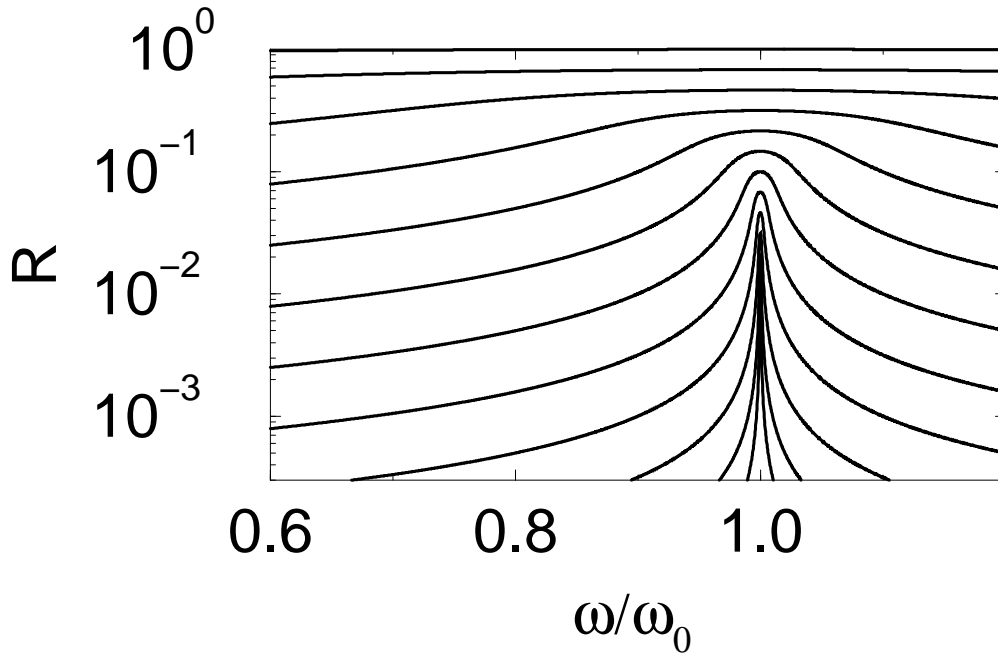


Figure 2.2: Hopf resonance. The response R to different levels of forcing F is obtained from Eq. (2.2). At resonance the response increases as the one-third power of the forcing, while away from the resonance the response is linear in the forcing.

on F . If we define the half-width Γ of the resonance as the range in ω for which R falls by one-half, $(R/2)^6 + \Gamma^2(R/2)^2 = R^6$, from which

$$\Gamma = \frac{3\sqrt{7}}{4} F^{2/3} \quad (2.3)$$

For this system the gain-bandwidth product is constant and independent of the forcing. The gain-bandwidth balance depends strongly on the forcing amplitude, however, asymptoting to infinite gain and zero bandwidth for zero forcing amplitude. This behavior strikingly resembles that of the velocimetric data for the basilar-membrane response [14].

The precision with which the system can be poised near the bifurcation determines the maximal amplification and frequency selectivity. We again specialize Eq. (2.1), this time to the case $\omega = \omega_0$, exactly at resonance, to get

$$F^2 = R^2(R^2 - \mu)^2 \quad (2.4)$$

Consider first $\mu < 0$, the sub-bifurcation regime. As $F \rightarrow 0$ then $R \rightarrow -F/\mu$: the amplification for infinitesimally soft sounds is $-1/\mu$, which becomes infinite only exactly at the transition. Therefore, for μ sufficiently small and negative we observe compressive nonlinearity for $F > (-\mu)^{2/3}$ and a linear regime for softer sounds. We should furthermore note that for Eq. (2.1), μ is also the parameter for exponential relaxation in the absence of forcing: the system relaxes to the quiescent state as $\exp(\mu t)$. Thus

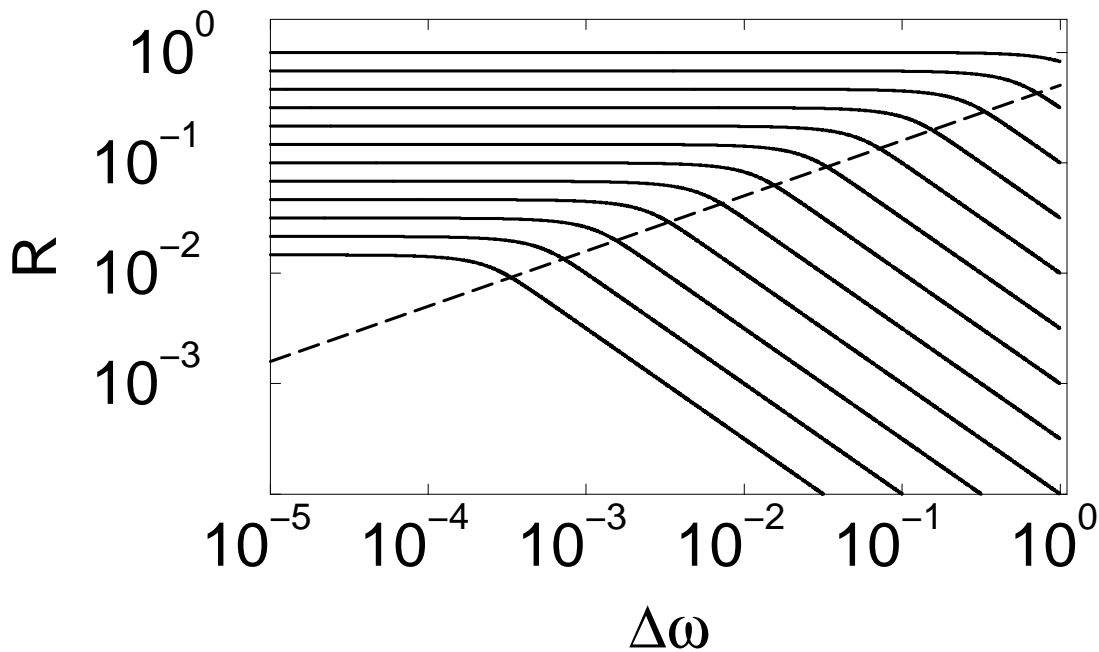


Figure 2.3: The resonance of Fig. (2.2) in log-log form shows the compressive and linear regimes and the boundary between them. The dashed line given by Eq. (2.3) indicates the half-width Γ .

the linear-regime amplification is exactly proportional to the integration time given by this relaxation; this integration time becomes infinite exactly at the bifurcation.

Once past the Hopf bifurcation ($\mu > 0$), an oscillation occurs, for which the response above the limit-cycle amplitude is $R' = R - \sqrt{\mu}$. Eq. (2.4) has three solutions, of which only one ($R' > 0$) is stable with stability parameter 2μ . In the supra-bifurcation regime the solution above is by definition phase-locked 1:1, so its stability is constrained to the 1:1 Arnold tongue. In order to fully explore the behavior of the system around the Hopf bifurcation, it is better to consider the simplest forced model able to suffer quasiperiodic transitions. The best numerical scheme is to define a system whose solution we can compute analytically, then to force it impulsively so that we obtain a closed-form iterated map [17, 18]. The simplest such homogeneous oscillator is

$$\dot{r} = r(\mu - r^2) \quad (2.5)$$

$$\dot{\theta} = \omega, \quad (2.6)$$

Numerical exploration of this model and of the model described in³ shows that the features described above are independent of model details [19].

We have thus established that several nonlinear aspects of hearing are compatible with the idea that individual sound-sensing elements poise themselves at the Hopf transition. We shall now argue that physiological data suggest that this is the case.

2.3 Physiological justification.

Electrical frequency selectivity, in which individual hair cells are tuned to specific frequencies of mechanical stimulation by resonance of the membrane potential [20], suggests a role for Hopf bifurcations in the auditory system. A seven-dimensional conductance-based model describes the hair cell's electrical amplifier, called the membrane oscillator [21, 22]. In this model, the hair-cell's capacitance is charged by a standing current through the transduction channels, then discharged by a Ca^{2+} -activated K^+ current. The model's control parameter μ is a strong function of both the transduction and the Ca^{2+} conductances. As described by the membrane-oscillator model with increased μ , electrically resonant hair cells in the hearing organs of amphibians, reptiles and birds operate near a supercritical Hopf bifurcation. A small conductance oscillation in the transduction channels engenders a large current-to-voltage gain, the benefit of operating near a Hopf bifurcation⁴.

Sharp mechanical frequency selectivity may also emerge from proximity to a Hopf bifurcation. A priori, one may suspect that frequency-specific amplification in the auditory system derives in part from mechanical properties of the hair bundle, the mechanoreceptive organelle of the inner ear. This bundle does not behave as a merely passive transducer. The spontaneous and evoked hair-bundle oscillations observed in hair cells from the turtle's cochlea and the bullfrog's sacculus instead demonstrate that the hair bundle is capable of producing active limit-cycle and high-Q behavior [24, 25, 26]. Two suggestions have been made about the mechanism of these oscillations [27]. Both posit that the force-generating elements regulate the elastic properties of the mechano-electrical transduction channel in a Ca^{2+} -dependent manner, thus modulating tension in the associated gating spring and altering the mechanics of the hair bundle. In support of such a mechanism, the current through the channel displays Ca^{2+} -sensitive oscillations even under conditions in which the membrane potential and hair-bundle position are fixed, and therefore in which the usual means of channel gating is frustrated [28].

One possibility is that myosin molecules anchoring the channel complex to the actin core of the stereocilia power the oscillations. The alternative proposal is that the channel complex itself is intrinsically active and generates force. The primary supposition of this model [3] is that the closed state of the channel is stabilized by Ca^{2+} binding. Because there is a Ca^{2+} concentration gradient across the cell membrane and the channel is permeable to Ca^{2+} , channel opening regulates the local intracellular Ca^{2+} concentration and thus force generation through channel reclosure. This model is represented by an eight-dimensional system in which two mechanical equations are coupled to a six-state Ca^{2+} -binding cycle and chemomechanical forcing

⁴Electroreceptors are thought to represent derivatives of hair cells that have lost mechanical sensitivity. These cells may nonetheless retain the hair cell's strategy of electrical resonance for frequency tuning. The paddlefish, for example, uses electrosensitive ampullary cells to detect electrical activity associated with the swimming motions of water fleas. These cells are sensitive to electric fields as weak as $2 \text{ mV}\cdot\text{m}^{-1}$. The neurons innervating ampullary cells show noisy electrical oscillations at rest; during stimulation the oscillations are synchronized by external electric fields. Ampullary cells thus behave like noisy phase-locked loops [23] and appear to operate near a Hopf bifurcation.

operates through the open probability of the transduction channel.

Variation of parameter values through a physiologically plausible range reveals a locus of Hopf bifurcations whose frequencies span the range of human hearing. Near the bifurcation, one observes compressive frequency selectivity; the system is essentially nonlinear. A particularly relevant control parameter is the number of stereocilia in the hair bundle: many of the mechanical properties may be defined as functions of this number, which is clearly regulated along the cochlea. In agreement with experiment, near the bifurcation locus the model maps tall, thin hair bundles to the low-frequency range and short, broad bundles to higher frequencies. A second control parameter governs Ca^{2+} -binding kinetics; faster transitions correspond to higher oscillation frequencies. Tuning of this parameter may be achieved through modulation of the intracellular Ca^{2+} concentration, which is also subject to tight regulation. This model demonstrates that a biologically reasonable tuning mechanism in the auditory system may operate near a Hopf bifurcation and that proximity to the bifurcation may be tuned by realistic variations in parameter values.

In the mammalian cochlea amplification is thought to be mediated by the phenomenon of electromotility [29, 30]. During stimulation of an outer hair cell, large numbers of intramembrane proteins rapidly respond to changes in transmembrane potential by altering the cell's length. This movement presumably deflects the hair bundle, causes a conductance change and therefore is fed back to the transmembrane potential. To realize the performance attributed to the cochlear amplifier, the electromotility system may also utilize the instability of a Hopf bifurcation.

2.4 Conclusions.

We have shown that some of the characteristic of the hearing organ, as for example the compression of the dynamic range, infinitely sharp tuning at zero input, and generation of combination tones, can be explained with a superregenerative mechanism. We have shown universal properties of an oscillator in the vicinity of a Hopf bifurcation that presents similar features as the hearing organ.

Chapter 3

‘Sausage-String’ Patterns in Blood Vessels at High Blood Pressures

A new Rayleigh-type instability is proposed to explain the ‘sausage-string’ pattern of alternating constrictions and dilatations formed in blood vessels at high blood pressure conditions. Our theory involves the nonlinear stress-strain characteristics of the vessel wall, and provides predictions for the conditions under which the normal cylindrical geometry of a blood vessel becomes unstable. The theory explains key features observed experimentally, e.g. the limited occurrence of the sausage-string pattern to small arteries and large arterioles, and only in those with small wall-to-lumen ratios¹.

¹This Chapter corresponds to *Instability and ‘Sausage-String’ Appearance in Blood Vessels during High Blood Pressure*, by P. Alstrøm, V.M. Eguíluz, M. Colding-Jørgensen, F. Gustafsson, N.-H. Holstein-Rathlou, *Phys. Rev. Lett.* **82**, 1995 (1999), and *‘Sausage-String’ Patterns in Blood Vessels at High Blood Pressures*, by P. Alstrøm, V.M. Eguíluz, M. Colding-Jørgensen, F. Gustafsson, N.-H. Holstein-Rathlou, to appear in *Proceedings of Statistical Mechanics of Biocomplexity*, Springer Verlag (Berlin 1999)

3.1 Introduction

Approximately 10% of the population in Western societies has high blood pressure and roughly half receive pharmacological treatment. Despite the development of potent blood pressure lowering drugs, elevated blood pressure remains a major risk factor for development of stroke and heart disease. While the underlying mechanisms in the vast majority of cases of high blood pressure are unknown, it is clear that high blood pressure is primarily caused by an increase of resistance to blood flow in the circulation. This elevation in resistance to blood flow is induced by an increase in the tone of the small arteries and arterioles (diameter 30-300 μ) by contraction of the smooth muscle cells surrounding the vessels. Smooth muscle cell contraction in arterioles and arteries may be induced by several vasoconstricting agents, one of the most potent being the octapeptide angiotensin II. Standard medication for high blood pressure includes drugs that lower the production or effects of vasoconstricting agents on the vascular smooth muscle cells.

Extreme increase in blood pressure, so-called malignant hypertension, may for example be encountered in patients with a kidney disease or in pregnant women suffering from preeclampsia. The underlying large increase in arterial resistance may be accompanied by severe damage to the circulatory system and result in organ dysfunction, particularly of the kidneys and the brain. This organ dysfunction may be irreversible and even fatal. In almost every case, malignant hypertension is accompanied - or caused - by considerable elevations of the blood levels of angiotensin II [31]. The vascular damage associated with substantial increase in blood pressure is confined to small arteries and arterioles, and it is preceded by a peculiar vascular reaction pattern: Initially extreme uniform narrowing of the blood vessels occurs. This is succeeded by the development of alternating constriction and dilatation, giving the vessel a "sausage-string appearance" (Fig. 3.1). This vascular pattern has been demonstrated in many organs, including the brain, the gut, and the kidney [32] and it is of decisive importance to the subsequent development of vascular damage, since damage to the vascular wall occurs exclusively in the dilated regions of the vessel [33, 34, 35, 36]. In the dilated segments, permeability to macromolecules from the blood stream is increased resulting in diffusion of proteins into the vessel wall. Presumably this in turn leads to local dysfunction and ultimately death of the cells of the vascular wall.

In experimental studies of malignant hypertension in rats, high blood pressure is typically induced by intravenous infusion of angiotensin II [33, 34, 35, 36]. As the infusion is continued, a substantial narrowing of the smaller blood vessels is observed, and at a given contraction, the narrowed vessels develop the sausage-string pattern (Fig. 3.1). Despite several decades of experimental research of the phenomenon, the mechanism causing the 'sausage-string' pattern has remained unknown [32]. It has been suggested that the pattern is caused by a 'blow out' of the vessel wall due to the high blood pressure [37], but this seems unlikely for several reasons. First, as mentioned above, the sausage-string pattern is observed only in the smaller vessels (small arteries and large arterioles), cf. Fig. 3.2, and here the pressure elevation is relatively small compared to that in the larger arteries. Secondly, the phenomenon is



Figure 3.1: *In vivo* micrograph of rat intestinal arterioles showing a typical ‘sausage-string’ pattern following an acute increase in blood pressure induced by intravenous infusion of angiotensin II. The neighboring vessels not showing constrictions and dilatations are the corresponding venules. From [32].

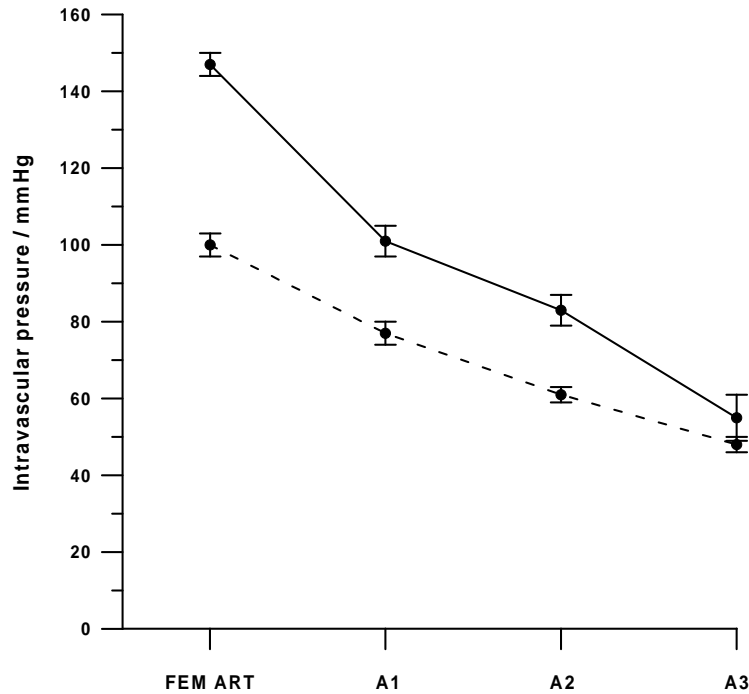


Figure 3.2: Intravascular pressure in a large (femoral) artery (FEM ART) of diameter ~ 1 mm, and in three categories of gut arterioles (A1-A3) in normal rats (dashed line) and rats with high blood pressure (solid line). Mean resting vessel diameters were: A1: $78 \mu\text{m}$; A2: $30 \mu\text{m}$; A3: $15 \mu\text{m}$. From [38].

highly reproducible [35]. If the infusion of the vasoconstricting agent is stopped, the normal, uniform cylindrical geometry is restored without remaining deformations, as generally would be expected if the phenomenon was a breakdown due to mechanical failure of the elastic tissue. Restoring the infusion causes again an extreme, uniform vasoconstriction followed by the reappearance of the sausage-string pattern. A third and intriguing feature of the phenomenon is its overall periodicity with constrictions and dilatations occurring in a regular and repetitive pattern.

In this chapter, we present a simple anisotropic, elastic model of the vessel wall. We show that under certain hypertensive conditions a novel Rayleigh-type instability occurs which leads to a periodic sausage-string pattern of constrictions and dilatations along the vessel. Our theory provides predictions for the conditions under which the cylindrical form of a blood vessel becomes unstable. Especially, we show that the appearance of the sausage-string pattern is limited to smaller blood vessels, because the pressure elevation there is relatively small (Fig. 3.2). Moreover, we show that the instability does not occur for vessels where the wall-to-lumen ratio (vessel-wall thickness divided by the inner radius) is large. In agreement herewith, the sausage-string pattern has not been observed in the small arterioles where the wall-to-lumen ratio is 0.3 - 0.5, compared to a value of 0.1 - 0.2 for larger blood vessels. Thus

we argue that the sausage-string pattern is caused by an instability, and not by a mechanical breakdown. Furthermore, the borders of the instability window, where the sausage-string pattern appears, are determined by two different conditions, one related to the pressure, the other related to the geometry.

3.2 Cylindrical blood vessels

In order to investigate the stability of a cylindrically shaped blood vessel, consider an initial small axial symmetric perturbation of the inner radius, $r \rightarrow r + u(z)$ (Fig. 3.3). If the perturbation grows in time, the cylindrical form is unstable, if it decreases toward zero, the cylindrical form is stable. To determine the stability, we must therefore know the dynamic equation for the perturbation $u(z, t)$. To this end, we invoke the continuity equation,

$$\partial_t(\pi r^2) = -\partial_z J, \quad (3.1)$$

associating a local change of the cross-sectional area at a downstream site z with a fluid flux $J(z)$. The flux is related to the transmural pressure P , by

$$J = -c(r)\partial_z P, \quad (3.2)$$

where $c(r)$ is the vascular conductance. In the Hagen-Poiseuille approximation, the fluid conductance is $c(r) = \pi r^4/(8\eta)$, where η is the dynamic viscosity of the fluid (blood). However, the specific form of $c(r)$ is not crucial for our purpose

From the continuity equation and the flux-pressure relation, the dynamic equation to lowest order in the perturbation follows,

$$\partial_t u = \frac{c(r)}{2\pi r} \partial_z^2 P. \quad (3.3)$$

Above, we have tacitly neglected the pressure drop along the vessel, noting that this is much smaller than the transmural pressure.

As a simple illustration, consider first a very thin vessel wall, for which the pressure is given by the Laplace form [39, 40]

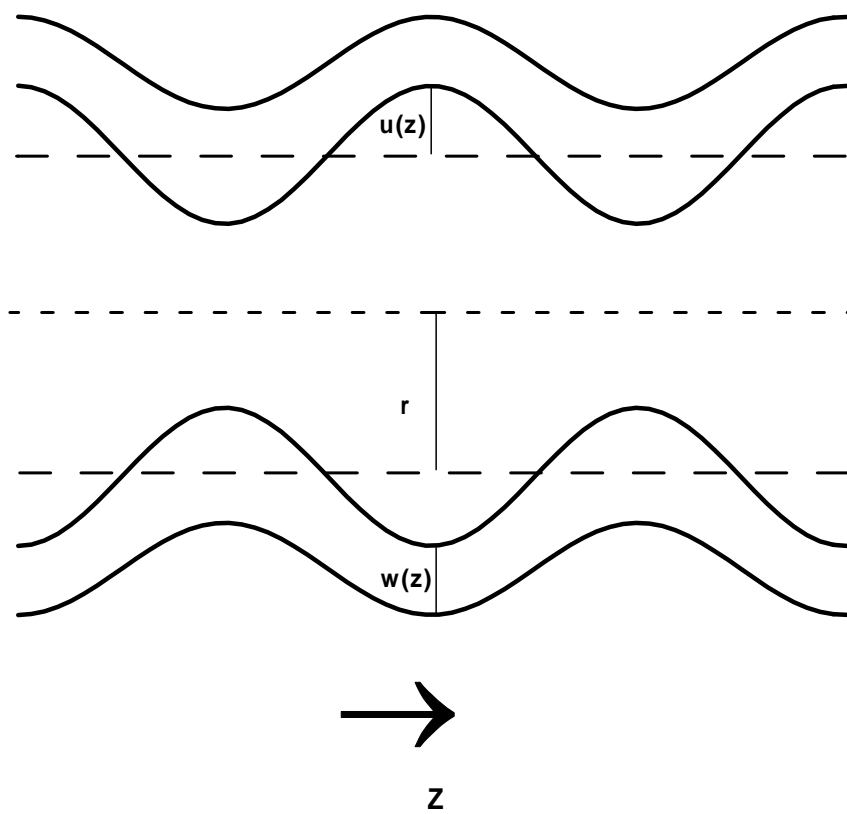
$$P = (T/R) + (T_z/R_z). \quad (3.4)$$

Here T and T_z are the tensions circumferential to and parallel with the cylinder axis z , and $1/R$ and $1/R_z$ are the principal curvatures in the corresponding directions,

$$\frac{1}{R} = \frac{1}{r[1 + (\partial_z r)^2]^{1/2}}, \quad \frac{1}{R_z} = \frac{-\partial_z^2 r}{[1 + (\partial_z r)^2]^{3/2}}. \quad (3.5)$$

Furthermore, we assume that the tensions are constant and identical, $T_z = T$. Using the above expression, Eq. (3.4), for the pressure, we get from Eq. (3.3), retaining only linear terms in u ,

$$\partial_t u = -\frac{Tc(r)}{2\pi r^3} [\partial_z^2 u + r^2 \partial_z^4 u]. \quad (3.6)$$



(b)

(c)

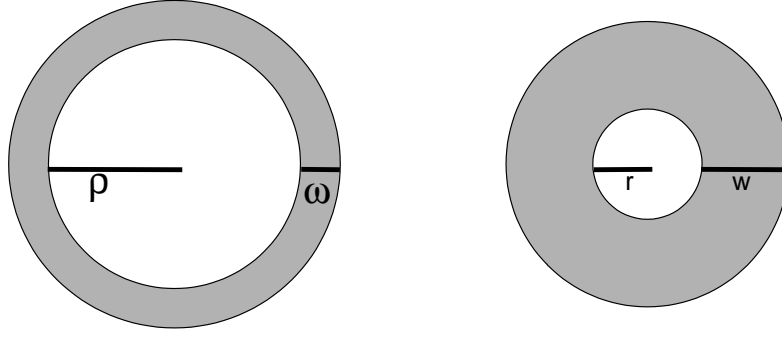


Figure 3.3: (a) A schematic picture of a blood vessel of inner radius r undergoing a perturbation $u(z)$. The wall thickness $w(z)$ is larger at smaller radii since the circumference is smaller. (b) Schematic cross-section of a blood vessel in relaxed state. (c) Schematic cross-section of a blood vessel in activated state. The cross-sectional area is assumed fixed, so the wall thickness is larger than in (b).

For a perturbation of the form

$$u = \sum_k u_k(t) \cos(kz) , \quad (3.7)$$

we have $u_k(t) \sim u_k(0)e^{\lambda_k t}$, where

$$\lambda_k = \frac{Tc(r)}{2\pi r^3} k^2 [1 - r^2 k^2] . \quad (3.8)$$

Thus, the vessel wall is unstable to modes with $rk < 1$. The dominant mode, where λ_k is maximal, is at $k = 1/(\sqrt{2}r)$.

The above instability is known as the Rayleigh instability [41, 42]. The theory explains why a cylindrical column of water with surface tension T is unstable at all radii. Alternatively, this can be shown in an energy context, varying the area

$$A = \int da = \int 2\pi r [1 + (\partial_z r)^2]^{1/2} dz \quad (3.9)$$

for fixed volume

$$V = \int \pi r^2 dz , \quad (3.10)$$

in order to minimize the surface energy

$$F = \int T da . \quad (3.11)$$

From a perturbation of the form $u = u_0 + u_k \cos(kz)$, where $u_0 = -u_k^2/(4r)$ [to lowest order in u_k] is determined by volume conservation, one obtains an energy change

$$\delta F = -F_0 [1 - r^2 k^2] (u_k/2r)^2 \quad (3.12)$$

[to lowest order in u_k], which is again favorable (negative) when $rk < 1$.

The cylindrical geometry may remain stable if stabilizing terms appear in the energy functional F . In the recent analysis of the so-called pearling instability [43, 44, 45], it is the reluctance against bending in tubular lipid membranes that stabilizes the cylindrical geometry. In the simplest form, an additional term [43]

$$\Delta F = \frac{1}{2}\kappa \int \left[\frac{1}{R} + \frac{1}{R_z} \right]^2 da , \quad (3.13)$$

κ being the bending modulus, is added to the surface energy. For Tr^2/κ sufficiently small, the cylindrical geometry remains stable (for all k). However, increasing the surface tension (using optical tweezers [43]), the instability occurs when Tr^2/κ crosses a given critical value.

In small blood vessels it is not the reluctance against bending but rather a strongly nonlinear stress-strain relation (Fig. 3.4) that is responsible for the stability of the cylindrical form. Under normal conditions, the stress is exponentially increasing with circumferential strain, and an increase in area by an amount δa is energetically much more expensive than gained by a similar decrease in area. Therefore, the cylindrical form remains stable. However, when the vessel contracts, the exponential behavior is replaced by a more slow variation, with a smaller area dependence in energy cost. At sufficiently strong contractions, energy is gained by reducing area, and the cylindrical form becomes unstable.

For blood vessels one cannot neglect the width w of the vessel wall. Taking the width of the vessel into account, the Laplacian form for the pressure is replaced by an integral,

$$P = \int_r^{r+w} \left[S \frac{1}{\tilde{r}[1 + (\partial_z \tilde{r})^2]^{1/2}} - S_z \frac{\partial_z^2 \tilde{r}}{[1 + (\partial_z \tilde{r})^2]^{3/2}} \right] d\tilde{r} , \quad (3.14)$$

where S and S_z are the stresses, circumferential and parallel with the vessel. The stresses, S and S_z , defined as the forces per actual cross-sectional area, are related to the experimentally measured idealized stresses, σ and σ_z , defined as the forces per relaxed cross-sectional area [48],

$$S = \gamma\gamma_z\sigma , \quad S_z = \gamma\gamma_z\sigma_z . \quad (3.15)$$

Here γ and γ_z are the normalized lengths in the circumferential direction and in the vessel direction, i.e. γ (γ_z) is equal to L/L_0 where L is the actual length of a tissue strip in the circumferential direction (vessel direction) and L_0 is the corresponding resting length. The strain, ϵ (ϵ_z), is by definition equal to $\gamma - 1$ ($\gamma_z - 1$). Since the length of a vessel remains almost constant during a contraction, γ_z is here assumed to be constant, $\gamma_z = \gamma_0$. Correspondingly, the stress σ_z is replaced by a constant σ_0 .

The width w of the vessel wall changes when the inner radius r changes (Fig. 3.3). Assuming that the cross-sectional area of the vessel wall is constant, the radius dependence of w is given, when the inner radius ρ and wall thickness ω are known for the angularly relaxed state ($\gamma = 1$). We have

$$(r + w)^2 - r^2 = (\rho + \omega)^2 - \rho^2 . \quad (3.16)$$

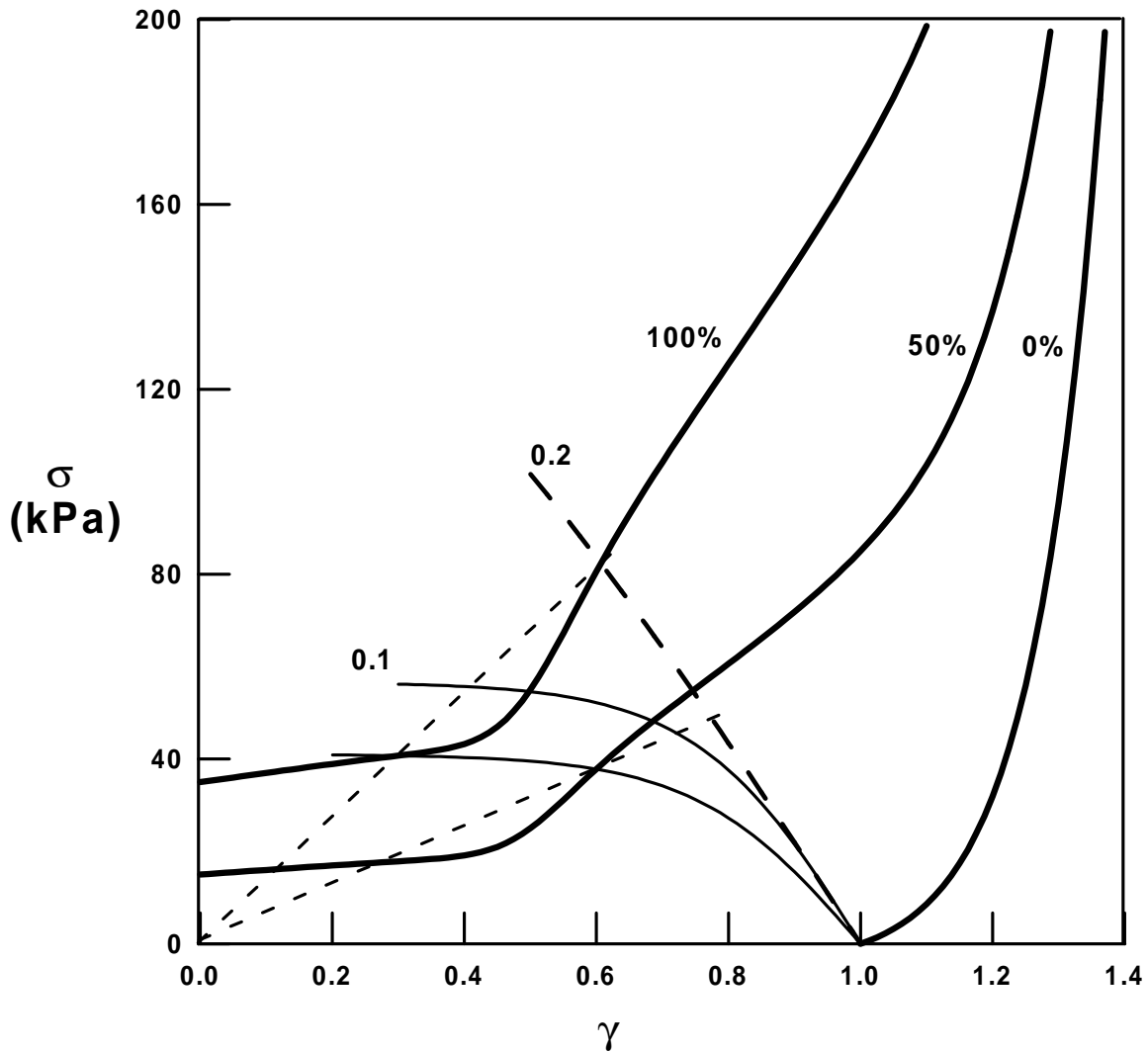


Figure 3.4: A schematic plot of typical stress-strain relations for arterioles (adapted from [46, 47]). The three heavy solid curves correspond to a completely relaxed vessel (0%), a vessel where the smooth muscle cells are half maximally activated (50%), and a vessel where the smooth muscle cells are maximally activated (100%). The thin solid lines indicate how the points $(\gamma_r, \sigma(\gamma_r))$ and $(\gamma_w, \sigma(\gamma_w))$ [marked 0.1] move with muscle cell activation for an arteriole with wall-to-lumen ratio $\omega/\rho = 0.1$. The point of instability ($r = r_c$) for the cylindrical form of the blood vessel can be illustrated geometrically by thin dashed lines from $(0, 0)$ through $(\gamma_r, \sigma(\gamma_r))$ [see text]. The instability point is where $\sigma(\gamma_w)/\gamma_w$ equals $\sigma(\gamma_r)/\gamma_r$. The thick dashed line [marked 0.2] shows how the point $(\gamma_w, \sigma(\gamma_w))$ move with muscle cell activation for an arteriole with $\omega/\rho = 0.2$, keeping the same curve for $(\gamma_r, \sigma(\gamma_r))$.

Equation (3.16) suggests a useful change of variable, from \tilde{r} to $\tilde{\rho}$, where

$$\tilde{r}^2 - r^2 = \tilde{\rho}^2 - \rho^2 . \quad (3.17)$$

When \tilde{r} varies between values r and $r + w$, which under perturbations changes along the z axis, $\tilde{\rho}$ varies between the fixed values ρ and $\rho + \omega$. The normalized length γ at a radius \tilde{r} is simply the ratio between \tilde{r} and its relaxed value $\tilde{\rho}$: $\gamma = \tilde{r}/\tilde{\rho}$ (Fig. 3.3).

For small perturbations, the relevant expression for the pressure reduces to

$$P = \gamma_0 \int_{\rho}^{\rho+\omega} [\sigma - \sigma_0 r \partial_z^2 r] [\tilde{\rho}^2 - \rho^2 + r^2]^{-1/2} d\tilde{\rho} , \quad (3.18)$$

where the stress σ in the circumferential direction depends on the normalized length

$$\gamma = [\tilde{\rho}^2 - \rho^2 + r^2]^{1/2} / \tilde{\rho} . \quad (3.19)$$

To linear order in the perturbation $u(z, t)$, we obtain

$$P = P_0(r) + I(r)u - I_0(r)\partial_z^2 u , \quad (3.20)$$

where

$$P_0(r) = \gamma_0 \int_{\rho}^{\rho+\omega} \sigma [\tilde{\rho}^2 - \rho^2 + r^2]^{-1/2} d\tilde{\rho} , \quad (3.21)$$

$$\begin{aligned} I_0(r) &= \gamma_0 \sigma_0 r \int_{\rho}^{\rho+\omega} [\tilde{\rho}^2 - \rho^2 + r^2]^{-1/2} d\tilde{\rho} \\ &= \gamma_0 \sigma_0 r \log[1 + (\omega + w)/(\rho + r)] , \end{aligned} \quad (3.22)$$

and

$$I(r) = \frac{d}{dr} P_0(r) = \gamma_0 \int_{\rho}^{\rho+\omega} \tilde{\rho}^{-1} \frac{d}{d\gamma} \left[\frac{\sigma}{\gamma} \right] \frac{\partial \gamma}{\partial r} d\tilde{\rho} . \quad (3.23)$$

The partial derivatives of γ with respect to r and $\tilde{\rho}$ are related,

$$\tilde{\rho}^{-1} (\partial \gamma / \partial r) = r (\rho^2 - r^2)^{-1} (\partial \gamma / \partial \tilde{\rho}) , \quad (3.24)$$

and $I(r)$ can be expressed in terms of the normalized length γ ,

$$I(r) = \frac{\gamma_0 \gamma_r}{\rho(1 - \gamma_r^2)} \left[\frac{\sigma(\gamma_w)}{\gamma_w} - \frac{\sigma(\gamma_r)}{\gamma_r} \right] , \quad (3.25)$$

where

$$\gamma_r = r/\rho , \quad \gamma_w = (r + w)/(\rho + \omega) , \quad (3.26)$$

are the normalized inner and outer radius. Note that $I(r)$ is not singular at $\gamma_r = 1$, where also $\gamma_w = 1$.

By Eq. (3.20), the dynamic equation, Eq. (3.3), for the perturbation $u(z, t)$ takes the form

$$\partial_t u = -\frac{c(r)}{2\pi r} [-I(r)\partial_z^2 u + I_0(r)\partial_z^4 u] . \quad (3.27)$$

For a perturbation of the form (3.7), we have $u_k(t) \sim u_k(0)e^{\lambda_k t}$ with

$$\lambda_k = \frac{c(r)}{2\pi r} k^2 [-I(r) - I_0(r)k^2] . \quad (3.28)$$

The value of $I_0(r)$ is always positive. Therefore, it is the sign of $I(r)$ that determines the stability of the vessel wall. If $I(r)$ is positive the cylindrical geometry is stable for all modes. If $I(r)$ is negative, the cylindrical geometry is unstable, more specifically to modes with $k^2 < |I|/I_0$.

The dominant (fastest growing) mode, where λ_k is maximal, is at the value $k = [|I|/(2I_0)]^{1/2}$, corresponding to ‘sausages’ of length

$$\ell = 2\pi[2I_0/|I|]^{1/2} . \quad (3.29)$$

For $\omega/\rho = 0.1$, and $\sigma_0 = 100$ kPa, we find $|I|\rho \approx 2I_0/\rho \approx 10$ kPa. Hence, $\ell \approx 2\pi\rho$, and the length of the ‘sausages’ will be 5-10 times the radius of the relaxed vessel. This is in good agreement with experimental observations [35] (Fig. 3.1).

From the expression for $I(r)$, Eq. (3.25), it is seen that the important quantity is σ/γ . The cylindrical form becomes unstable when σ/γ calculated at the inner radius ($r = r_c$) equals the value of σ/γ at the outer radius. This is illustrated geometrically (Fig. 3.4), by drawing a line (thin dashed) in the plot of σ versus γ from $(0, 0)$ through $(\gamma_r, \sigma(\gamma_r))$. The slope of this line is obviously $\sigma(\gamma_r)/\gamma_r$. If the point $(\gamma_w, \sigma(\gamma_w))$ lies above this line, $\sigma(\gamma_w)/\gamma_w > \sigma(\gamma_r)/\gamma_r$, $I(r)$ is positive, and the cylindrical form is stable. If on the other hand the point $(\gamma_w, \sigma(\gamma_w))$ lies below the line, $\sigma(\gamma_w)/\gamma_w < \sigma(\gamma_r)/\gamma_r$, $I(r)$ is negative, and the cylindrical form is unstable.

Under normal physiological conditions, the circumferential stress σ in blood vessels increases exponentially with the normalized length [39, 40, 46, 47] (Fig. 3.4), and the value of $I(r)$ is therefore positive (Fig. 3.5). This ensures that the blood vessel keeps its cylindrical form. However, when acute hypertension is induced by infusion of a strong vasoconstricting agent like angiotensin II, there will be a significant reduction of the inner radius in small arteries and large arterioles due to contraction of the smooth muscle cells. The operating point for the vessel will move to the less steep part of the $\sigma - \gamma$ curve (Fig. 3.4), and when the inner radius is reduced below a certain value r_c at which $\sigma(\gamma_w)/\gamma_w = \sigma(\gamma_r)/\gamma_r$, the value of $I(r)$ becomes negative (Fig. 3.5). The cylindrical form becomes unstable, and the ‘sausage-string’ pattern appears.

The ‘sausage-string’ pattern following infusion of angiotensin II has been found to occur predominantly in small arteries and large arterioles [35]. In accordance herewith, the present analysis predicts that large vessels will be stable. In this case, the operating point $(\gamma, \sigma(\gamma))$ lies on the steep part of the $\sigma - \gamma$ curve, at high pressure elevation and rather small contraction (Fig. 3.2 and Fig. 3.4), thus the larger vessels do not reduce their radii below the critical value r_c . As arterial vessels get smaller, the wall-to-lumen ratio ω/ρ generally increases [39, 40]. From the expression for $I(r)$, Eq. (3.25), we find that the value of r_c decreases with increasing wall-to-lumen ratio ω/ρ (Fig. 3.6). In Fig. 3.4, the thin solid lines illustrate how the points $(\gamma_r, \sigma(\gamma_r))$ and $(\gamma_w, \sigma(\gamma_w))$ [marked 0.1] move with muscle cell activation for an arteriole with wall-to-lumen ratio $\omega/\rho = 0.1$. For a given activation of the smooth muscle cells (50%, 100%),

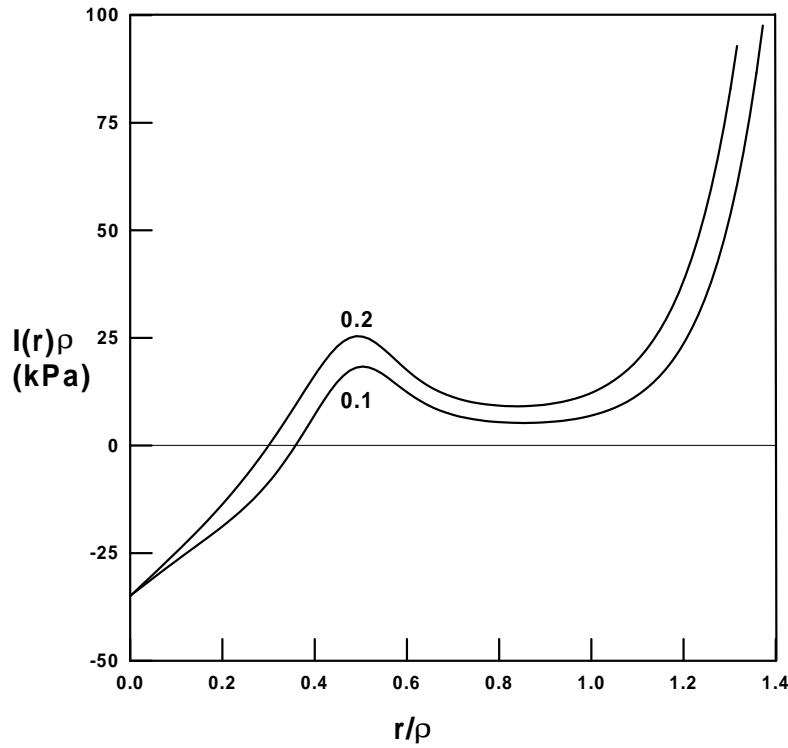


Figure 3.5: A plot of the stability measure $I(r)$ at large muscle cell activation for two different wall-to-lumen ratios, $\omega/\rho = 0.1$ and $\omega/\rho = 0.2$. The cylindrical form of a blood vessel becomes unstable when I becomes negative (at $r = r_c$). An almost linear stress-strain relation in a region above r_c gives rise to a decay of I . Above $\gamma = 1$, where the stress increases exponentially, also $I(r)$ increases exponentially.

a thin dashed line is drawn from $(0, 0)$ through $(\gamma_r, \sigma(\gamma_r))$. As argued above, when the point $(\gamma_w, \sigma(\gamma_w))$ lies above the thin dashed line, the cylindrical form is stable; when it lies below, the cylindrical form is unstable. For $\omega/\rho = 0.1$, we see from Fig. 3.4 that the cylindrical form is stable at 50% activation, but unstable at 100% activation of the smooth muscle cells surrounding the blood vessel. For $\omega/\rho = 0.2$ ($(\gamma_w, \sigma(\gamma_w))$ illustrated by thick dashed line marked 0.2), the cylindrical form is only barely unstable at 100% activation. For larger wall-to-lumen ratios, the cylindrical form remains stable (Fig. 3.6). Hence, the ‘sausage-string’ instability will not appear in blood vessels with large wall-to-lumen ratios. While the transmural pressure and the contractile potential sets an upper limit, the wall-to-lumen ratio sets a lower limit for vessels that will undergo the ‘sausage-string’ instability in response to an acute increase in blood pressure.

We note that when $I(r)$ becomes negative, the pressure at slightly larger radii is smaller than at slightly smaller radii. Accordingly, the resulting flow J will be directed from low-radii regions to high-radii regions, causing the small radii to become even smaller, and the large radii to become larger. This continues until the pressure stabilizes at a value which is the same for both the large radius r_{max} and the small

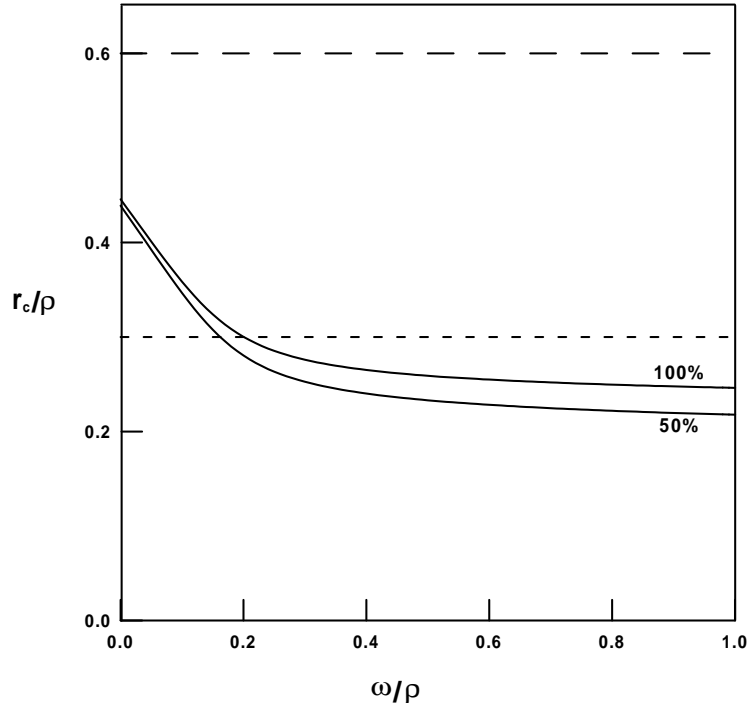


Figure 3.6: The critical radius r_c , normalized by relaxed radius ρ , decreases with (relaxed) wall-to-lumen ratio ω/ρ . Above the r_c curve, the cylindrical form is stable, below it is unstable. The dashed lines indicate the circumferential normalized lengths $\gamma_r = 0.6$ at 50% and $\gamma_r = 0.3$ at 100% activation of the smooth muscle cells. At 50% activation, the γ_r line lies entirely in the stable regime, and the cylindrical form is stable for all wall-to-lumen ratios. At 100% activation, the γ_r line lies in the unstable regime for wall-to-lumen ratios below 0.2, hence the cylindrical form is unstable for blood vessels with $\omega/\rho < 0.2$.

radius r_{min} . The stabilization is possible because the pressure for radii above the instability, $r > r_c$, again increases with r . The theory allows an estimate of the radius in the dilated regions, r_{max} . Assuming that r_{min}/ρ is small (close to zero), the final value of r_{max} is estimated by the condition $P(r_{max}) = P(0)$. Interestingly, the almost linear stress function in the region above r_c (Fig. 3.4) gives rise to a decay of $I(r)$ in the same region (Fig. 3.5). As a consequence r_{max}/r_{min} can become quite large. However, close to $\gamma = 1$, the stress increases exponentially due to the elastic properties of the vessel wall [39, 40], and the value of $I(r)$ will also increase rapidly. This will prevent r_{max} from attaining a value substantially larger than the relaxed radius, ρ , of the vessel. Preliminary experimental data from Gustafsson's laboratory confirm this. However, r_{max} may be larger than the working radius of the vessel under normal physiological conditions, because the normal working radius is smaller than the relaxed radius [39, 40], i.e. the vessel has spontaneous tone. This may explain why earlier the dilated regions have been suggested as a 'blow out' due to mechanical

failure of the vessel wall [37].

3.3 Conclusions

In summary, we have demonstrated that during severe vasoconstriction, the normal cylindrical geometry of a blood vessel may become unstable, resulting in a sausage-string pattern of alternating constrictions and dilatations. The sausage-string pattern is thus the expression of an instability, and not caused by a mechanical failure of the vessel wall due to a high blood pressure. The instability is associated with the Rayleigh instability of a fluid column and with the ‘pearling’ instability observed in tubular lipid membranes. The mechanism behind the instability is however novel, involving the nonlinear stress-strain characteristics of the vessel wall. The developed theory explains many of the key features observed experimentally, especially why the instability is only observed in small arteries and large arterioles, and predominantly in those with small wall-to-lumen ratios.

PhysicsWeb

Institute of Physics Publishing

News: 16 October 1998

Physics solves blood vessel mystery

[Friday October 16] A group of physicists has solved a surgical mystery that has puzzled doctors for over 70 years. When a patient suffers high blood pressure, small blood vessels tend to alternately constrict and dilate along their length, forming a "sausage-string" pattern that is damaging to the patient. Previously physicians had thought that the blood vessels had suffered a "blow-out", but closer examination by Finn Gustafsson and colleagues in Denmark and Spain reveals that the blood pressure is too small to cause such an effect. Instead they suggest that the elasticity characteristics of the vein cause the problem. The work has been submitted to *Physical Review Letters*.

Experiments on the effect have been performed by introducing a compound called angiotensin II into the blood stream of a rat. This compound narrows the diameter of the blood vessels, which increases the blood pressure and leads to the formation of the "sausage-string" pattern in the blood vessels. If the angiotensin II is removed, the blood vessel returns to its previous shape. Gustafsson's group suggests that the shape of the blood vessel becomes unstable at high blood pressure if the inner radius of the vessel becomes perturbed.

Gustafsson and co-workers defined a quantity, $I(r)$, in terms of the dimensions and elastic properties of the vessels. If $I(r)$ is positive, then the stress on the vessel increases in such a way to keep the blood vessel cylindrical in shape. However, if $I(r)$ is negative, the radius of the vessel at that point becomes smaller, increasing the pressure and causing blood to flow away from this region. This further reduces the radius, eventually leading to the "sausage-string" pattern in the vein. According to their equations, the length of each "sausage" should be 5-10 times the radius of the vessel, which is backed up by experimental evidence. The theory also explains why similar patterns are not seen in larger blood vessels.

RELATED LINKS:

[Instability and 'Sausage-String' Appearance in Blood Vessels during High Blood Pressure](#)



From the SCIENCE newsroom

More
News

Posted **10 March 1999**, 5 pm PST

APNet
Home

The Secret of Blood Sausages

Blood vessels under high pressure undergo weird contortions: They swell and shrink into something resembling sausages on a string. Now a team of physicists has developed equations that model this curious--and potentially harmful--behavior and can predict when and where it might occur. The scientists say their calculations, reported in the 1 March *Physical Review Letters*, could lead to new ways of treating acute hypertension.

The sausage-string pattern, first noticed in the 1950s in laboratory animals, has been found in people who suffer from extremely high blood pressure. Physiologists thought that weak spots in the vessel walls ballooned under high pressure, but this did not explain the regularity of the changes or their presence in smaller vessels where pressure is not as high. To solve the mystery, Preben Alstrøm, a physicist at the Niels Bohr Institute in Copenhagen, Denmark, and his colleagues examined the inherent stability of blood vessels.

The researchers started with equations that describe blood flowing through cylindrical tubes with the elasticity of blood vessels, then they worked out a theory to describe what happens when muscle cells constrict the vessels. This squeezing, their model predicts, would not only narrow the vessel but, paradoxically, also lead it to swell in some places--exactly the sausage-string pattern. "A normal blood vessel is stable because to expand costs it a lot of energy," says Alstrøm. But when constricted, the system is perturbed and slight variations in variables such as rate of fluid flow will make sections of the vessel more inherently "stable" if they expand.

The team may have finally hit upon the correct explanation for the sausage-string pattern in arteries*, says Raymond Goldstein, a physicist at the University of Arizona, Tucson. He'd still like to see more detailed experimental work that can be compared to the model's predictions, such as how the length of each sausage depends on parameters like the thickness of the artery walls. Alstrøm says this sort of knowledge could lead to ways to prevent the formation of the sausage-link shapes, which can disrupt blood flow. For example, he imagines drugs that might change the elasticity of the arteries so that they don't become unstable under high pressure.

--Meher Antia

IDEAL
Online
Journals

Book
Catalog

Journal
Sites

Chapter 4

Frozen spatial chaos induced by boundaries

We show that rather simple but non-trivial boundary conditions could induce the appearance of spatial chaos (that is stationary, stable, but spatially disordered configurations) in extended dynamical systems with very simple dynamics. We exemplify the phenomenon with a nonlinear reaction-diffusion equation in a two-dimensional undulated domain. Concepts from the theory of dynamical systems, and a transverse-single-mode approximation are used to describe the spatially chaotic structures¹.

¹This Chapter corresponds to *Frozen spatial chaos induced by boundaries*, by V.M. Eguíluz, E. Hernández-García, O. Piro, S. Balle, to appear in Phys. Rev. E (1999).

4.1 Introduction

In the past few decades, considerable understanding of the phenomenon of temporal chaos in dynamical systems of few degrees of freedom has been achieved [49, 50, 51]. On the other hand, spatio-temporal chaos in extended dynamical systems with infinitely many degrees of freedom is currently under very active investigation [52, 53]. It is remarkable however, that an area of problems laying somehow between the two extremes has not received so much attention, namely, purely spatial chaos as a stationary attractor of extended dynamical systems [54, 55, 56, 57, 58, 59, 60, 61, 62].

The possible existence of this kind of attractors was first suggested by Ruelle [63] in the context of equilibrium phases. He pointed out the parallelism between a time-dependent differentiable dynamical system and the space dependence of equilibrium states in statistical mechanics. He then raised the question as to whether the existence of turbulent crystals could be the natural next step towards complexity after spatially homogeneous, periodic, and quasi-periodic equilibrium phases have been found. Newell and Pomeau [64] gave some conditions under which such a turbulent crystal would exist in pattern-forming systems described by a free energy. Theoretical and experimental work on modulated phases and commensurate-incommensurate transitions [65, 66, 67, 68] represent additional concrete results along these lines.

In the context of fluid dynamics, the existence of spatially chaotic, but temporally steady solutions would also fill a conceptual gap between two well-studied complex phenomena: Lagrangian chaos, and Eulerian chaos or turbulence. The former refers to the chaotic motion of a fluid parcel which might occur even in laminar and, in three dimensions, steady flows [69, 70, 71]. On the other extreme, the road to turbulence is usually associated to a hierarchy of instabilities leading to increasingly spatio-temporally chaotic Eulerian velocity fields. Frozen spatial chaos would then refer in this context to a third possibility: a stationary flow spatially chaotic in the Euler description.

By now, many extended dynamical systems displaying spatial chaos have been identified. Most of the studies are concerned with one-dimensionally extended systems. They are specially suitable to analysis because their steady state configurations depend just on the unique spatial coordinate. These configurations are solutions of sets of ordinary differential equations (the *spatial* dynamical system) with the space variable as the independent variable. The standard theory of low-dimensional dynamical systems can be used to describe such configurations, by just considering the spatial coordinate as a fictitious time. Rigidly traveling waves with spatial chaotic structure can also be considered as a case of spatial chaos in a moving reference frame [56, 57, 58, 59, 60, 61].

Spatial chaos may appear when the *spatial* dynamical system has a sufficiently high dimensional phase space. This high dimensionality may arise from either a) the presence of high-order spatial derivatives in a single evolution equation as in the cases of the Swift-Hohenberg equation [72, 73], and Kuramoto-Sivashinsky and related models [58, 62], b) the coupling of several fields each one satisfying a lower order differential equation as in excitable media [59, 60, 61] and in (the real and imaginary parts of) the complex Ginzburg-Landau equation [56, 57] which supports

chaotic travelling waves, or c) explicit space dependent forcing terms as in [54] or [74]

Consideration of two-dimensional spatial chaos has been much scarce. In absence of a simple connection with conventional dynamical systems theory, the very concept of chaos in the spatial configuration should be properly defined for the general two-dimensional case. A rather complete formalism generalizing dynamical system tools (entropies, dimensions,...) to multidimensional spatial chaos has been developed [55, 75], and some examples examined [55, 73]. On the other hand, as the number of dimensions increases, a much larger variety of non-trivial boundary condition classes surely leads to a greater richness in the expected properties of the steady field configurations. A well-posed question is then whether relatively simple boundary conditions may lead to steady spatially chaotic configurations. The main purpose of this chapter is to address this question.

In addition to the existence of chaotic spatial configurations, it is important to study also their stability in time. A stationary state will only be physically observable if it is stable or at least long-lived. It turns out that the temporal stability of the stationary solutions is in general unrelated to the stability of these configurations considered as orbits of the spatial dynamical system. In the examples cited above, there are cases of both stable and unstable space-chaotic configurations, but instability seems to be more frequent. As a consequence, spatial chaos has been generally considered of limited physical relevance.

In this chapter we show that rather simple undulated strip-like domain shapes can induce, in a very simple nonlinear extended dynamical system, the formation of patterns that are both *spatially chaotic* and *temporally attracting*. The kind of *modulated boundaries* we use could be easily implemented in standard experimental pattern-formation set-up's such as Faraday waves, convection cells, or open flows. In fact, our work was originally motivated by the observation, in a fluid dynamics experimental setup consisting of a periodic array of pipe bends, that the transverse profile of the steady flow does not necessarily repeat itself with the same periodicity of the array [70].

In Section 4.2 we present the particular model that we study and perform a preliminary analysis of its behavior. In Section 4.3 a single-transverse-mode approximation is introduced and we use it to predict the existence of boundary-induced spatial chaos. Numerical simulations are presented in Section 4.4 to substantiate our claims beyond the validity of the previous approximation. Finally we summarize the results and open problems in the Conclusions.

4.2 A reaction-diffusion equation in a strip-shaped domain

As stated before, the application of the theory of dynamical systems to the study of stationary spatial configurations of one-dimensionally extended systems is direct. A stationary pattern satisfies, in general, a system of ordinary differential equations

with the spatial coordinate as its independent variable which we can think of as a time. Parity symmetry in a spatial coordinate will appear as time-reversal symmetry after reinterpretation of this coordinate as time.

The general study of spatial chaos in several spatial dimensions requires the notion of translational dynamical systems with d times [55, 75]. There are situations, however, where such formalism is not necessary because the two independent spatial directions are distinguished by the geometry of the system, so that one of them naturally plays the role of time. In this way, the spatial variation in one direction would be interpreted as time evolution of a one-dimensional field that only depends on the remaining spatial coordinate. Particularly suited to our approach will be the case of two-dimensional extended systems in strip-shaped regions much longer (ideally infinite) in the time-like direction than in the space-like one. If the strip is narrow enough, only patterns composed of one or few transverse spatial modes will be allowed and spatial chaos could be readily defined and identified in terms of the usual concepts of dynamical systems theory.

In order to concentrate on spatial chaos purely induced by boundary effects, we consider a very simple model equation containing only up to second order derivatives and a single field variable, a reaction-diffusion equation of the Fisher-Kolmogorov type:

$$\partial_t \psi = \nabla^2 \psi + a\psi - \psi^3 \quad , \quad (4.1)$$

with appropriate boundary conditions for the real field $\psi(\mathbf{x}, t)$. The real linear coefficient a can be absorbed rescaling the variables, but we find convenient to keep it explicit in the equation. Equation (4.1) appears in several contexts including phase transitions, where it takes the name of real Ginzburg-Landau equation or time-dependent Ginzburg-Landau model [76], and population dynamics [77]. The dynamics of (4.1) can be written as purely relaxational [78, 79] in a functional Lyapunov potential $V[\psi]$:

$$\partial_t \psi = -\frac{\delta V[\psi]}{\delta \psi} \quad (4.2)$$

with

$$V[\psi] = \int_D d\mathbf{x} \left(\frac{1}{2} |\nabla \psi|^2 - \frac{a}{2} \psi^2 + \frac{1}{4} \psi^4 \right) + S[\psi] \quad , \quad (4.3)$$

where the integral is over the domain D . The surface term $S[\psi]$ takes into account the effects of boundary conditions over the domain limit, and it vanishes when periodic, null Dirichlet ($\psi = 0$) or null Neumann ($\partial_n \psi = 0$) boundary conditions are specified. It follows from Eq. (4.2) that V can only decrease with time. The relaxational character of Eq. (4.2) implies also that the only asymptotic states are fixed points. Therefore, this model does not display any limit-cycle oscillations or more complex dynamics such as temporal chaos in any number of spatial dimensions.

Equation (4.1) has been extensively studied in one and two dimensions. In one dimension, for infinite systems, we have the following situations: For $a < 0$, $\psi = 0$ is the only stationary solution and is stable under time evolution. At $a = 0$ a pitchfork bifurcation occurs and the former trivial solution loses its stability. For $a > 0$ some of the stationary solutions are the following:

1. Homogeneous solutions: $\psi(x, t) = 0$, and $\psi(x, t) = \pm\sqrt{a} \equiv \psi_{\pm}$.
2. Kink type solutions: $\psi(x, t) = \pm\sqrt{a} \tanh(\sqrt{\frac{a}{2}}x)$.
3. Periodic solutions: $\psi(x, t) = \sqrt{a - k^2} \sin(kx) + \dots$, where the ellipsis stands for higher order harmonics.

Only ψ_{\pm} and the kinks are now linearly stable.

For finite systems, the boundary conditions normally restrict the variety of solutions either by selecting some values of k , or by favoring either the kink or the ψ_{\pm} solutions. Additionally, the boundary conditions may have as an effect a shift in the pitchfork bifurcation point $a = 0$ to a different value $a_c \neq 0$ and a change in the coefficients appearing in the solutions.

The typical time evolution of initial field distributions leads to the formation of domains where values of ψ close to either ψ_+ or ψ_- dominate. These domains are separated by kink- or anti-kink-type walls that can move into each other producing a mutual annihilation. By this mechanism, small domains disappear and feed the larger domains whose sizes then increase logarithmically in time until one of the stationary solutions, prevailing by chance, takes over the whole system.

In two dimensions, the dynamics typically consists of the coarsening of domains of ψ_+ and ψ_- phases whose typical size grows as the square root of time[76]. Interfaces between the two phases are locally similar to the one-dimensional kink solutions. The gradient term in Eq. (4.3) is important at the interfaces giving a positive contribution to the Lyapunov potential. Since the dynamics always minimizes V , it tends to reduce the length of these interfaces. This reduction is achieved by the shrinking and ulterior collapse of the smallest domains to contribute to the (square-root) growth of the remaining ones.

It was shown by Collet [80] in a more general context that the time evolution and final states of Eq. (4.1) in finite domains are similar to those in an infinite system except in a boundary layer around the border whose size depends on the a parameter. This result holds in both one and two dimensions. Thus, in order to observe the influence of boundaries on pattern evolution, we need to consider a domain small enough at least in one of the directions. In a striped domain, elongated in the x direction, this small dimension will be the transverse y direction. The domain will be limited in this transverse dimension by the boundaries $y_0(x)$ and $y_1(x)$, where the function $\psi(x, y, t)$ will take values $\psi_0(x)$ and $\psi_1(x)$, respectively (Dirichlet conditions).

In the one-dimensional case, conventional dynamical systems theory implies that there are no chaotic stationary solutions to Eq. (4.1) because the spatial dynamical system is just a second order ordinary differential equation. However, chaos can arise if some x -dependent periodic forcing is added to the equation. These arguments do not apply directly to the two-dimensional case. However, it is tempting to think of undulations of the lateral boundaries as a kind of periodic forcing on the longitudinal coordinate. This suggests the possibility of finding chaotic structures in the x -direction induced by undulated boundaries.

As a particular case we consider domains limited by two sinusoidal boundaries.

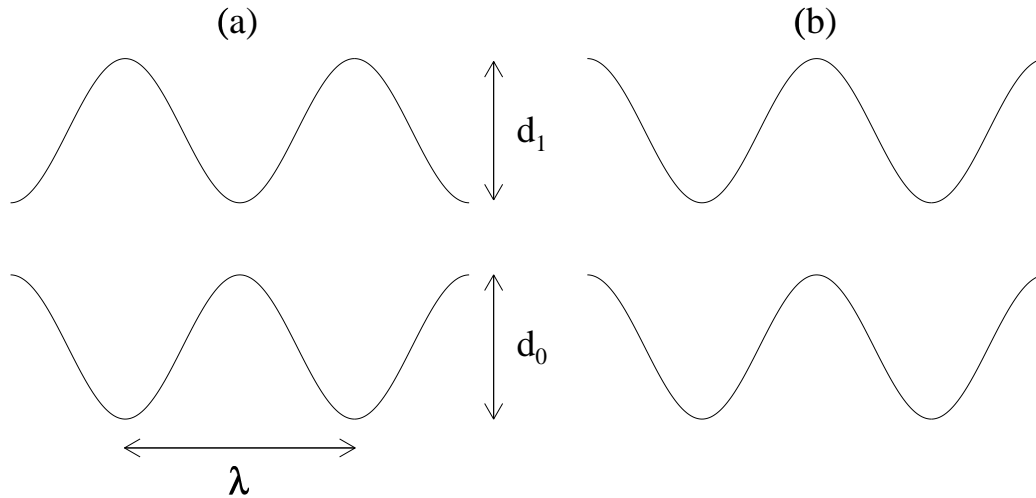


Figure 4.1: Examples of stripped channels enclosed in oscillating walls: $\alpha = 2\pi/\lambda$; $d_0 = d_1$, and (a) $\phi = \pi$, (b) $\phi = 0$.

With applications to hydrodynamics in mind we think of these domains as channels with sinusoidal banks.

$$y_1(x) = \frac{d_1}{2}(1 - \cos(\alpha x)) \quad (4.4)$$

$$y_0(x) = -1 - \frac{d_0}{2}(1 + \cos(\alpha x + \phi)) \quad (4.5)$$

Here d_1 , d_0 are the amplitude of the undulation of each bank, α is the spatial frequency which we assume to be the same for both banks and ϕ is their mutual phase mismatch. Figure (4.1) shows a few typical shapes for our channel-like domains. The case $d_1 = d_0$ and $\phi = \pi$ gives a sausage shaped channel with symmetrically and sinusoidally varying width. On the other hand, $d_1 = d_0$ and $\phi = 0$ sets the boundaries in phase and corresponds to a domain with the form of a sinusoidally meandering channel of constant y -width.

We stress that we want to consider the simplest situation that may display spatial chaos. Consideration of more complex equations exhibiting spatial chaos even with simple boundaries, or more complex boundaries such as incommensurate oscillations for the upper and lower banks (corresponding to quasi-periodic forcing) would only enrich the complexity of stationary solutions.

A complete definition of the model requires also the specification of boundary conditions on the longitudinal x direction. The analogy with a temporal variable would be better for domains infinite in the x direction, with only the weak requirement of boundedness for ψ . However, an infinite domain is inadequate for the numerical approaches to be described below. In our calculations we would need to impose

periodic boundary conditions (of period L) along the x direction. In this way we are restricting the class of solutions to periodic orbits of period L or less in the time-like coordinate. We will still be able to identify as spatially chaotic the configurations that have the maximal period L , provided this period increases and the periodic orbit approaches a chaotic trajectory as system size L increases. Subtle considerations such as Lyapunov number computations for such limiting orbits will be addressed elsewhere.

To perform numerical simulations we can choose between several strategies. If we are only interested in stationary states, we can numerically solve the time-independent version of Eq. (4.1) by means of finite elements or finite differences. These methods can be implemented to find solutions that may or may not be stable under time evolution. Another possibility is to follow the dynamics of the full Eq. (4.1) until a stationary state is reached. In this way, only attracting (i.e. stable) stationary solutions can be found (remind that only stationary attractors are allowed by this purely relaxational dynamics). In any case, a convenient way to handle the boundary conditions is to map the region limited by $y_0(x)$ and $y_1(x)$ (and by $x = 0, L$) to a rectangular one: $\tilde{y}_1 = 1$, $\tilde{y}_0 = 0$, and $x = 0, L$. For arbitrary functions $y_0(x)$ and $y_1(x)$, the map $(x, y) \mapsto (x, \tilde{y})$, with

$$\tilde{y} = (y - y_0)/(y_1 - y_0) , \quad (4.6)$$

transforms Eq. (4.1) into an equation for $\tilde{\psi}(x, \tilde{y}, t) \equiv \psi(x, y, t)$:

$$\begin{aligned} \partial_t \tilde{\psi} = & \partial_{xx}^2 \tilde{\psi} + \mathcal{F}(x) \partial_{\tilde{y}\tilde{y}}^2 \tilde{\psi} + \mathcal{G}(x) \partial_{x\tilde{y}}^2 \tilde{\psi} \\ & + \mathcal{H}(x) \partial_{\tilde{y}} \tilde{\psi} + a\tilde{\psi} - \tilde{\psi}^3 \end{aligned} \quad (4.7)$$

where

$$\mathcal{F}(x) = \frac{1 + (\Delta_x \tilde{y} + y_{0x})^2}{\Delta^2} \quad (4.8)$$

$$\mathcal{G}(x) = -2 \frac{\Delta_x \tilde{y} + y_{0x}}{\Delta} \quad (4.9)$$

$$\mathcal{H}(x) = \frac{\tilde{y}(2\Delta_x^2 - \Delta \Delta_{xx}) - \Delta y_{0xx} + 2\Delta_x y_{0x}}{\Delta^2} \quad (4.10)$$

$$\Delta(x) = y_1(x) - y_0(x) \quad (4.11)$$

$$\Delta_x(x) = \frac{d}{dx} \Delta(x) \quad (4.12)$$

$$\Delta_{xx}(x) = \frac{d^2}{dx^2} \Delta(x) \quad (4.13)$$

$$y_{0,1x} = \frac{d}{dx} y_{0,1} \quad (4.14)$$

Here $\Delta(x)$ is the transverse distance between the boundaries and gives the width of the strip. If this width does not vary along x , then $\Delta_x(x) = 0 = \Delta_{xx}(x)$.

The new transverse boundary conditions are

$$\tilde{\psi}(x, \tilde{y} = 0) = \psi_0(x), \quad \tilde{\psi}(x, \tilde{y} = 1) = \psi_1(x) . \quad (4.15)$$

A first observation is that the shape of the domain boundaries is reflected as a parametric forcing of the equation in the new coordinates. For example, for the simplest case of a meandering channel given by Eqs. (4.4) and (4.5) with $\phi = 0$, and $d_0 = d_1 = d$ (Fig. 4.1b):

$$\begin{aligned} \partial_t \tilde{\psi} = \partial_{xx}^2 \tilde{\psi} &+ \mathcal{F}(x) \partial_{\tilde{y}\tilde{y}}^2 \tilde{\psi} + \mathcal{G}(x) \partial_{x\tilde{y}}^2 \tilde{\psi} \\ &+ \mathcal{H}(x) \partial_{\tilde{y}} \tilde{\psi} + a\tilde{\psi} - \tilde{\psi}^3 \end{aligned} \quad (4.16)$$

$$\mathcal{F}(x) = \frac{1 + \left(\frac{d\alpha \sin(\alpha x)}{2}\right)^2}{(1+d)^2} \quad (4.17)$$

$$\mathcal{G}(x) = -\frac{d\alpha \sin(\alpha x)}{1+d} \quad (4.18)$$

$$\mathcal{H}(x) = -\frac{d\alpha^2 \cos(\alpha x)}{2(1+d)}. \quad (4.19)$$

Setting the right hand side of Eq. (4.7) to zero in order to seek for stationary solutions, and thinking of x as the time we can view Eq. (4.7) as a nonlinear evolution equation for a one-dimensional field with a ‘time’-periodic parametric driving due to the boundaries. Present knowledge on spatio-temporal chaos and pattern formation can in principle be applied to analyze the behavior of this resulting evolution equation. General results are not abundant, however. In the next Section further approximations will be introduced in order to facilitate the analysis and establish the existence of stationary spatially-chaotic solutions.

4.3 Single-transverse-mode approximation

For definiteness, in the rest of the chapter we will consider just null Dirichlet boundary conditions, that is the field ψ takes the value zero at the transverse boundaries: $\psi_0(x) = \psi_1(x) = 0$. In this case our model in the form of Eq. (4.7) has the trivial solution $\tilde{\psi}(x, \tilde{y}, t) = 0$. The stability analysis of this solution for the case of a rectangular domain of width l leads to an eigenvalue problem for the linearized equation. For $a > a_c = (\frac{\pi}{l})^2$ the eigenfunctions factorize into longitudinal ($\exp(ik_x x)$) and transverse ($\sin(k_{\tilde{y}} \tilde{y})$) modes: $\tilde{\psi}_{\lambda, \mathbf{k}}(x, \tilde{y}, t) = \exp(\lambda t) \exp(ik_x x) \sin(k_{\tilde{y}} \tilde{y})$, with $k_{\tilde{y}} = \frac{\pi}{l} m$, $m = 1, 2, \dots$, k_x real, λ satisfying the dispersion relation $\lambda = a - k^2$, and $k^2 = k_x^2 + k_{\tilde{y}}^2$. The unstable modes are then those satisfying the condition $k^2 < a$. The first unstable mode corresponds to $(k_x, k_{\tilde{y}}) = (0, \frac{\pi}{l})$, which becomes unstable at the critical value $a_c = (\frac{\pi}{l})^2$. The transverse modes are discretized in multiples of $\frac{\pi}{l}$ due to the boundary condition. If in addition, we require L -periodicity in the longitudinal coordinate x , k_x will be also discrete, but provided that $L \gg l$ this discretization will be much finer than the transverse one. The value of the parameter a controls how many modes are linearly unstable. If the transverse size l is small enough for the control parameter to satisfy the condition $(\frac{\pi}{l})^2 < a < (\frac{2\pi}{l})^2$, there would be just one linearly unstable transverse mode, with many associated longitudinal unstable modes. Close

enough to the instability threshold, we can try an approximate solution of the form $\tilde{\psi}(x, \tilde{y}, t) = A(x, t) \sin(\pi \tilde{y})$ and write an evolution equation for the amplitude $A(x, t)$ of the first transverse mode.

We are interested however in a domain which is not a rectangular strip but a undulated channel. The coordinate change bringing our domain into a rectangular one renders the variables non-separable and the linear problem is no longer solvable analytically. However, for small deviations from the uniform channel a perturbation scheme can be used. In the same vein as in the preceding paragraph we try, for our undulated domain, the ansatz $\tilde{\psi}(x, \tilde{y}, t) = A(x, t) \sin(\pi \tilde{y}) + \mathcal{O}(d_0, d_1)$, assuming that a is close to the threshold imposed by the small l , and that the size of the channel undulations is small. We call this approach a single-transverse-mode approximation (STMA).

Projecting Eq. (4.7) onto the single transverse mode present in the ansatz and neglecting higher order contributions we get the following evolution equation for the amplitude A :

$$\partial_t A = \partial_{xx}^2 A + \beta(x) \partial_x A + \omega^2(x) A - \frac{3}{4} A^3 \quad (4.20)$$

where

$$\beta(x) = \frac{\Delta_x}{\Delta} \quad (4.21)$$

and

$$\begin{aligned} \omega^2(x) = a &+ \frac{\Delta \Delta_{xx} - 2\Delta_x^2}{2\Delta^2} - \left(\frac{\pi}{\Delta}\right)^2 (1 + y_{1x} y_{0x}) \\ &- (2\pi^2 - 3) \frac{\beta^2}{6} \end{aligned} \quad (4.22)$$

We have checked that a more rigorous, but lengthy, approach based on a multiple scale expansion leads to the same result². The stationary patterns satisfy the time independent version of Eq. (4.20). In terms of the coordinate x considered as a time, one can view this spatial dynamical system as a parametrically forced nonlinear oscillator: domain undulations provide a periodic driving on the frequency of the system $\omega^2(x)$. In turn, $\beta(x)$ is a “dissipation” term which can be positive or negative depending on x . This x -modulation of β comes from the longitudinal variation of the vertical width. The integral of the “dissipation” $\beta(x)$ on one period of the oscillating boundaries $T = 2\pi/\alpha$ is $\int_{x_0}^{x_0+T} \beta(x) dx = \ln \frac{\Delta(x_0)}{\Delta(x_0+T)} = 0$. This shows that although system (4.20) is locally dissipative, it is effectively conservative over one period of the modulation. This implies, in particular, that the stroboscopic map associated with the system (4.20) is area preserving.

In the general case, Eq. (4.20) can be simplified by removing the dissipation term with the change: $A(x, t) = \exp\left(-\frac{1}{2} \int \beta(x) dx\right) \rho(x, t) = \rho(x, t) / \sqrt{\Delta(x)}$. The new equation reads:

$$\partial_t \rho = \partial_{xx}^2 \rho + \Omega^2(x) \rho - \frac{3}{4\Delta} \rho^3 \quad (4.23)$$

²For similar multiple scale analysis applied to fluid flows in a varying curved channel, see e.g. [81]

$$\Omega^2 = a - \left(\frac{\pi}{\Delta}\right)^2 (1 + y_{1x}y_{0x}) - \frac{\pi^2 + 3}{12}\beta^2 . \quad (4.24)$$

A particular case occurs when the transverse distance between the two channel borders does not vary along the longitudinal direction, so that the dissipation term vanishes identically, i. e. $\beta(x) = 0$. For the sinusoidal channel this happens when $\phi = 0$ and $d_0 = d_1 = d$ (Fig. 4.1b). In this case, the amplitude equation is reduced to

$$\partial_t A = \partial_{xx}^2 A + \omega^2(x)A - \frac{3}{4}A^3 \quad (4.25)$$

with

$$\omega^2 = a - \left(\frac{\pi}{1+d}\right)^2 - \frac{(\pi d \alpha)^2}{4(1+d)^2} \sin^2(\alpha x) . \quad (4.26)$$

When $\partial_t A = 0$, (4.25) is a dissipative Mathieu equation modified by the addition of a cubic nonlinear term or, equivalently, a parametrically forced Duffing oscillator. This equation is known to have chaotic solutions [82].

The general time-independent case of Eq. (4.20) [or Eq. (4.23)] reads:

$$\partial_{xx} A = -\omega^2(x)A + \frac{3}{4}A^3 - \beta(x)\partial_x A . \quad (4.27)$$

In the absence of undulations ($d_0 = d_1 = 0$) parametric forcing and dissipation vanish and the equation is both Hamiltonian and integrable. It has a region in phase space (A, A_x) close to the origin where motion is bounded and regular. Beyond the separatrices of the two saddle points $(A, A_x) = \pm 2/\sqrt{3}(a - \pi^2, 0)$, trajectories escape to infinity. When undulations are introduced, separatrices of the saddle points deform and may cross. It is well known that for perturbed Hamiltonian systems, separatrix intersections indicate the onset of chaos. In our system, in addition to chaotic bounded trajectories, separatrix intersections lead also to fractalization of the phase-space boundary dividing bounded and unbounded trajectories. Melnikov theory provide us with the tools to determine analytically the necessary conditions for separatrix intersection and the occurrence of chaos. Following [82], the Melnikov function $M(\theta)$ can be calculated for small d . For example, in the case $\phi = \pi$, $d_0 = d_1 = d$ one finds:

$$M(\theta) = f(a, \alpha) \sin(\alpha\theta) . \quad (4.28)$$

The fact that the function $M(\theta)$ has zeros as a function of θ indicates that separatrix intersection and chaotic behavior occur. Chaotic behavior appears for arbitrarily small sizes of the channel undulations. We expect similar behavior to occur for other values of ϕ , d_0 and d_1 .

To illustrate the chaotic behavior of the stationary STMA (4.27) we show in Fig. (4.2a) its numerical stroboscopic map. The dots are values of (A, A_x) at multiples of the forcing period $T = 2\pi/\alpha$ for a set of initial conditions. Several regions

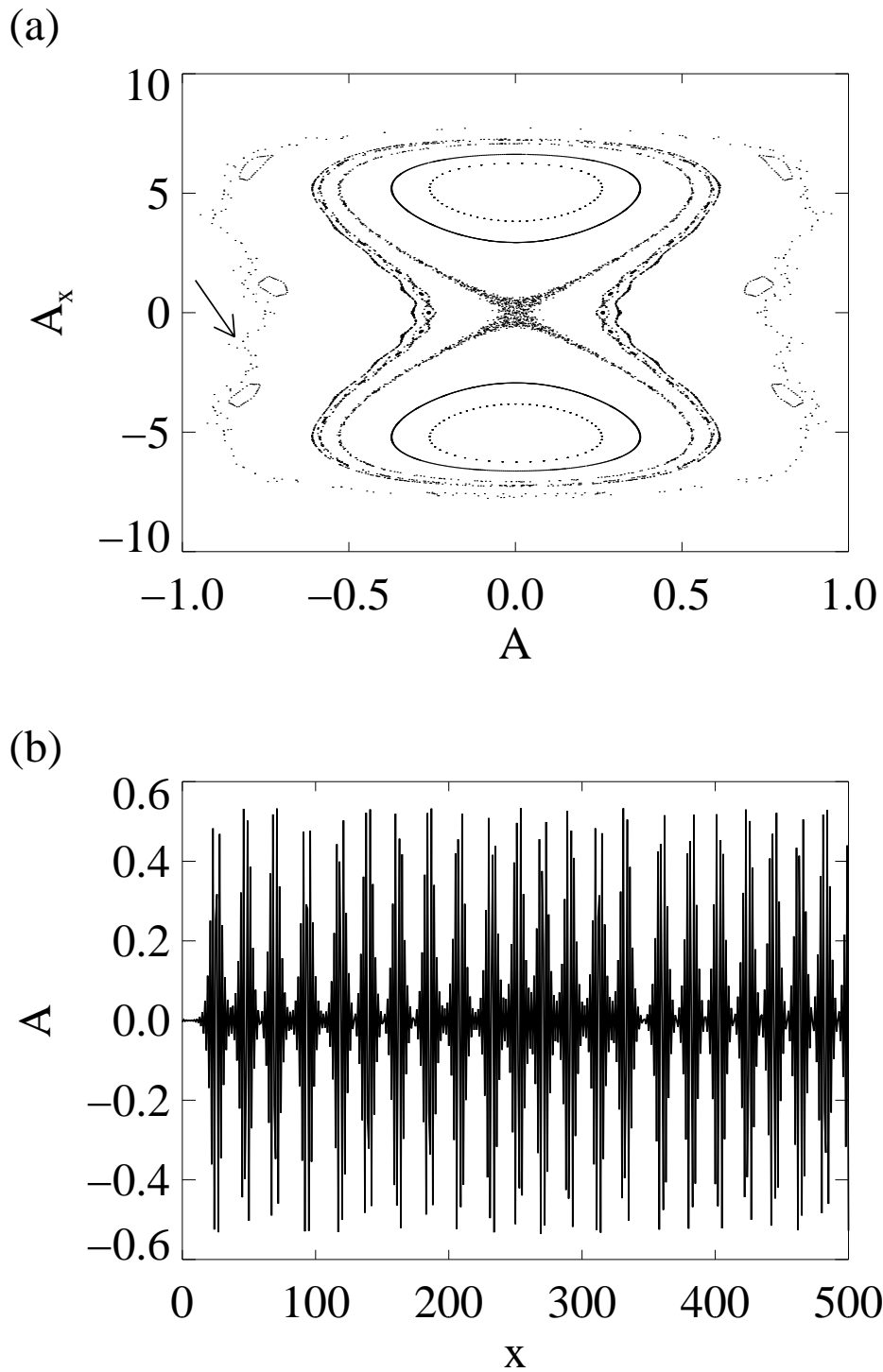


Figure 4.2: (a) Stroboscopic Poincaré map of the phase space of the system (4.27) for the values $d_0 = d_1 = 1$, $\alpha = 2\pi$, $a = 17$, $\phi = \pi$. KAM tori and chaotic trajectories inbetween are clearly seen. The arrow indicates the approximate location of the fractal boundary separating bounded and unbounded trajectories. (b) The chaotic configuration corresponding to the cloud of points surrounding the origin in the stroboscopic map.

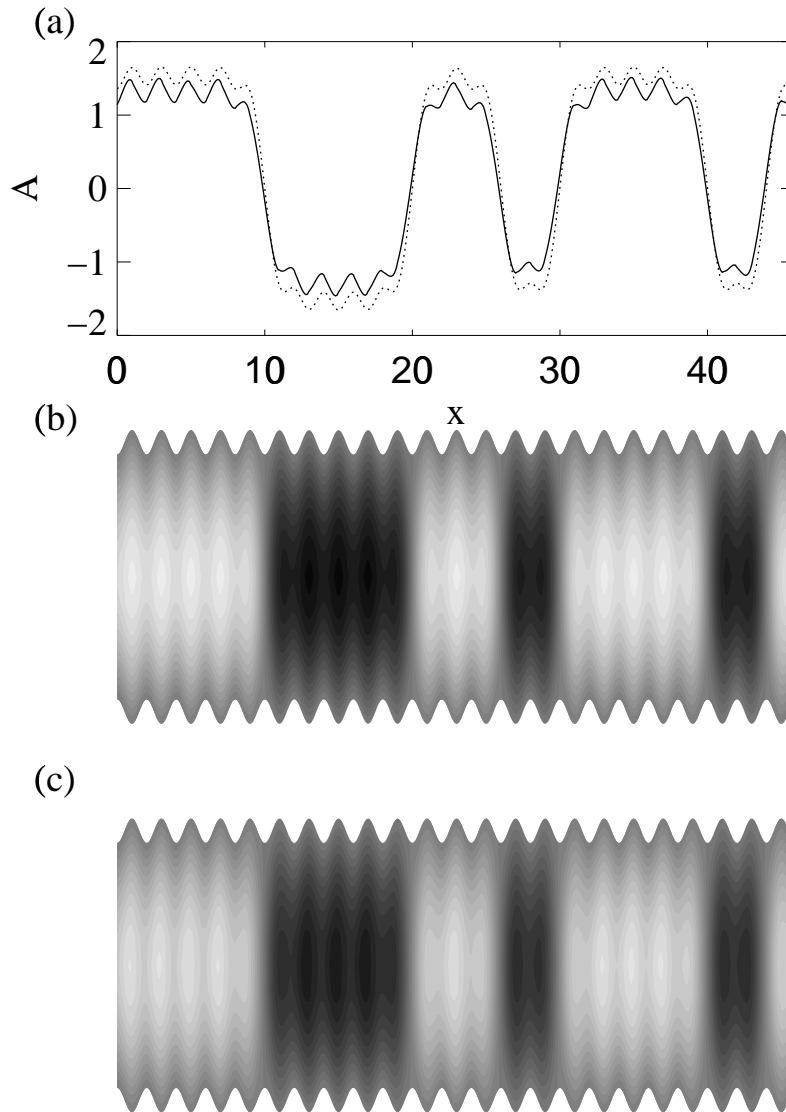


Figure 4.3: Stationary solution of the STMA (4.20) compared to a fully two-dimensional simulation of (4.1) for the parameter values $d_0 = d_1 = 0.1$, $\alpha = \pi$, $a = 10$, $\phi = \pi$. a) Stationary solution $A(x)$ of the STMA (dotted) and the on-axis values of the actual two-dimensional stationary solution $\psi(x, y = 0)$ (solid). b) The full two-dimensional solution of (4.1) represented on a gray-scale. White corresponds to the highest values of ψ and black to the lowest. c) Reconstruction of the two-dimensional field from the STMA ($\psi(x, y) = A(x) \sin(\pi \tilde{y})$) on the same gray-scale as in b).

dominated by chaotic trajectories and separated by KAM tori (the closed curves corresponding to quasi-periodic solutions) are clearly recognized in the picture. Also, the approximate location of the fractal boundary separating bounded trajectories from those escaping to infinity is pointed by an arrow. Melnikov analysis also implies the existence of a dense set of unstable periodic orbits in the vicinity of the separatrix intersection on both sides of the fractal boundary mentioned before. These periodic orbits and the fact that they constitute a skeleton of the chaotic trajectories, are important for our analysis because the periodic boundary conditions in the x -direction select them out from the uncountable many other possible solutions of Eq. (4.27).

4.4 Numerical STMA and two-dimensional time-integrations

In the previous section, we have shown both analytically and numerically that simple undulated boundaries may induce spatially chaotic steady solutions in our simple model (4.20). In this section, we discuss the accuracy and range of validity of the STMA and the physical relevance of its solutions by comparing with the numerical integration of the full model (4.1).

In the first place, we discuss the results of such integration for the particular case $\phi = \pi$ and $d_0 = d_1 = d$. Starting from random initial conditions the system, after a time long enough, settles in a disordered stationary configuration, as shown in Fig. (4.3). There we present the stationary configuration $A(x) \equiv A(x, t \rightarrow \infty)$ obtained by direct integration of Eq. (4.20). In the same plot, a longitudinal cross section of the asymptotic field obtained from a simulation with the full two-dimensional model is shown for comparison. We use as the initial condition of the two-dimensional problem the solution from the STMA for the same parameter values, $\psi = A(x) \sin(\pi \tilde{y})$, to provide an approximate stationary solution to Eq. (4.1). After a short time of adjustment, the system settles in a stationary state that is very close to the initial approximation. The full two-dimensional field and its reconstruction from the STMA are also shown in Figs. (4.3b) and (4.3c), respectively. This figure reveals a strikingly accurate fit of the STMA solution and the complete field simulation, a strong indication of the validity of the approximation as a tool for analysis. The maximum absolute error of the approximate solution is of the same order of magnitude in both the undulated channel and a rectangular-domain test-case. This suggests that the error is mainly due to the truncation at the first linear transverse mode, but not to the peculiarities of the curved boundaries.

The accuracy of the STMA, $A(x, t) \sin(\pi \tilde{y})$, breaks down when the channel width increases or when strongly non rectangular domains are considered. Nevertheless, we have also performed direct simulations of Eq. (4.1) for this last case. An example of the typical behavior is shown Fig. (4.4) for boundaries defined by $d_0 = d_1 = 1.0$, $\alpha = \pi$, $a = 20$, $\phi = \pi$. Notice that the resulting stationary configuration displays the same qualitative features of the STMA solutions: disordered distribution of kinks randomly pinned at some of the narrows of the channel. This is an evidence of the fact

that undulating boundaries may also be the source of stationary spatial chaos in a two-dimensional system (4.1) beyond the regime well described by a single transversal mode.

The results in Figs. (4.3) and (4.4) illustrate the physical mechanism behind the emergence of spatial chaos in our system. Let us remember that Eq. (4.1) evolves to minimize the potential (4.3). This minimization requires to reduce as much as possible the length of the interfaces between ψ_+ and ψ_- . Following this tendency, an interface that links the opposite lateral banks of the channel and is far from any other interface will evolve to lock into one of the narrows of the channel, where it is shorter than in any other position. Detaching the interface from the bank of the channel would imply a temporary increase of the potential V due to the necessary proliferation of new interfaces. Such a potential increase is not allowed by the dynamics. Hence, the random occupation (arising from random initial conditions) of the narrows of the channel by kinks and anti-kinks finally builds up a spatially chaotic stationary configuration. This argument, based on kink and interface dynamics, clearly applies beyond the range of validity of the STMA, where we have analytically established the existence of spatial chaos, as evidenced in Fig. (4.4). With this mechanism in mind, we can also conclude that not all the chaotic trajectories presented in Fig. (4.2) will lead to spatial chaos stable in time: only those corresponding to an energetically favorable (a local minima of the potential V) distribution of kinks will be reached under time evolution. In particular the trajectory plotted in Fig. (4.2b) corresponds to a temporally unstable configuration.

Let us now try to get further insight about the chaotic nature of the irregular spatial structures described above. Periodic boundary conditions in the longitudinal direction always force the system to converge not to a chaotic spatial configuration, but to a periodic one which we have shown it may very well be of the maximal period. To justify the use of the chaotic qualifier we need to show that as the size of the system increases, these periodic configurations approach one that could be characterized as chaotic in some way. Of course, to numerically carry out this process we would need to consider very long channels. Unfortunately though, performing direct simulations on the fully two-dimensional model soon becomes computationally prohibitive as the number of the channel undulations increases. However, having demonstrated that the STMA accurately describes the qualitative features of the full model, we can concentrate our attention on the behavior of the approximate model Eq. (4.20).

In Fig. (4.5) we summarize the results from the numerical integration of Eq. (4.20) using the same parameter values as in Fig. (4.3) with the exception of the domain size which now is much larger. An asymptotically stable configuration is shown in a) while c) displays the projection of the trajectory in phase space (A, A_x) . The power spectrum of $A(x)$ plotted in Fig. (4.5b) shows the typical broadband feature characteristic of chaotic trajectories. As a further indication of the (approximately) chaotic nature of this configuration, we have shown in Fig. (4.6) the stroboscopic map constructed from the trajectory in Fig. (4.5). taking phase space points at ‘times’

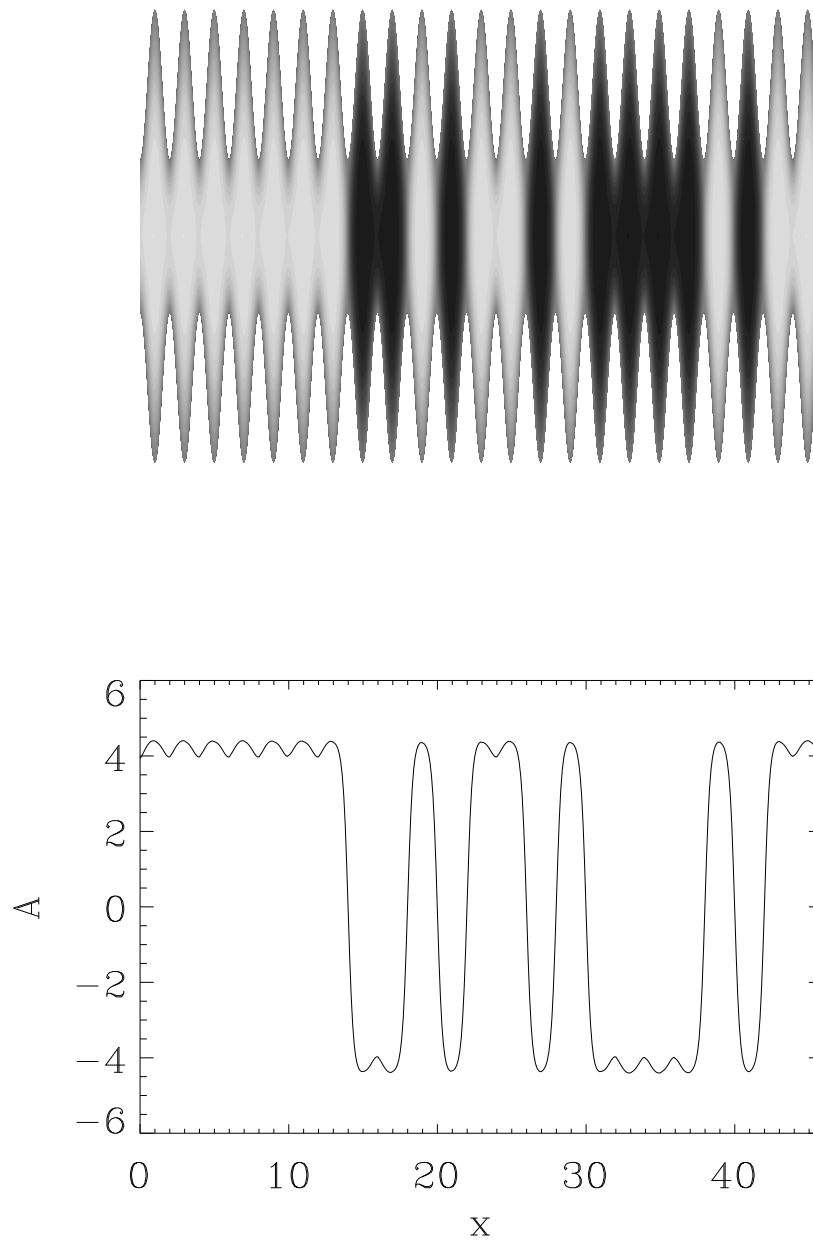


Figure 4.4: Two-dimensional steady state obtained by simulation of the system (4.1) starting from random initial conditions. The amplitude of the field on the channel axis is shown in the lowest panel. Parameter values: $d = 1.0$, $\alpha = \pi$, $a = 20$, $\phi = \pi$.

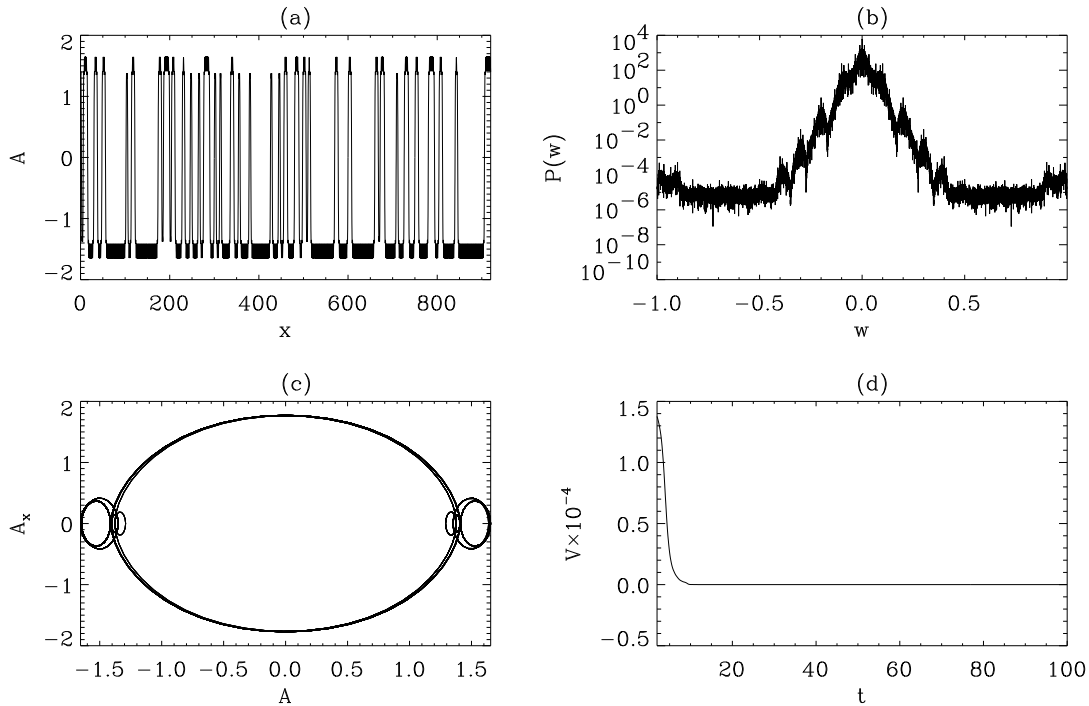


Figure 4.5: One-dimensional solution of the system (4.20) showing a steady chaotic configuration, its spatial power spectrum, the trajectory in the projected phase space (A, A_x) , and the time evolution of the Lyapunov functional, showing that this is an attracting configuration. Parameter values as in Fig. (4.3), but for a longer system

integer multiples of T . This map reveals an incipient self-similar fractal structure, also common in chaotic trajectories. All these facts together give compelling evidence that the trajectory, although L -periodic by construction, develops chaotic features as system size increases.

Finally, as an illustrative measure of the asymptotic stability of this solution, Fig. (4.5d) displays the value of the Lyapunov potential $V[\psi]$ evaluated along the time evolution of the field $\tilde{\psi}(x, \tilde{y}, t) = A(x, t) \sin(\pi \tilde{y})$. The functional decreases in time, confirming the consistency of the STMA with the exact dynamics of Eq. (4.2), and the potential asymptotically approaches a constant value indicating that the field has reached a local minimum of V .

4.5 Conclusions

We have given evidence of the existence of stationary, stable, longitudinally chaotic spatial configurations induced by undulated boundaries in a simple two-dimensional

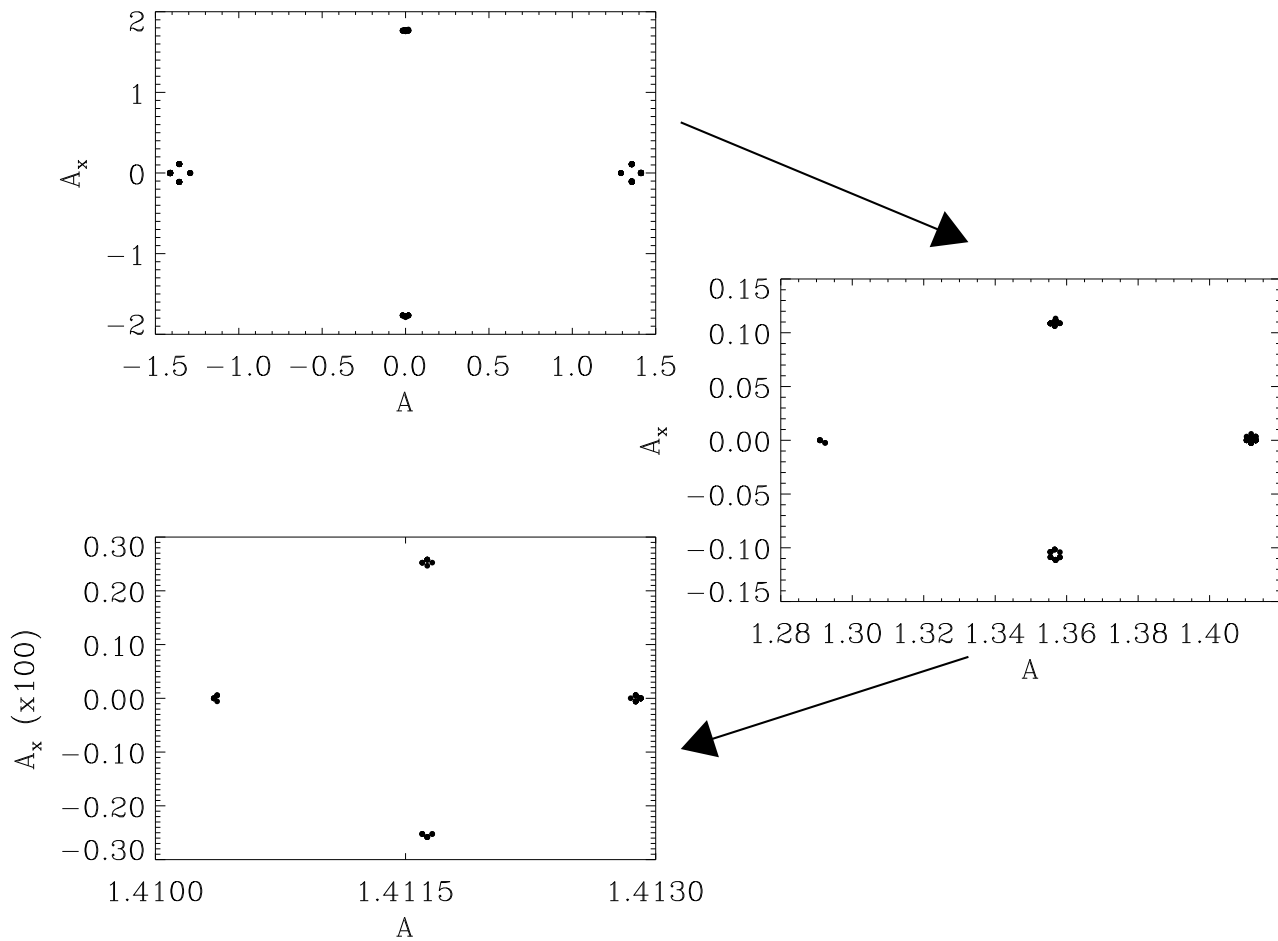


Figure 4.6: Stroboscopic map of the trajectory shown in Fig. (4.5). Two successive amplifications are shown, displaying a self-similar structure typical of a fractal.

reaction-diffusion model that does not otherwise display any kind of chaos. We have demonstrated that these type of boundaries can be convincingly mapped into spatially-periodic parametric modulations in a one-dimensional approximation to the original system. In a dynamical systems approach to the study of stationary solutions, these modulations play the role of a temporal time-periodic forcing capable to drive a nonlinear second-order ODE into chaotic behavior. The diffusive character of our original model ensures precisely that the relevant ODE is in fact, second order and that the presence of chaotic stationary solutions is expected at this level of approximation. Previous results exist[54, 73, 74] showing that spatial periodic modulation of some parameters intrinsic to the dynamics may originate spatial chaos in relatively simple reaction diffusion models. However, to our knowledge, the present is the first example in which an straightforward dynamical systems approach is used to establish the existence of disorder in two-dimensional systems due to the influence of the boundaries.

The consequence of our analysis is that chaotic configurations should *exist* in virtually any of the experimental systems commonly used to study pattern formation, provided that boundary conditions such as those studied here are imposed. The *stability* of these chaotic configurations should be discussed in each particular case. While in our model stability comes from the tendency of the dynamics to minimize (4.3) therefore minimizing interface lengths and leading to pinning of these interfaces to the narrows of the channel, the mechanism for stability in other systems may be different. Apart from the direct application to pattern forming systems, the idea of boundary-generated spatial chaos could be speculatively transferred to other non-linear extended dynamical systems of interest. For example, it is possible that low Reynolds number fluid flows through a space-periodically perturbed pipeline or even through a realistic channel of shape similar to the ones considered here can display frozen spatial chaos [70]. A numerical search for this manifestation of “frozen turbulence” at the level of Navier-Stokes equations is currently in progress. We expect this observation to promote also experimental work both in the area of pattern formation and in hydrodynamics.

Chapter 5

Time averages of spatio-temporal chaos: a boundary effect

Chaotic pattern dynamics in Faraday waves, in rotating thermal convection, and in electroconvection, show ordered time averages. We suggest a simple universal mechanism underlying this phenomenon, here exemplified by the Kuramoto-Sivashinsky equation in a bounded domain. In agreement with experimental observations, time-averaged patterns obtained from the Kuramoto-Sivashinsky equation recover global symmetries broken locally by the chaotic fluctuations, and the averaged amplitude is strongest at the boundaries and decays with increasing distance to them. The law of decay is found and explained. The wavenumber selected by the average pattern is obtained as a function of system size and the different behavior observed between the central and boundary regions is discussed¹.

¹This Chapter corresponds to *Time averages of spatio-temporal chaos: a boundary effect*, by V.M. Eguíluz, P. Alstrøm, E. Hernández-García and O. Piro, Phys. Rev. E **59**, 2822 (1999).

5.1 Introduction

Beginning with Poincaré [83, 84, 85] and after the re-discovery of the theory to the physicists by Lorenz [86], more than thirty years ago, and subsequently by Ruelle and Takens [87], in the seventies, much effort has been dedicated towards the development of the Theory of Dynamical Systems. Nowadays, this Theory is quite well established even though its frontiers are still growing. However, in the last decades a lot of work has been dedicated to the understanding of extended dynamical systems. This represents a shift of the focus from the study of the evolution of one quantity (or a few) to the evolution in time of a spatially extended field. The evolution equations for the former case are a set of ordinary differential equations, while for a field we need in general, partial differential equations. Since a field is a function of the point \mathbf{x} within a continuous domain, such evolution equations represent infinite dimensional dynamical systems. This radical change in focus has been made possible in part by the tremendous growth in computational power during the recent years which allows us to deal with infinite dimensional systems. Numerical simulations are intended to provide us with a first insight in the dynamics of the systems, but sometimes they become the only available tool due to the difficulty of the analytical approach.

An important issue in the theory of dynamical systems is the appearance of *chaos*. A chaotic regime is roughly characterized by the divergence of initially close trajectories. Initial conditions that differ very little, can have an absolutely different evolution. The analogue of chaos in the extended case is *spatio-temporal chaos*, where the solutions are not only chaotic in time but they are also disordered in space. In this thesis we concentrate on systems that show some kind of spatio-temporal chaotic regime.

In order to bridge simulations to analysis, it is important to concentrate on the behavior of very simple model equations with the hope that universality can make relevant these results. However, the need of simplified models also steams from the computational limitations. When dealing with simplified theoretical models, it is not a trivial question how we can compare the theoretical results to experiments in order to validate the models. The problem is that many of the available theoretical predictions in the literature are not accessible to the experimental work, and viceversa. For example, Lyapunov exponents can be calculated numerically and analytically in many situations. However, the practical measurements of phase-space quantities in experiments have faced great problems when the number of degrees of freedom is moderately large [88]. In this context, it seems reasonable to expect that a statistical approach could fill this gap between models and experiments.

Following a suggestion by Golubitsky [89], several experimenters have investigated the behavior of time averages of chaotic wave patterns. At the beginning researchers did not pay much attention to the temporal average of extended fields. On the one hand, when one is doing numerical simulations one easy way to avoid complications is to take periodic boundary conditions, to make the theoretical analysis and the implementation of the numerics much simpler to carry. In these circumstances, and if the evolution equations have translational symmetry, all the points are equivalent, and on average all will have the same value. Thus, the temporal average does not show any spatial structure, the average is a constant function in such cases. On the

other hand, it is usually assumed that the boundaries only affect a region close to them so that if the domain is big enough the bulk dynamics is not affected by the boundaries. However these two assumptions do not apply when imposing boundary conditions that break the translation symmetry (e.g Dirichlet boundary conditions, where a value of a field is specified at the boundary) and moderate domain sizes. There are situations in which the translation symmetry is spontaneously broken (e.g. Rayleigh-Bénard convection), but this case will be not studied here.

The measurements of the average were done first on the Faraday experiment where an open container filled with a fluid is shaken vertically. This system first undergoes a transition from a flat surface to an ordered structure (usually an oscillating square pattern) when the amplitude is increased. When the amplitude is further increased, a spatio-temporally chaotic regime is reached. The time averages were done in this regime. The results are in some way surprising, since a structured pattern is recovered on average. The symmetries of this pattern are related to the global symmetries of both the container and the evolution equations, rather than to the local symmetries.

However, so far no complete theoretical explanation for this phenomenon was given. The purpose of this work is to present a universal mechanism to explain for this effect. We will show that all we need to reproduce the same behavior found in the experiments is the co-existence of spatio-temporal chaotic regimes and boundary conditions that break the translational symmetry. Our program consists of performing simulations on a generic model of spatio-temporal chaos, the Kuramoto-Sivashinsky equation, subject to different types of boundary conditions. We present results about the time average for these conditions and for several system sizes, and we study how the number of oscillations, wave lengths of the patterns, and amplitudes depend on the system size.

In the following Section, we present previous experimental results, where time averages on a spatio-temporal chaotic regime give a structured pattern. We will concentrate mainly on the Faraday instability, but similar results have been also found for other systems. In the last Section of this Chapter we present our results on time averages of the Kuramoto-Sivashinsky equation [90].

5.2 Previous results

Many investigators concerned with patterns in non-equilibrium systems have turned their attention to the problem of *spatio-temporal chaos*. Roughly speaking, the concern here is with situations in which the range of spatial correlations is small compared to at least one dimension of the system. Given the remarkable progress made in analyzing (a) the chaotic behavior of small systems with only a few degrees of freedom, and (b) the steady patterns of extended non-equilibrium systems, it is natural to try to extend the relevant concepts to chaotic extended systems. Indeed, a major body of experimental literature has appeared on a great variety of systems, including Rayleigh-Bénard convection [91, 92, 93], rotating convection [94, 52], Turing patterns [95], parametrically excited surface waves [96, 97], convection in nematic liquid crystals [98, 99, 100, 101], binary mixtures [102, 103], rotating films [104], and Taylor-Couette flow [105].

In parallel with this experimental work, there has been a considerable numerical and an analytical effort, much of it directed at model equations such as the complex Ginzburg-Landau equation, which is believed to provide a plausible approximation to the physics for some systems in which spatio-temporal chaos occurs close to the onset of the basic pattern. The Kuramoto-Sivashinsky equation has provided another approach to modeling, as have provided coupled map lattices and other discrete models. The theoretical work is now so extensive and diverse that it is impossible to reference adequately; it is thoroughly discussed in a lengthy review by Cross and Hohenberg [53].

An alternative approach to the dynamical systems methods is using the basic statistical character of the phenomena, despite their deterministic origin [106]. Experimental studies of the chaotic pattern dynamics in Faraday waves [9, 107], in rotating thermal convection [108], and in electro-convection [109], reveal that spatio-temporal complex patterns can have surprisingly ordered time averages. The form of these average patterns (square, circular, hexagonal) is determined by the underlying symmetry [89, 110, 111, 112] imposed by the boundary conditions. It is shown that the instantaneous images present locally a determined symmetry that does not depend on the global symmetry of the container. Compare for example Fig. 5.3.b and 5.4.b. Taken an instantaneous image only from the central region of the rectangular domain and another from the circular one, they are indistinguishable, i.e. it is not possible to decide what picture corresponds to what boundary. Experimental observations lead to the conclusion that although the instantaneous patterns fluctuate chaotically in time, they are biased towards an average pattern because they have short-lived patches spatially in phase with this average. Thus, there are some regions that are in phase with the average for a short period of time, and the rest of the regions are not correlated with the average pattern. These patches-in-phase appear in different places of the container at different times and, in average, give rise to the structure of the time averaged pattern. This phase rigidity seems to come from the boundaries. The amplitude of the time-averaged pattern depends on the system size and control parameters. It is strongest near the sidewalls, and decays with increasing distance from the sidewalls and with increasing fluctuations about the ordered averaged state.

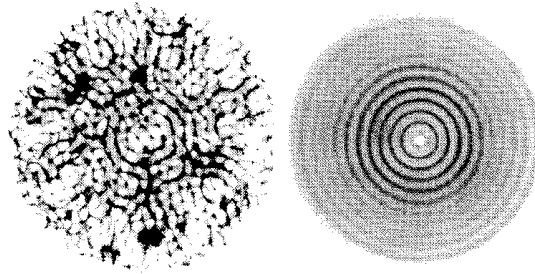


Figure 5.1: Instantaneous (left) and time-averaged (right) shadowgraphs of interfacial wave patterns in a circular cell. these chaotic Faraday wave patterns are produced by a vertical oscillation of the cell at 81 Hz, with a driving amplitude 40% above that required for the wave onset. The structured average pattern indicates a significant degree of phase rigidity despite the spatio-temporal chaos.(From [113])

For very large containers the ordered average pattern exists only near the sidewalls.

We suggest a simple universal mechanism underlying this phenomenon, here exemplified by the Kuramoto-Sivashinsky equation in a bounded domain. In agreement with experimental observations, time-averaged patterns obtained from the Kuramoto-Sivashinsky equation recover global symmetries broken locally by the chaotic fluctuations, and the averaged amplitude is strongest at the boundaries and decays with increasing distance to them. The law of decay is found and explained. The wave number selected by the average pattern is obtained as a function of system size and the different behavior observed between the central and boundary regions is discussed.

In the following, we describe experimental results on average patterns. For simplicity we will focus on the Faraday experiment, but similar results apply to other experimental systems.

5.2.1 Faraday waves.

When a fluid layer with a free surface is subjected to a vertical oscillation of amplitude A greater than a critical value A_c , it is unstable with respect to interfacial standing waves. This instability was first studied and described by Faraday [114] and Lord Rayleigh [115]; the linear stability theory was developed by Benjamin and Ursell [116]. This instability of the surface is of the *parametric* type (in the sense that the external forcing appears as a modulation of the parameters, in this case the acceleration of the gravity \vec{g}) and, consequently, it is usually called *parametrically driven surface waves*.

Under some assumptions, the linearized equations of motion reduce to the standard form of the Mathieu equation. The solution has stability tongues in the parameter space defined by drive acceleration vs wave number. The wave frequencies ω within the tongues occur at $\omega = n\Omega/2$ where Ω is the drive frequency and n is a positive integer. The $n = 1$ sub-harmonic response is selected due to its lower

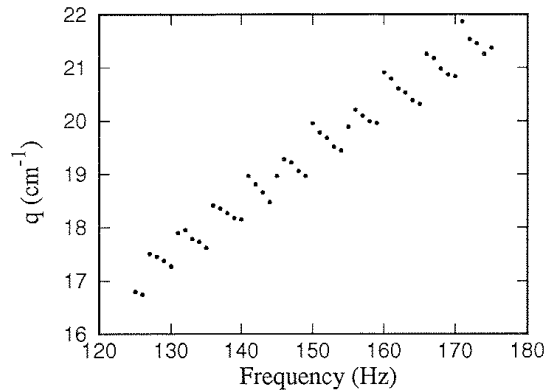


Figure 5.2: Mean wave number of the average pattern, showing the phenomenon of statistical quantization.(From [113])

threshold, after the effect of viscous dissipation is included in the theory. Thus, the frequency of the standing waves is half the driving frequency.

Patterns of various symmetries have been observed in large aspect ratio systems (large lateral size of the fluid layer compared to the wave length of the waves) depending on the driving frequency and fluid properties (viscosity, surface tension and density). One typically observes patterns of standing waves (parallel stripe patterns), two waves at a 90° angle (square patterns); it is only in recent years that a variety of additional patterns -some with quasi-periodic rather than periodic long range order- have been observed, as for example, hexagonal, eightfold and tenfold patterns [118, 119]. For example, the case of square pattern could be expressed as

$$\zeta(x, y) = a[\cos(\kappa x) + \cos(\kappa y)] , \quad (5.1)$$

where the local surface height is denoted by $h(x, y, t) = \zeta(x, y) \sin(\omega t)$, plus higher harmonics. In the linear approximation, the waves obey a dispersion relation, which relates the wave frequency ω to their wave number κ

$$\omega^2 = [g\kappa + \frac{\sigma}{\rho}\kappa^3] \tanh(\kappa h) \quad (5.2)$$

where σ is the surface tension, ρ is the fluid density, g is the local gravitational constant, and h is the mean fluid depth. For a deep fluid ($h \rightarrow \infty$) the relation simplifies to

$$\omega^2 = \frac{\sigma}{\rho}\kappa^3 + g\kappa. \quad (5.3)$$

For long wavelengths, i.e. for small wave numbers (as long as the approximation $\tanh(\kappa h) \approx 1$ remains valid), the gravitational force on the displaced fluid (displaced away from the flat surface, equilibrium) acts as the restoring force of the wave. In

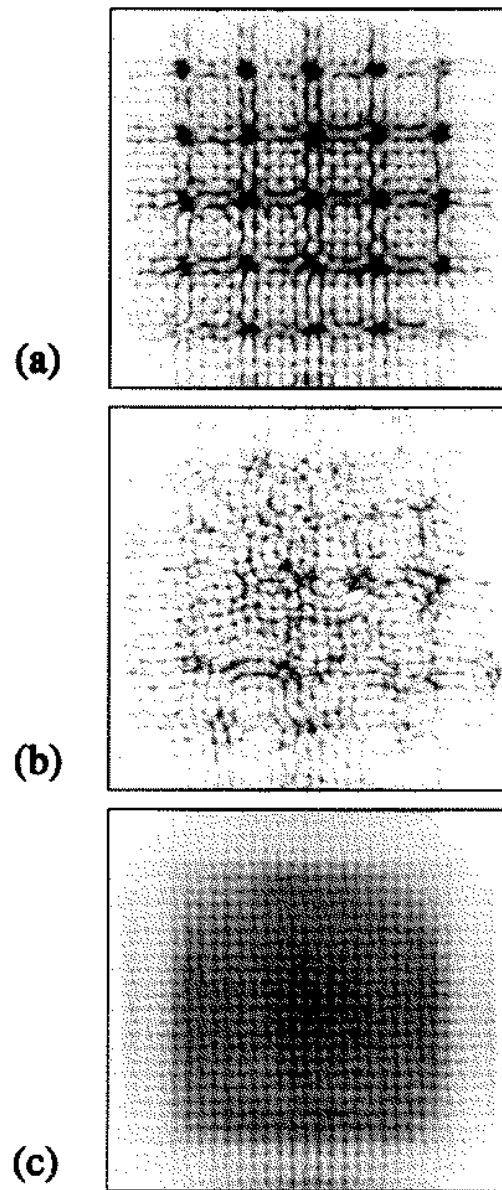


Figure 5.3: Instantaneous and time-averaged images for square geometry. (a) Shadowgraph image of the time-independent wave pattern near onset ($\epsilon = 0.05$). The wave pattern is approximately a mixed mode with mode numbers (29,6). (b) Instantaneous image of a chaotic pattern ($\epsilon = 0.10$). (c) Time average over 12 800 images ($\epsilon = 1.0$). the average reveals the probability distribution of antinode positions. High intensities are shown dark. (From [117])

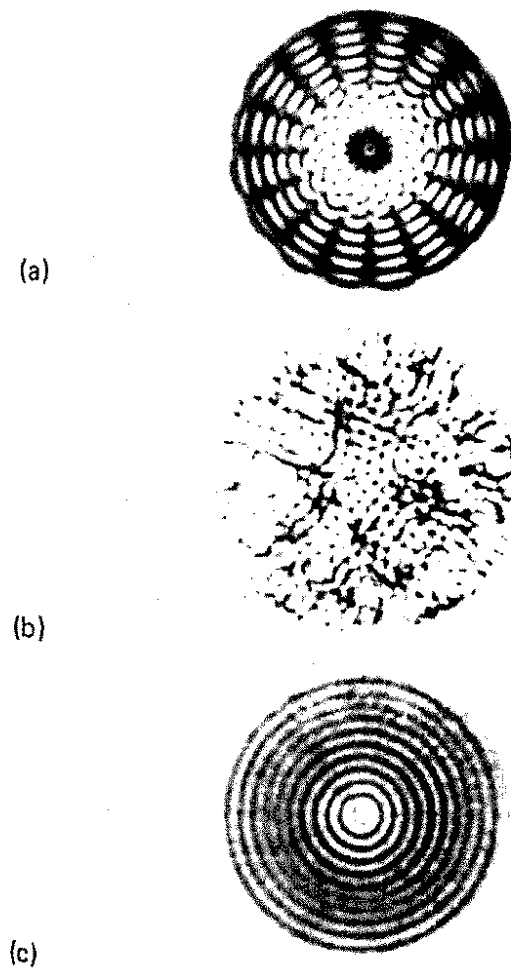


Figure 5.4: The instantaneous and time average for circular geometry. (a) Shadowgraph image of time-independent wave pattern near onset ($\epsilon = 0.01$). (b) Instantaneous image of a chaotic pattern. (c) Time average over 12 800 images ($\epsilon = 0.5$). (From [117])

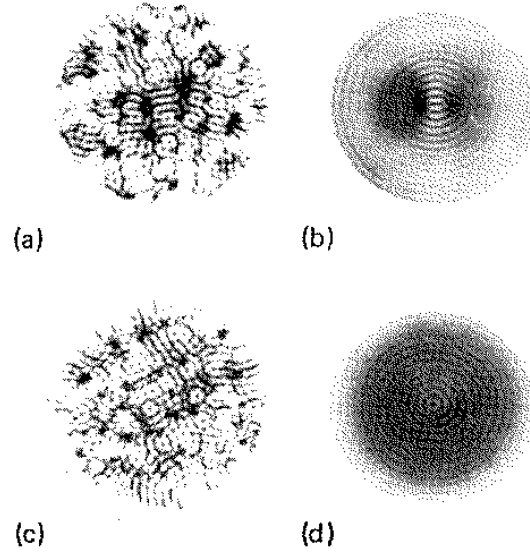


Figure 5.5: Instantaneous [(a) and (c)] and time-averaged [(b) and (d)] images in a cell with ellipticity 0.02. [(a) and (b)] $\epsilon = 0.15$; [(c) and (d)] $\epsilon = 0.50$. The asymmetry of the resultant image is amplified at the lower drive amplitude, and is less pronounced at higher ϵ . (From [117])

that case the first term in (5.2) dominates. Such waves are called *gravity waves*.

$$\omega^2 = g\kappa. \quad (5.4)$$

In the opposite case of short wavelengths, the effect of gravity can be neglected, and the restoring force due to the surface tension dominates, i.e. the second term of (5.2) dominates. For these waves, called *capillary waves*, the dispersion relation is

$$\omega^2 = \frac{\sigma}{\rho}\kappa^3. \quad (5.5)$$

When the amplitude A is slightly increased, the surface pattern becomes somewhat disordered by the occurrence of moving defects. These defects result from the transverse amplitude modulational (TAM) instability. For example, for water this happens at such a small increase of A that, in reality, a perfect square pattern is not seen. Nonlinear wave interactions become important and the defects dominate. The wave pattern becomes random in appearance and the flow is spatio-temporally chaotic. However, on time averaging the motion of the surface over many oscillation periods, the square pattern remains discernible. This indicates that the long-range correlations of the capillary waves are not destroyed.

It is worth noting that the wavelength selected in the first instability can be changed varying the frequency of oscillation ω , thus changing at the same time the

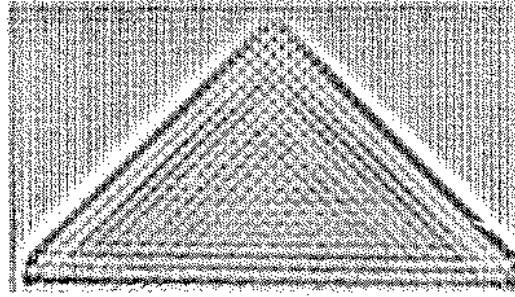


Figure 5.6: Enhanced time-averaged image observed in a triangular cell ($\epsilon = 1.5$). (From [117])

aspect ratio $\Gamma = \frac{\lambda}{L}$, being $\lambda = \frac{2\pi}{\kappa}$. Changing the container or the fluid is thus not needed in order to change the aspect ratio. The second important aspect we want to stress is that the control parameter is given by the amplitude of acceleration. For a harmonic oscillation of amplitude A and frequency ω , it is $a = A\omega^2$. Once the frequency is selected, the control parameter is simply the amplitude of oscillation A . It is useful to define the distance to threshold as $\epsilon = \frac{a-a_c}{a_c}$, where a_c corresponds to the critical amplitude of instability.

The experimental method to get the instantaneous images is based on screenless shadowgraph optics [120]. Basically, a collimated beam of white light is sent vertically from below through the fluid surface. The light is collected and imaged onto a video camera. The resulting images are bright only where the local surface slope is close to zero. The condition for a ray to reach the camera is $|\vec{\beta}| < \Lambda$, where $\vec{\beta} = \vec{\nabla}\zeta$, all other rays being lost. It is important to note that *the instantaneous optical images obtained with this technique are not linear in the surface wave field*. The images are sharply peaked functions which highlight the local extrema of the surface. An algorithm that approximates this optics is given by the following formula:

$$I(\vec{x}, t) = I_0 \Lambda^2 / (\Lambda^2 + \beta^2) \quad (5.6)$$

where $\beta^2 = \vec{\beta} \cdot \vec{\beta}$.

5.2.2 Experimental observations

As stated before, our interest is focused on the time average of the wave patterns in the spatio-temporal chaotic regime. The main results of these experiments are summarized in the figures. The most striking observation is that structure is found in the time-averaged images of chaotic wave patterns.

- The symmetry of the average patterns is determined by the symmetry of the boundaries, despite the fact that the instantaneous patterns are similar, as explained in page 8. See Fig. (5.1,5.3-5.6)

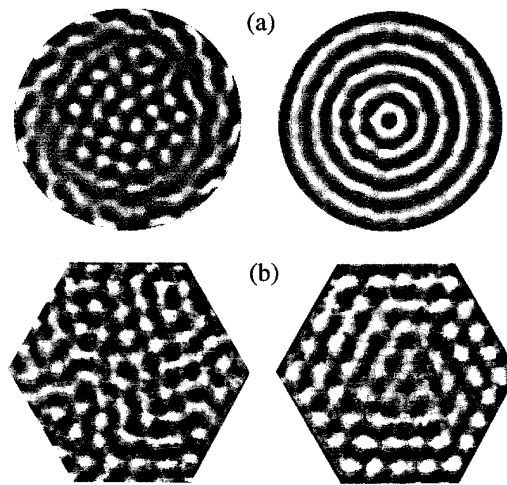


Figure 5.7: Rotating thermal convection. The instantaneous (left) and time-averaged (right) pattern in rotating Rayleigh-Bénard convection in (a) a cylindrical container and $\epsilon = 0.053$ with water; (b) hexagonal container and $\epsilon = 0.08$ with carbon dioxide. (From [108])

- The system continually fluctuates about the mean, but never becomes fully ordered.
- The amplitude of the average image is a decreasing function of the degree of disorder in the instantaneous pattern; as the drive amplitude is increased, the contrast in the average images decreases.
- The profile of the average pattern is oscillatory and thus, the number of oscillations for a given parameters is an integer. This number of oscillations has the same value for a range of the control parameters but suddenly jumps to the next integer when a new oscillation appears. The jumps correspond to integral changes of the total phase difference of the base pattern across the cell. This magnitude is plotted in Fig. (5.2), where the number of oscillations is the wave number q divided by the length L of the domain. The mean wave number of the average images is observed to have non-hysteric jumps as a function of drive frequency.
- Not only these features apply to the Faraday experiment, but very similar results have been obtained in rotating thermal convection [108] (see Fig. (5.7,5.8)) and electro-convection [109]. Thus giving some clue about a universal signature.

Given the general features of average patterns suggested by experiments, it seems surprising that their possible existence and characterization have not been addressed within the standard model equations displaying spatio-temporal chaotic states [53].

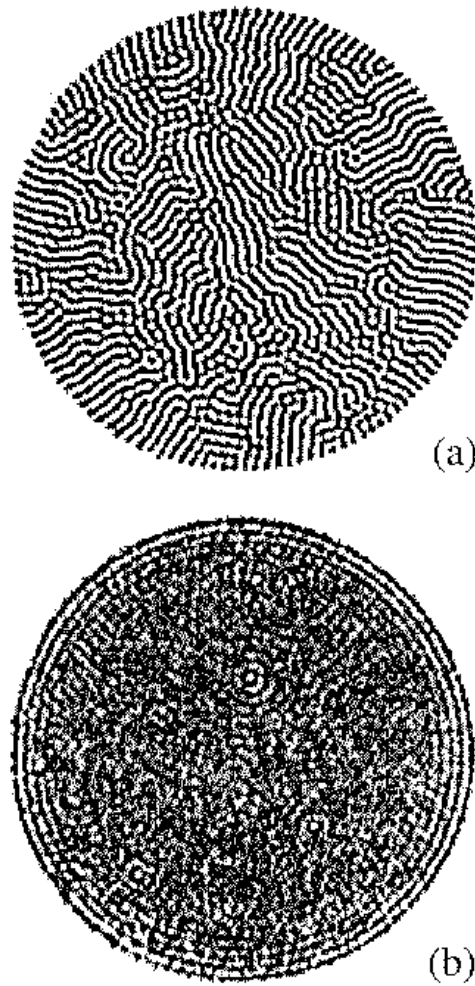


Figure 5.8: The instantaneous (top) and time-averaged (bottom) patterns in rotating Rayleigh-Bénard convection in a cylindrical container, $\epsilon = 0.10$ with CO_2 . The time average is obtained from 720 images. Note that the local orientation of the rolls close to the boundaries is perpendicular in the instantaneous image and they form concentric rings in the average. (From [108])

One possible reason for this is that periodic boundary conditions are usually considered in theoretical studies. In such situation spatial translational invariance homogenizes out any time average (unless some unexpected ergodicity breaking takes place). Boundary conditions breaking translational symmetry, as in the experiments, are thus needed to obtain nontrivial average patterns. Motivated by this fact, in the next chapter we will consider the Kuramoto-Sivashinsky equation, one of the prototype equations showing spatio-temporal chaos, in bounded one and two dimensional domains.

5.3 Time averages on the Kuramoto-Sivashinsky equation

In this chapter, we will consider the Kuramoto-Sivashinsky equation, one of the prototype equations showing spatio-temporal chaos, in bounded one and two dimensional domains. We show that ordered average patterns do appear, despite the strong fluctuations, and we discuss the universal aspects of wave number selection and amplitude variations. More directly, our analysis of average patterns may be relevant and suggestive for experiments on phase turbulence in convection cells [121], fluids flowing down an inclined wall [122], and flame front propagation [123, 124].

5.3.1 The Kuramoto-Sivashinsky equation.

The Kuramoto-Sivashinsky equation [121, 125] is perhaps the simplest partial differential equation exhibiting spatio-temporal chaos. The mechanism for generating the chaotic behavior is the combination of a linear instability and a nonlinear term which tends to bring energy from the long wave length modes to the small wave length modes where it is dissipated. The linear instability is responsible for creating ‘cells’ with lengths centered around the maximally unstable scale and the nonlinear term causes ‘tip splitting’ of large cells with subsequent squeezing out of small cells. The equation in one dimension has the form:

$$h_t = -h_{xx} - h_{xxxx} + (h_x)^2, \quad (5.7)$$

where $h = h(x, t)$ is a real function, $x \in [0, L]$, and the subscripts stand for derivatives. In two dimensions the spatial derivative is replaced by a gradient and the second derivative by a Laplacian. The only control parameter for the equation is the length of the domain L ; prefactors to the terms in Eq. (5.7) can be scaled out. It is shown to describe the temporal phase of coupled chemical oscillators [121]. It also describes the behavior of other extended pattern forming systems, such as flame fronts [125] and fluid interfaces [122]. An equivalent equation for $u = h_x$ can be obtained by taking the derivative of Eq. (5.7) with respect to x ,

$$u_t = -u_{xx} - u_{xxxx} + 2uu_x. \quad (5.8)$$

In this form the model is reminiscent of the Burgers equation, but in contrast with the Burgers equation, it displays a sustained chaotic behavior.

Equation (5.7) possesses translational symmetries ($h \rightarrow h + h_0$, $x \rightarrow x + x_0$) a reflexion symmetry ($h \rightarrow h$, $x \rightarrow -x$), and an infinitesimal Galilean symmetry ($x \rightarrow x + 2vt$, $h \rightarrow h + vx$). The asymmetry of the equation under $h \rightarrow -h$ induces growth of h predominately in one direction (that depends on the sign of the nonlinear term). In large systems with homogeneous initial conditions the system evolves to an ‘equilibrium’ state in which the interface, in the case of flame fronts or fluid interfaces, moves upward (or downward, depending on the sign of the nonlinear term) with a constant velocity and with fluctuations of a typical width proportional to \sqrt{L} . Equation (5.8) is also invariant under translations ($u \rightarrow u$, $x \rightarrow x + x_0$)

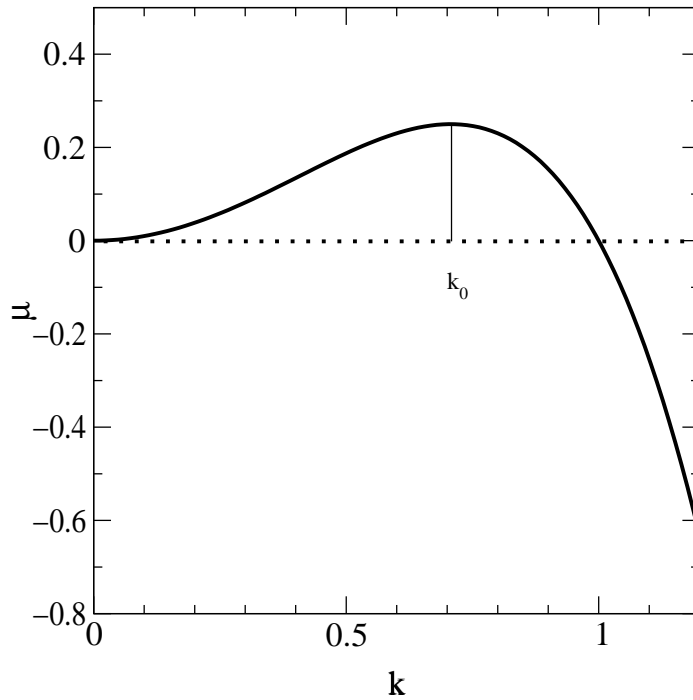


Figure 5.9:

Dispersion relation for the Kuramoto-Sivashinsky equation. The mode corresponding to k_0 is the one with maximum linear growth.

and under a Galilean symmetry . A different reflexion symmetry is valid in this case ($u \rightarrow -u, x \rightarrow -x$).

As an example, we will present what we mean by a Galilean invariance of u ($x \rightarrow x + 2vt, u \rightarrow u + v$). The corresponding change of variables is

$$x' = x + 2vt \quad (5.9)$$

$$t' = t \quad (5.10)$$

$$\bar{u}(x, t) = u(x', t') + v \quad (5.11)$$

We suppose that u is a solution of the KS equation $u_{t'} = -u_{x'x'} - u_{x'x'x'} + 2uu_{x'}$. Differentiation with respect to the primes variables

$$\bar{u}_t = u_{t'} + 2u_{x'}v \quad (5.12)$$

$$-\bar{u}_{xx} - \bar{u}_{xxxx} + 2\bar{u}\bar{u}_x = -u_{x'x'} - u_{x'x'x'} + 2(u+v)u_{x'} \quad (5.13)$$

and letting equal the two equations we arrive again to the KS equation

$$\bar{u}_t = u_{t'} + 2u_{x'}v = -u_{x'x'} - u_{x'x'x'} + 2(u+v)u_{x'} = -\bar{u}_{xx} - \bar{u}_{xxxx} + 2\bar{u}\bar{u}_x \quad (5.14)$$

The corresponding exact Galilean invariance of h is $x \rightarrow x + 2vt, h \rightarrow h + vx + v^2t$

The stability of the laminar solution $h = 0$ [$u = 0$] is analyzed by linearizing Eq. (5.7) [Eq. (5.8)]. For commonly used periodic boundary conditions the growth rate μ for the Fourier mode of wave number k is $\mu = k^2 - k^4$ (Fig 5.9). In two dimensions k^2 is replaced by $|\mathbf{k}|^2$. The laminar solution is unstable for all modes within $0 < k < 1$.

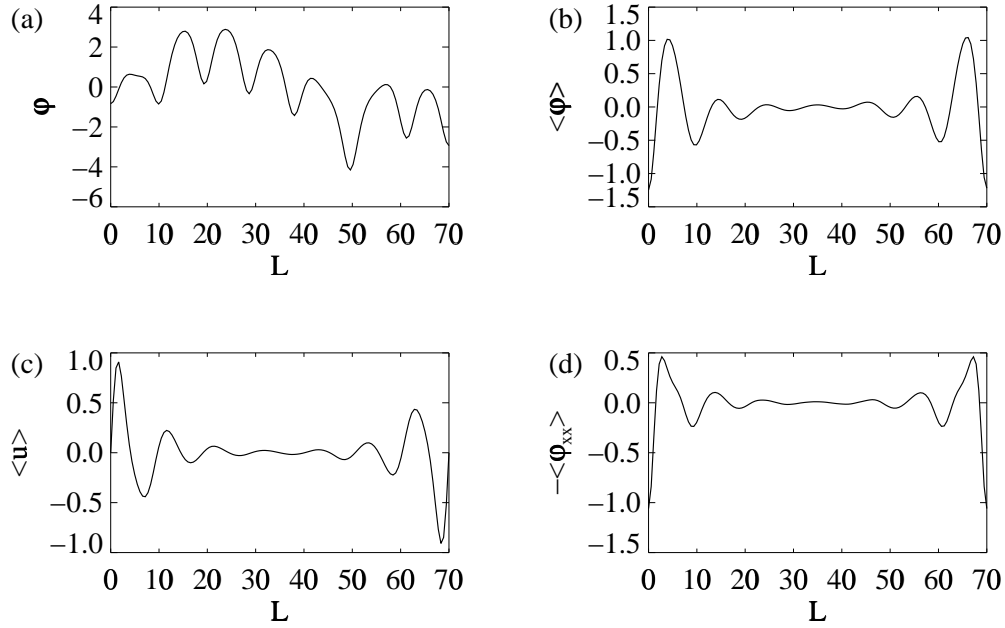


Figure 5.10: Results from simulations of the one-dimensional Kuramoto-Sivashinsky equation with stress-free boundary conditions. System size $L = 70$. a) A characteristic front φ at time $t = 1000$. b) The time average of the front φ , c) of u and d) of $\varphi_{xx} = u_x$.

The fastest growing mode has a wave number $k_0 = 1/\sqrt{2}$ corresponding to a wave length $\lambda_0 = 2\sqrt{2}\pi \approx 8.89$. The wave length λ_0 serves as a basic length scale, and the system size L is naturally measured in units of this scale, L/λ_0 , which is called the *aspect ratio*. Beyond the linear range, the nonlinear term becomes important and produces growth (linear in time) of the mean value of h , while the mean value of u saturates. For L large enough to permit a sufficient number of unstable Fourier modes, the solution exhibits spatio-temporal chaotic behavior that can be associated with a disordered evolution of a cellular pattern.

Many studies have been devoted to the bulk behavior of the Kuramoto-Sivashinsky system [53]. In relation to average patterns however the boundaries are of paramount importance, as discussed above. Here, we consider two types of boundary conditions. One of them is the *rigid boundary conditions*, where

$$u(0, t) = u(L, t) = u_x(0, t) = u_x(L, t) = 0, \quad (5.15)$$

or equivalently,

$$h_x(0, t) = h_x(L, t) = h_{xx}(0, t) = h_{xx}(L, t) = 0. \quad (5.16)$$

Our other choice of boundary conditions is

$$u(0, t) = u(L, t) = u_{xx}(0, t) = u_{xx}(L, t) = 0, \quad (5.17)$$

or equivalently,

$$h_x(0, t) = h_x(L, t) = h_{xxx}(0, t) = h_{xxx}(L, t) = 0 , \quad (5.18)$$

which we call *stress-free boundary conditions*, with reference to similar conditions in hydrodynamics.

We integrate the Kuramoto-Sivashinsky equation using explicit finite-differences of first order in time, second order in space for the linear terms, and fourth order in space for the nonlinear term. The time step is chosen sufficiently small to avoid any spurious behavior. The number of grid points used is 128 in one dimensional simulations and 64×64 in two dimensions. In all cases, the simulations were started from random initial conditions.

5.3.2 Results.

We are interested in the average pattern of u and the average pattern of the front φ of h ,

$$\varphi(x, t) = h(x, t) - \frac{1}{L} \int_0^L h(x, t) dx . \quad (5.19)$$

Due to the linear growth of h , and as we are interested in averages we have to subtract the instantaneous spatial average to follow the growth of h in order to get a good average. This is not needed in the average of u because it does not grow. To optimize the measurements of the average, the sampling was first started well beyond the initial transient behavior. For the system sizes considered, the typical transient time was limited to approximately 20 time units, and we discarded the first 100 time units. Then, averages were taken from configurations sampled every 5 time units. A total of 10,000 configurations per run were included, and further average over 10 runs with independent random initial conditions was performed. This is a large sample, but was necessary to compensate for the slow convergence of the averages produced by the long-range time correlations present in the KS equation.

In both one and two dimensions and with both rigid and stress-free boundary conditions we obtain non-trivial and ordered time-averaged patterns from the spatio-temporally chaotic evolution (Figs. 5.10-5.14), emphasizing that the formation of average patterns in spatio-temporal complex systems is general despite the presence of very large fluctuations. The presence of boundaries breaks the translational symmetry of the equations. The boundary conditions (5.15)-(5.18) respect however its reflection symmetries (for reflexions with respect to the center of the domain). As in the experiments, here we find that the average patterns display these remaining symmetries. In the two-dimensional case the average pattern recovers also the square symmetry of the integration domain (Fig. 5.12). Except for the one-dimensional case with stress-free boundary conditions (Fig. 5.10), an overall parabolic profile of the average front is obtained (see Figs. 5.11-5.13). For the derivative u a mean slope is obtained [126]. This parabolic profile is a peculiarity of the Kuramoto-Sivashinsky equation and we do not expect this shape in other systems. It can be removed by considering the second derivative of the front φ instead of φ itself; for this variable

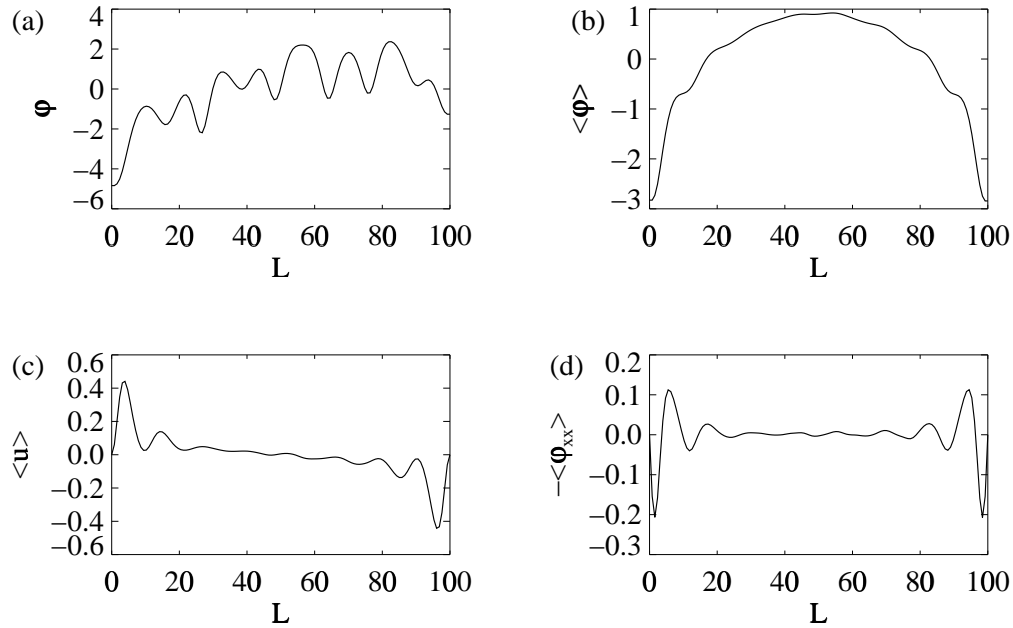


Figure 5.11: The same as Fig. 5.10 but for rigid boundary conditions.

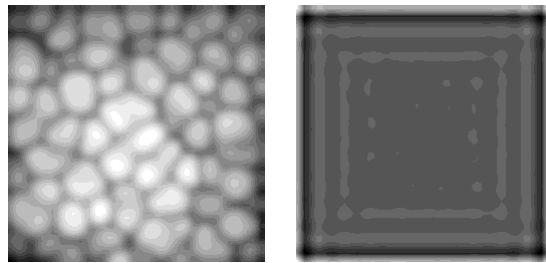


Figure 5.12: Results from simulations of the two-dimensional Kuramoto-Sivashinsky equation with stress-free boundary conditions. System size $L \times L = 70 \times 70$. Left: A characteristic instantaneous image of the front φ ($t = 1000$), different values of φ are coded with different gray levels. Right: The average of $\nabla^2 \varphi$, showing the square symmetry. The average of the Laplacian instead of the front itself is shown to eliminate the dominant parabolic shape of the average, thus improving the visibility of the sidewall oscillations.

(and for the Laplacian in two dimensions) the discussion for all the cases is very similar to the one-dimensional stress-free situation, that we address in further detail in the remaining of the section.

Figure 5.14 shows the average patterns for $L = 60$ and $L = 100$. The number of oscillations increases with the size of the system, although only those close to the boundaries are large. The amplitude of the oscillations decays abruptly when moving

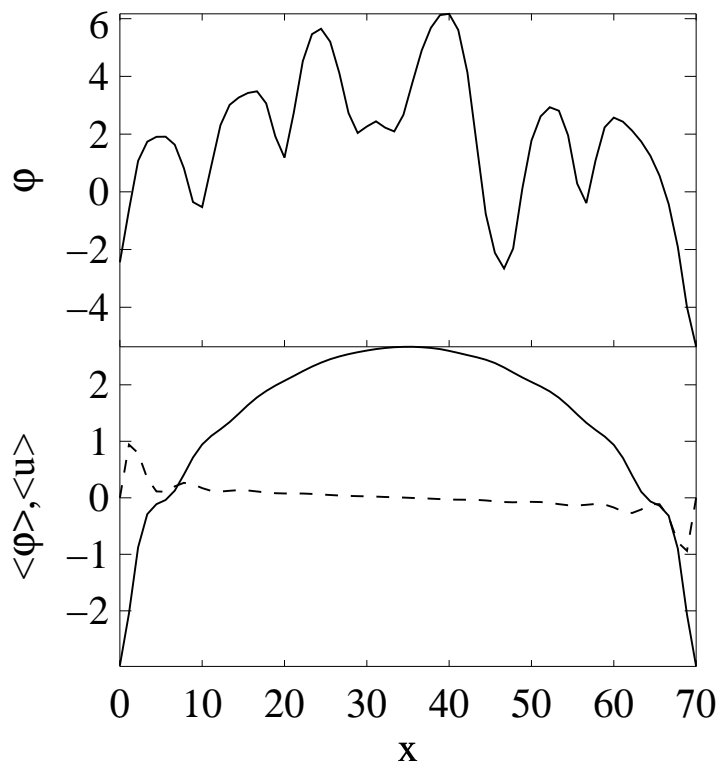


Figure 5.13: a) A central horizontal cut of the configuration shown in the left panel of Fig. 5.12. b) Solid: a central horizontal cut of the time average of the front φ for the same parameter values; dashed: the same cut for the time average of φ_x .

away from the boundaries. Thus for system sizes bigger than $L \approx 100$ the oscillations in the bulk are less evident and more statistics is needed. Furthermore, the distance between consecutive maxima is close (but not equal, see below) to the characteristic length scale $\lambda_0 \approx 8.89$. Similar observations were done in the experiments referred to at the beginning. In Fig. 5.15 the number of local maxima N in the average front is shown for increasing values of the aspect ratio L/λ_0 . N is written in terms of the average distance λ between two consecutive minima, $N = L/\lambda$. The line where $\lambda = \lambda_0$ is also indicated in Fig. 5.15. Plateaus are obtained at every integer N between 6 and 11 for system sizes L between 59 and 112. The average distance λ is consistently larger than λ_0 . Consistent deviations (positive or negative) are also known from the Faraday wave experiments [9].

If only the central region is considered, the plateaus fall off. More specifically, consider the ‘central region’, defined as the domain ranging from the second local minimum to the second last local minimum of φ (see Fig. 5.14). The rest of the the pattern is thus considered the ‘boundary region’. We now determine the average distance λ_c between consecutive minima in the central region for various system sizes L , and find the number of maxima L/λ_c characteristic for the central region. The results are shown in Fig. 5.15. Intriguingly, the plateaus now fall off, an observation also done in experimental studies of the central region [9] (compare for example with

Fig 5.2). At first sight the comparison of the two graphs (Fig. 5.15 and Fig 5.2) seems clear. However a deeper insight can bring us some doubts about the correspondence of the magnitudes plotted. In the Faraday experiment, the frequency of oscillation is varied. The frequency selects the wave number through the dispersion relation, and thus changing the aspect ratio. In the Kuramoto-Sivashinsky the only parameter present in the system is the size of the domain that changes the aspect ratio. So in both cases we are plotting related measures.

In order to explain this ‘fall off’ effect, we determine the average distance λ_b between minima in the boundary regions. Over the entire range of system sizes considered, these distances changes very little, not more than 4%, so that to a first approximation we can consider λ_b independent of L . For the central region we now have

$$\frac{L}{\lambda_c} = (N - 4) \frac{L}{L - 4\lambda_b} \simeq N + 4 \left(\frac{(N - 4)\lambda_b}{L} - 1 \right). \quad (5.20)$$

The last approximation is valid for λ_b/L small. For λ_b constant, it is seen that L/λ_c falls off as $\sim L^{-1}$ within a given plateau characterized by N . Thus an almost constant value of λ_b serves as a generic explanation for the generally observed fall off of the plateaus. The overall picture is that when L is increased the total number of oscillations tends to remain constant, as well as λ_b , so that λ_c increases. This situation continues until the local wave length in the central region is far enough from λ_0 , moment at which a new oscillation is accommodated and a jump in N occurs.

From Fig. 5.14 it is clear that the amplitude $A(x)$ of the average pattern in general decays with increasing distance from the boundaries [127]. Experimental studies show the same behavior [9, 107, 108, 109]. To quantify this observation, we consider the spatial average $\langle A^2 \rangle = L^{-1} \int_0^L A^2 dx$. The variation of $A_{rms} = \sqrt{\langle A^2 \rangle}$ with system size is shown in Fig. 5.16, showing a power-law dependence as $A_{rms} \sim L^{-1/2}$.

We explain this fact by noting that Fig. 5.14 indicates that A_{rms} receives its largest contribution from the boundaries, so that the integral in the definition of $\langle A^2 \rangle$ becomes a constant for system sizes larger than the boundary region. Thus the factor L^{-1} in the definition of $\langle A^2 \rangle$ becomes the dominant L -dependence thus providing the observed behavior of A_{rms} .

5.3.3 Discussion and conclusion.

Our main goal in this work is to show that the phenomenon of time-averaged patterns from spatio-temporal chaos is a universal boundary effect in nonlinear extended dynamical systems, which we exemplify with a study on the Kuramoto-Sivashinsky, equation. Our work shows that a simple model of spatio-temporal chaos reproduces much of the experimentally observed behavior of averaged patterns.

- The symmetry of the average patterns is strongly influenced by the imposed boundary conditions. Compare Fig. 5.10.c and 5.11.c. For the square domain, Fig. 5.12

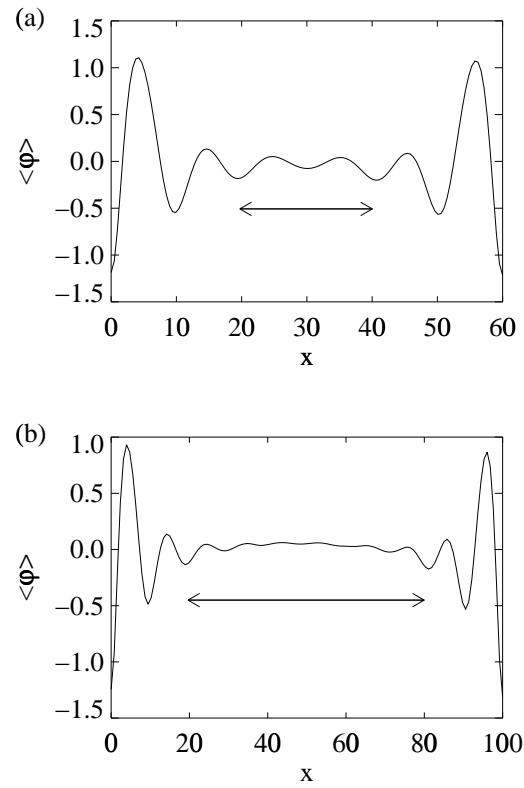


Figure 5.14: Average patterns of the front φ for the one-dimensional Kuramoto-Sivashinsky equation with stress-free boundary conditions. a) $L = 60$. b) $L = 100$. The arrows indicate the 'central region', as defined in the text.

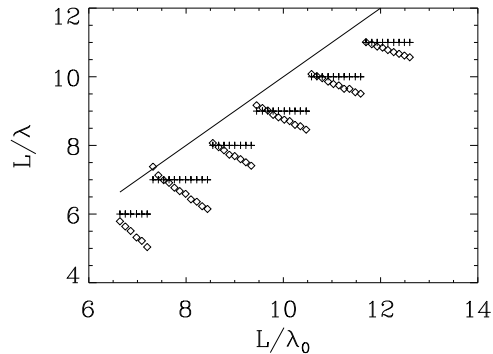


Figure 5.15: +: The number of maxima $N = L/\lambda$ in the average front versus the aspect ratio L/λ_0 , λ being the average distance between consecutive minima in the entire region. \diamond : the number of maxima in the central region, given by L/λ_c . The solid line corresponds to $\lambda = \lambda_0$.

- The system continually fluctuates, but never becomes fully ordered. As can be seen from the several instantaneous images shown.
- The amplitude of the average pattern is a decreasing function of the distance to the boundary and of the system size. Fig. 5.16
- The existence of plateaus in the wave number of the patterns are easily checked against experiments.
- The presence of structured averages in the KS equation² enhances our belief that many of the effects found in this work and in other experiments have a universal character, and that they are not specificities of the systems involved.

One objection that could be raised against our results is that apparently the experimental results present a ‘stronger’ contrast than our numerical results. The ‘strong coherence’ displayed in some experimental pictures is often due to observational artifices used to sharpen the structure of the averages. For example, in the case of Faraday waves experiments, the shadowgraph technique artificially amplifies the contrast of the instantaneous images, enhancing the apparent coherence of the average. However, qualitative aspects of the pattern such as its symmetry are not distorted by the recording technique. We are not claiming that we reproduce every single aspect of the experiments, but the generic features reported in this work, namely the recovery of the global symmetries in the average pattern, the decay of its structure from the

²We have strong evidence that structured average patterns can also be found in the complex Ginzburg-Landau equation, which is another model equation describing spatio-temporal chaos. This appears not only in extended dynamical systems, but also in two-dimensional simulations of molecules interacting via a Lennard-Jones potential. See for example Figs. (1.5) and (1.6).

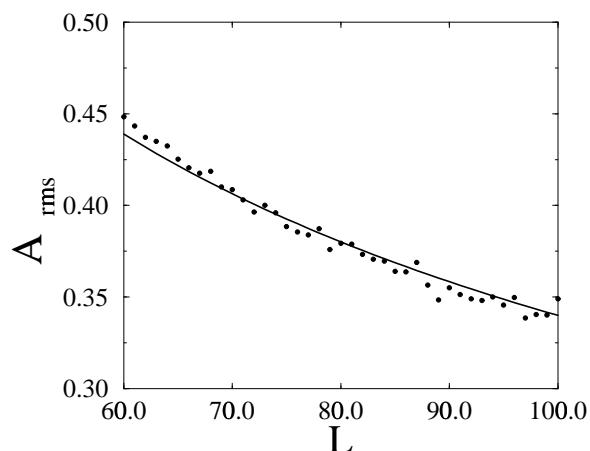


Figure 5.16: Variation of the root mean square amplitude A_{rms} over the range of system sizes $59 < L < 107$. The solid curve is the function C/\sqrt{L} , with C fitted to the data

boundaries to the bulk, as well as the wave number plateaus, squarely match the experimental behavior of many different systems.

One possible picture that could, in principle, explain both the coherence of the averages near the boundary and the decay towards the bulk, is the following: the patterns should be dominated by the structure of the linear modes within the instability band, and coherence at the boundaries should be expected from the necessary locking of the modes to satisfy boundary conditions. This picture is probably part of the truth, but we note that it is not a complete explanation since it misses a fundamental fact: within the instability band there are some linear modes that carry the global symmetries of the nonlinear system and some that do not. It is obvious by simple observation that the non-symmetric modes are present in the instantaneous configurations, and therefore, this simple picture does not explain the symmetry properties of the average. A good experimental example is given in Fig 5.8. The instantaneous rolls are all perpendicular to the boundary. However, the average is formed by rolls of circular symmetry being parallel to the boundary.

We could also wonder whether a simple stochastic model can reproduce some of the results, for example a model of the form $dp/dt = L \cdot p + noise$. A very simple analytical calculation shows that the time average of the field satisfying the equation proposed for zero-mean noise does not give any structured average pattern: Take any linear model of the form previously proposed, average it to obtain $d \langle p \rangle / dt = L \cdot \langle p \rangle + 0$. If L has a stable spectrum the average decays to zero, otherwise, the average explodes.

In conclusion, we have established the formation of ordered time-averaged patterns in the Kuramoto-Sivashinsky equation, in one and two dimensions, and with rigid as well as stress-free boundary conditions. The average pattern recovers the symmetries which are respected by both the equation and the boundary conditions. The am-

plitude is strongest at the boundaries and decays with increasing distance to them. The law of decay has been found and explained. We have determined the selected wave length λ , its variation with system size L , and interpreted the different behavior between the central and boundary regions. Most of these observations are also found in experimental systems for which the Kuramoto-Sivashinsky equation does not apply, thus indicating its generic, mainly geometrical, origin: What is relevant for these phenomena to occur is the occurrence of strong enough chaotic fluctuations in the presence of non-trivial boundaries.

Chapter 6

Boundary Effects in The Complex Ginzburg-Landau Equation

The effect of a finite geometry on the two-dimensional complex Ginzburg-Landau equation is addressed. Boundary effects induce the formation of novel states. For example target like-solutions appear as robust solutions under Dirichlet boundary conditions. Synchronization of plane waves emitted by boundaries, entrainment by corner emission, and anchoring of defects by shock lines are also reported.¹

¹This Chapter corresponds to *Boundary Effects in The Complex Ginzburg-Landau Equation*, by V.M. Eguíluz, E. Hernández-García and O. Piro, to appear in *Int. J. Bifurcation and Chaos* (1999).

6.1 Introduction

The complex Ginzburg-Landau equation (CGL) is the generic model describing the slow phase and amplitude modulations of a spatially distributed assembly of coupled oscillators near its Hopf bifurcation [128]. It contains much of the typical behavior observed in spatially-extended nonlinear systems whenever oscillations and waves are present. After proper scaling it can be written as:

$$\partial_t A = A - (1 + i\beta)|A|^2 A + (1 + i\alpha)\nabla^2 A \quad (6.1)$$

where A is a complex field describing the modulations of the oscillator field, and α and β are two real control parameters. The first two terms in the r.h.s. of Eq. (6.1) describe the local dynamics of the oscillators: the first one is a linear instability mechanism leading to oscillations, and the second produces nonlinear amplitude saturation and frequency renormalization. The last term is the spatial coupling which accounts both for diffusion and dispersion of the oscillatory motion.

The power of our analytical tools to study non-linear partial differential equations in general, and the CGL equation in particular, is very limited. Roughly speaking, only relatively simple solutions satisfying simple boundary conditions, usually in infinite domains, are amenable to analysis. Examples of these are plane and spiral waves. Nevertheless, sustained spatiotemporally disordered regimes have been found and thoroughly investigated numerically. Detailed phase diagrams displaying the transitions between different regimes have been charted for the cases of one and two spatial dimensions [129, 130, 131]. However, we want to stress that most of these numerical studies have been performed only under periodic boundary conditions, with the underlying idea that in the limit of very large systems the boundary conditions would not influence the overall dynamics. As a consequence of this belief, and despite its importance for the description of real systems, a systematic study of less trivial boundary conditions has been largely postponed. This is the case not only for the CGL equation but also for other nonlinear extended dynamical systems, and only few aspects of this problem have been collaterally addressed so far [132, 133, 134]. The purpose of this paper is to report on the initial steps of a program aiming towards such a systematic study. We will focus here on the behavior of the two-dimensional CGL equation on domains of different shapes and with different types of boundary conditions (Dirichlet or Neumann for example).

For the purpose of comparison we first summarize the behavior observed numerically on two-dimensional rectangular domains under the commonly used periodic boundary conditions. Let us remind that in the so called *Benjamin-Feir* (BF) *stable* region of the parameter space defined by $1 + \alpha\beta > 0$, there is always a plane wave solution of arbitrarily large wavelength that is linearly stable. In particular, for parameters in that region, and initializing the system with a homogenous condition (a wave of wavenumber $k = 0$) it will remain oscillating homogeneously. If we now vary the parameters slowly towards crossing the BF line, all the plane waves lose stability and small perturbations bring the system to a spatiotemporally disordered cellular state (the so-called *phase turbulence*). It is known that the behavior close to the BF line can be approximated by the Kuramoto-Sivashinsky equation.

Further change of the parameters to go deeper inside the BF unstable region eventually leads to generation of defects, i.e., points where $A = 0$, and a kind of turbulent evolution characterized by the presence of these defects sets in. This is the so called *defect* or *amplitude turbulence*. If we now trace back to the initial parameter values from the state dominated by defects, the system does not recover the initial uniformly oscillatory state. Spontaneous generation of defects ceases at parameter values still inside the BF unstable region. At these parameter values, the system usually reaches a state consisting of a spiral wave whose core is a defect. This spiral occupies most of the domain and it is limited by the shock-lines where the arms of the spiral meet themselves. Defects without spiral arms appear at the crossings of such shock-lines. In this regime, the amplitude of the field is time independent and its phase evolves quite regularly in time. In general, the configurations that share these two properties are called *frozen states*. These states persist while we vary the parameters all the way back to the BF stable region. Starting at values corresponding to a defect-dominated evolution, and suddenly setting the parameters to values in the stable BF regime, the stationary solution will be also a frozen state but in this case several domains, each one containing a spiral wave, may form. The size of these domains vary with the initial conditions, but the typical scale is controlled by the parameters. Shock lines where the arms of different spirals collide now proliferate and non-spiral defects are usually present at the crossings between them.

6.2 Boundary effects

Let us consider first parameter values such that with periodic boundary conditions the long-time asymptotic states are *frozen* and look at how the behavior is modified by changing the boundary conditions. We apply null Dirichlet ($A = 0$), and Neumann (vanishing of the normal derivative of A) boundary conditions. For the former, we consider three different boundary shapes: square, circle, and stadium-shaped domains. Comparison between square and circle will allow us to investigate the influence of corners. On the other hand, our interest in the stadium arose from considerations of ray chaos, but it will be presented here as a combination of circle and square geometries.

In the Dirichlet case, the zero amplitude boundaries facilitates the formation of defects near the walls. Starting from random initial conditions, defects are actively created in the early stages of the evolution. After some time however all the points on the boundaries synchronize and oscillate in phase so that plane waves are emitted. Defect formation ceases, and the waves emitted by the walls push the remaining defects towards the central region of the domain. There the defects annihilate in pairs of opposite charge and as a result of this process a bound state is formed by the surviving set of equal-charge defects. The orientation of the waves emitted by the boundaries also changes during the evolution. The synchronized emission of the early stages proceeds, obviously, perpendicular to the boundary but later the wavevector tilts to some emission angle of approximately 45 degrees. This angle depends on both the parameter values and the geometry of the boundaries. The fact that this angle

is not exactly 45 degrees is made evident by a mismatch of the waves coming from orthogonal walls. Finally the system reaches a frozen state of the type displayed in Fig. (6.1). The defects are confined in the center of the domain forming a rigid static chain. The constant-phase lines travel from the boundaries towards the center of the domain. Shock lines appear where waves from different sides of the contour collide. The strongest shocks are attached perpendicularly to the walls. If for a particular initial condition all defects annihilate the asymptotic state is a defect-free *target* solution. This kind of solutions is not seen in simulations with periodic boundary conditions.

It is known [135] that the phase velocity of the usual spiral waves in infinite systems could point either inwards or outwards the defect core depending on the parameter values. In our simulations in the square geometry with Dirichlet conditions, however, the direction of the phase velocity is always from the boundary to the core. We can understand this better by applying null Dirichlet conditions to only one of the walls. The synchronized emission that we observe is a straightforward generalization to two-dimensions of the one-dimensional Nozaki-Bekki emitting hole solution [136]. We have verified [137], for instance, that the direction of the emitted waves (inwards or outwards) can be changed with parameters as predicted by the analytic computations [135]. However, when several of the walls are lines of zeros (the four sides of the square, for example) the direction of the phase velocity becomes determined by the angle between these lines. In other words, corners effectively entrain the whole system.

In a circular domain (Fig. (6.2)), the frozen structures are either targets (no defects) or a single central defect. Groups of defects of the same charge can also form bound states, but instead of freezing they rotate together. This contrasts with the behavior of the square domains and is correlated with the absence of shock lines linking the boundaries to the center in the case of the circular domains. These links are probably responsible for providing rigidity to the stationary configuration in the square case. Tiny shock lines associated to small departures from circularity in the lines of constant phase can be observed also in the circle but these lines end in the bulk of the region before reaching the boundaries. On the other hand, the constant-phase lines reach the boundaries nearly tangentially in contrast to what we observe in the square. In addition, we observe that for circular domains the phase velocity direction can be changed controlling the parameters. This is probably a consequence of the absence of the corners that synchronize the emission from the boundaries in the square case.

The stadium shape (Fig. (6.2)) mixes features of the two geometries previously studied: it has both straight and circular borders. In this case, the curves of constant phase arrange themselves to combine the two behaviors described above. On one hand the lines meet the straight portions of the border of the stadium with some characteristic angle, as it happens in square domains. However, these lines bend to become nearly tangent to the semicircles in the places where they meet with these portions of the boundaries. A typical frozen solution displays a shock line connecting the centers of the circular portions of the domain. This shock line usually contains defects. It is also possible to find defect-free target solutions as in the case of the circle, and the behavior of the phase velocity is also similar in the sense that its

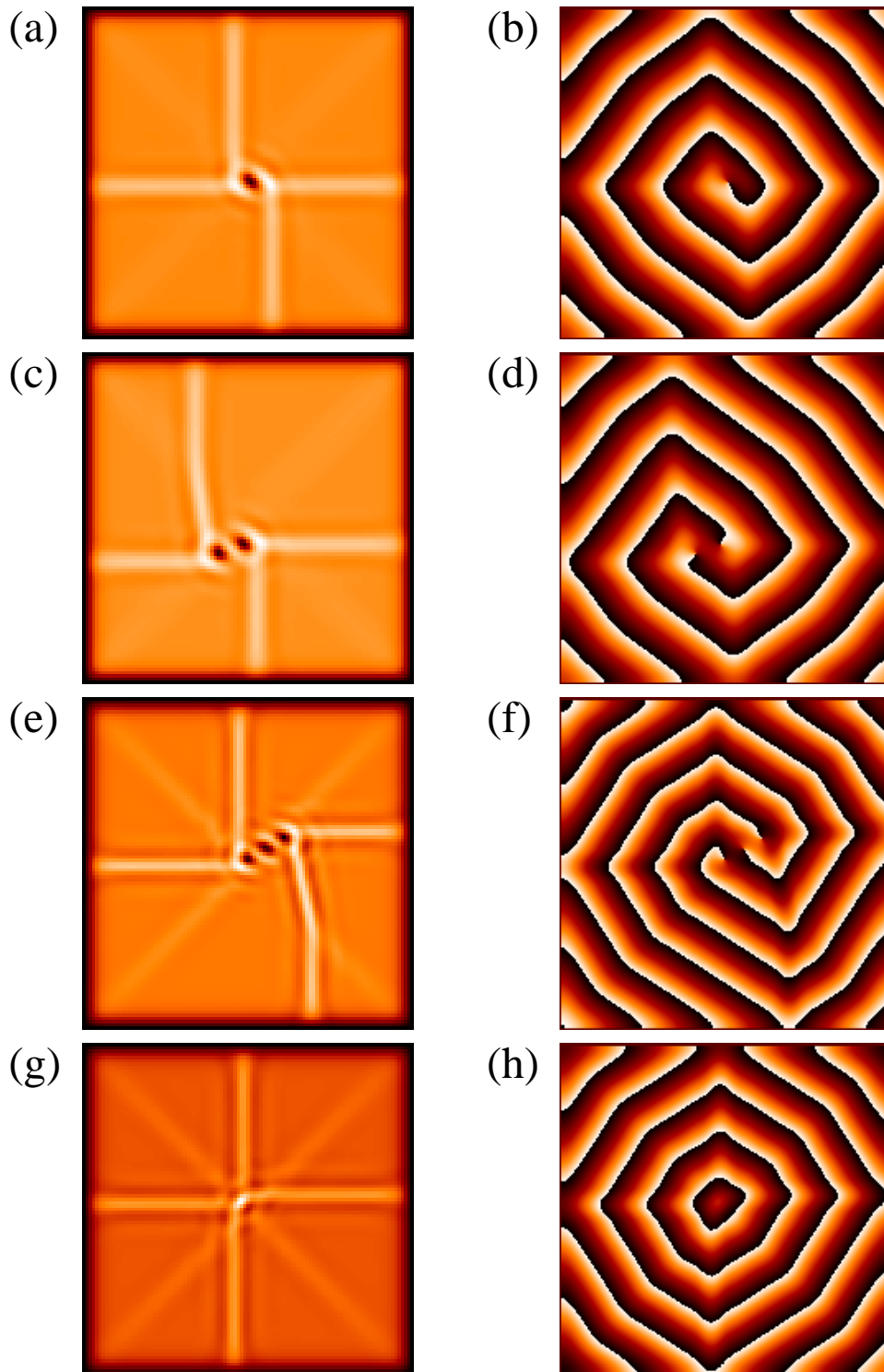


Figure 6.1: Frozen structures under null Dirichlet boundary conditions in a square of size 100×100 . Parameter values are $\alpha = 2, \beta = -0.2$ (a-d), and $\alpha = 2, \beta = -0.6$ (e-h). Snapshots of the modulus $|A|$ of the field are shown in the left column and snapshots of the phase in the right column. Color scale runs from black (minimum) to white (maximum).

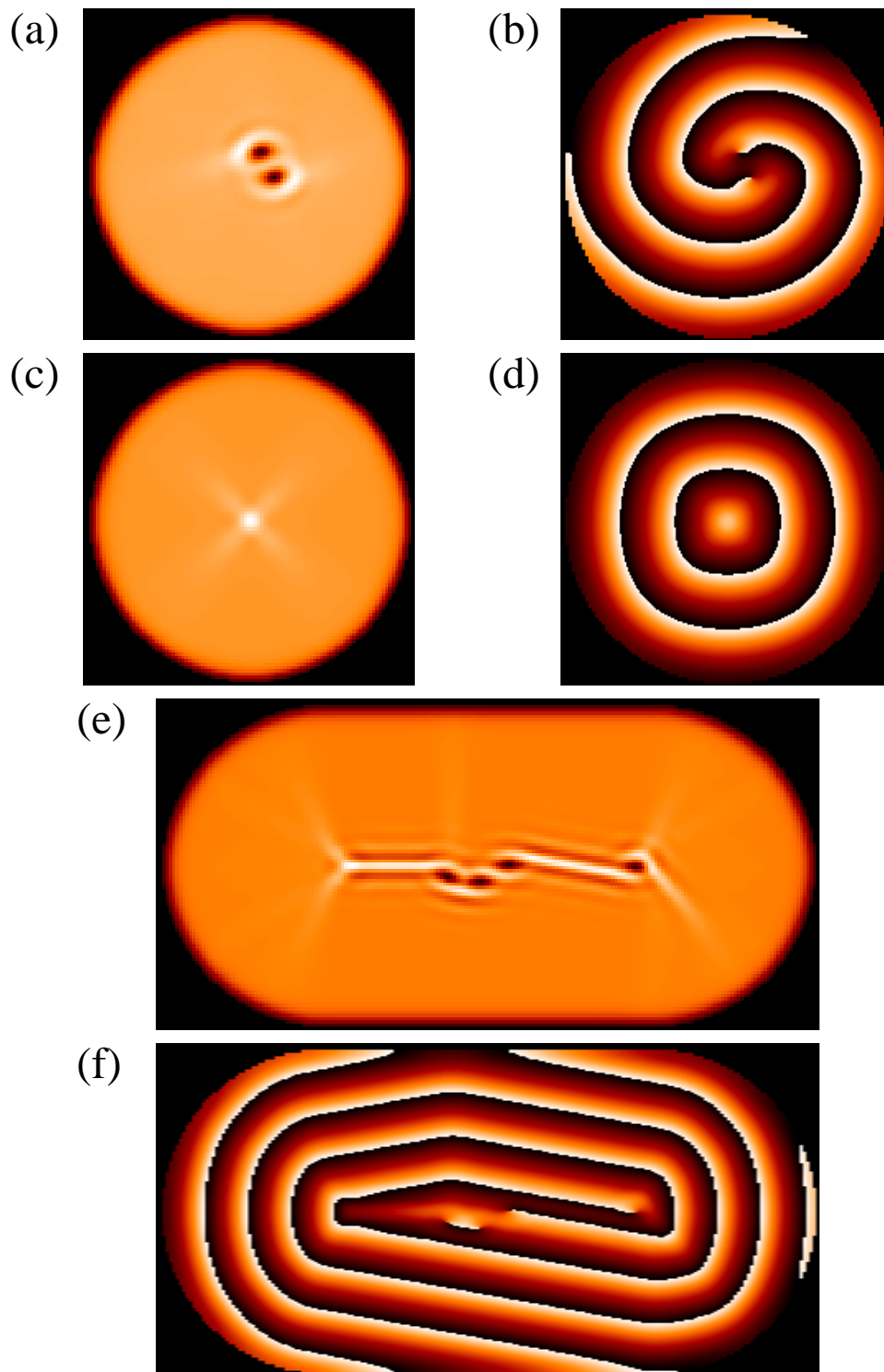


Figure 6.2: Frozen structures under null Dirichlet boundary conditions in a circle (a-d) of diameter 100 for parameter values $\alpha = 2$, $\beta = -0.2$, and in a stadium (e-f) of size 200×100 , for parameter values $\alpha = 2$, $\beta = -0.6$. Snapshots of the modulus $|A|$ are shown in the left column and (e) whereas the phase is shown in the right column and (f). Color scale as in Fig. (6.1).

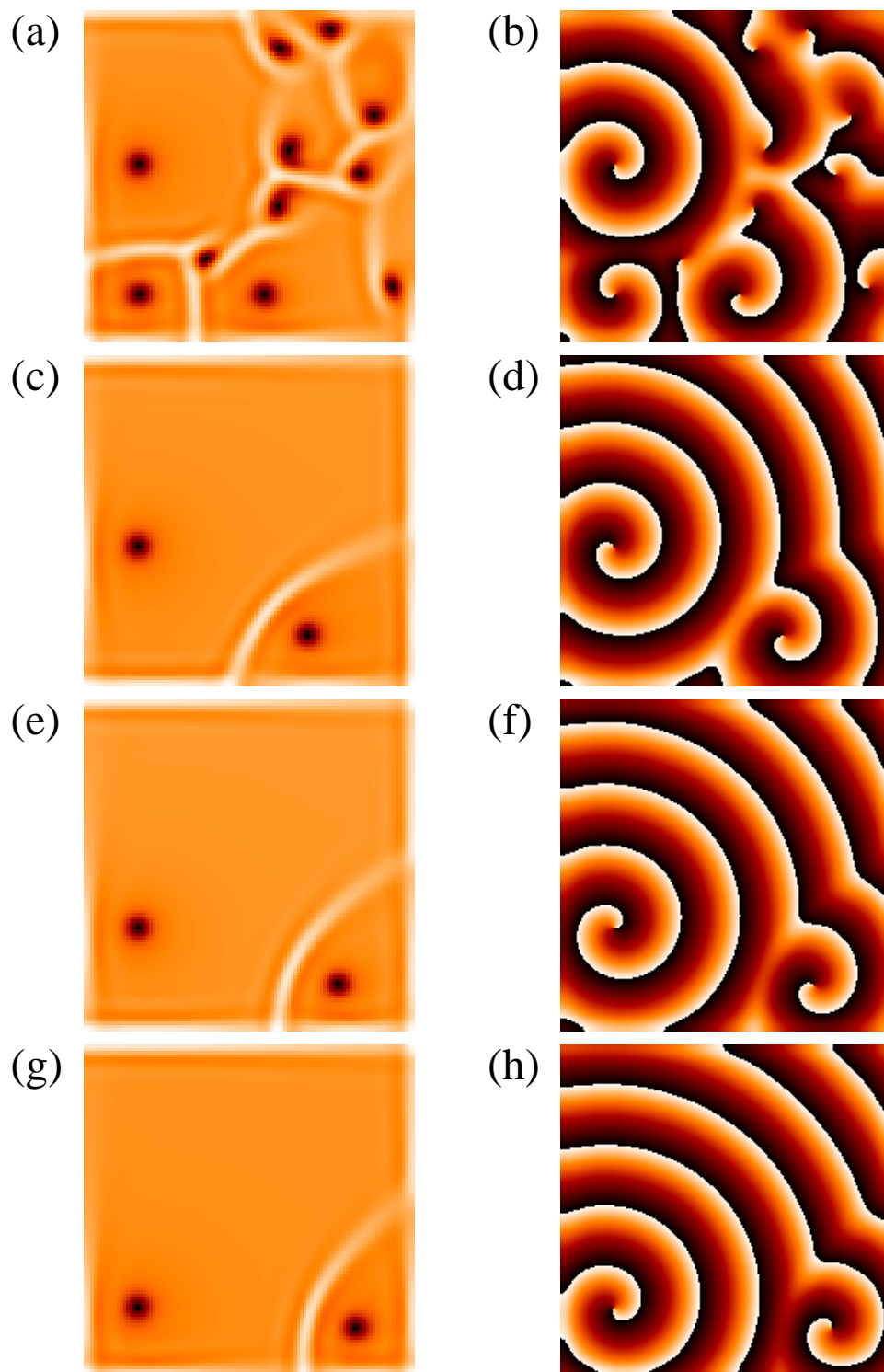


Figure 6.3: Snapshots of the field $|A|$ (left column) and phase (right column) in color scale as in Fig. (6.1) at times $t = 2.5 \times 10^4$ (a-b), $t = 5. \times 10^4$ (c-d), $t = 7.5 \times 10^4$ (e-f), and $t = 10. \times 10^4$ (g-h) under Neumann boundary conditions in a square domain of size 100×100 . Parameter values are $\alpha = 2$, $\beta = -0.2$.

direction can be changed by modifying the parameters.

The behavior under Neumann boundary conditions is rather similar to the case of periodic boundary conditions. However, the Neumann conditions induce several subtle features to the dynamics. For example, shock lines are now forced to reach orthogonally the boundaries. In addition, defects can be irreversibly absorbed by the boundaries, a process that is obviously impossible with periodic boundary conditions. During the evolution a spiral defect behaves as if it were interacting with a mirror image of itself with opposite charge located outside the domain [138]. This reflects in few characteristic phenomena. On one hand an isolated defect tends to move parallel to a nearby Neumann wall. On the other hand, mutual annihilation of a defect and its image is also possible accounting for the absorption of this defect by the boundary. Finally, when a defect closely approaches a corner, its evolution possibly as a result of the mutual interaction with two different images. Fig. (6.3) displays a typical evolution of the pattern. Initially starting at random, a number of dynamically active spiral defects is created. These move around eventually annihilating mutually or sometimes being absorbed by the walls while the dynamics progressively slows down. Normally one large spiral wave grows until it fills the whole domain at the expense of the smaller ones that are pushed out of the boundaries.

Finally, we have studied the changes induced by the boundaries for parameter values such that active spatiotemporal chaos (i.e., non-frozen states) is found for periodic boundary conditions. Far from the boundaries spatiotemporally chaotic solutions behave similarly to those satisfying periodic boundary conditions. However, a boundary layer with different behavior shows up near the borders. In Fig. (6.4) we can see plane waves emitted by the boundaries and rapidly fading inside the domain where spatiotemporal chaos evolves. In small domains the boundaries could synchronize the whole system. However, as the system size increases, full synchronization ceases.

For other parameter values, Dirichlet boundary conditions lead eventually to a dynamics characterized by the coexistence of regions dominated by defect turbulence and regions dominated by plane waves (constant $|A|$) whose shape and position normally evolve in time. We have found this behavior in all the domain shapes studied except for circular case.

For these parameter values, Neumann boundary conditions do not produce a dynamics sensibly different than the one induced by periodic boundary conditions. The only noticeable difference is that in the Neumann case the shock lines are forced, as pointed out before, to meet orthogonally the boundaries.

6.3 Conclusions

In this paper, we have presented important features of the dynamics of the CGL equation which depend strongly on the type of boundary conditions imposed, as well as on the geometrical shape of the boundaries.

Dirichlet boundary conditions play a double rôle. On one hand, the walls naturally behave as sources (or sinks) of defects. On the other hand, a wall with null Dirichlet

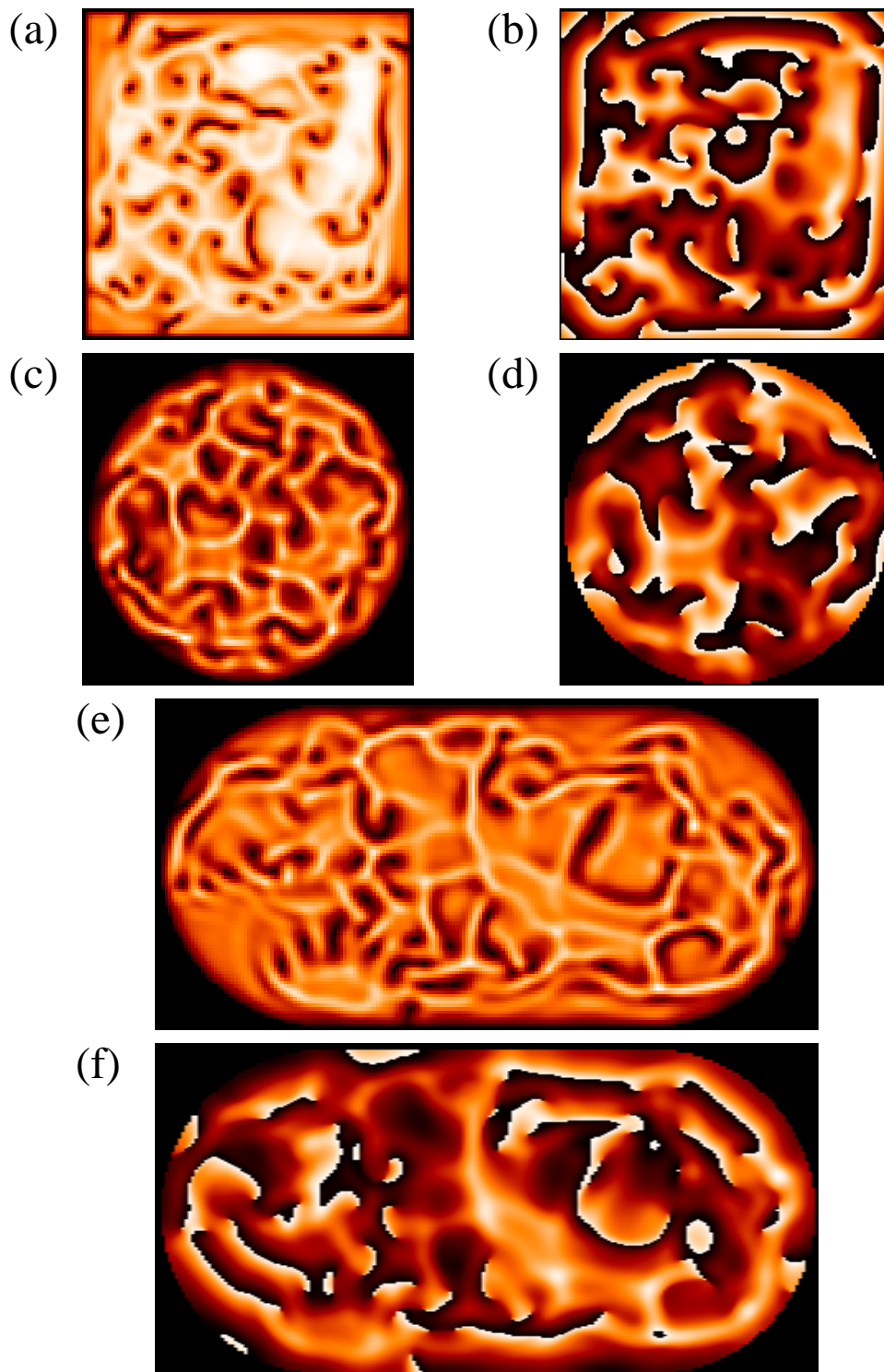


Figure 6.4: Dynamical solutions under Dirichlet boundary conditions. Snapshots of the field $|A|$ are shown in the left column and (e) whereas the phase is shown in the right column and (f). (a-b): square, parameter values $\alpha = 0, \beta = 1.8$; (c-d): circle, parameter values $\alpha = 2, \beta = -1$; (e-f): stadium, parameter values $\alpha = 2, \beta = -0.75$. System sizes and color scale as in Figs. (6.1) and (6.2).

conditions shows a tendency to emit plane waves. The interplay between these two properties of the boundaries gives rise to interesting behavior.

In the case of frozen states, the character of the walls as wave emitters dominates. Some geometrical features of the boundaries have a strong influence on the details of the phase synchronization. Corners, for instance, tend to act as pacemakers. In circular domains, on the other hand, the emission is definitively dominated by the internal spirals. Correspondingly, the internal structure of the frozen states is also influenced by the shape of the boundaries. In a square, defects form a chain which is anchored to the boundaries by a set of shock lines; in a circle, on the contrary, the asymptotic state is usually a bound state disconnected from the boundaries.

Neumann boundary conditions seem to have a much weaker influence on the overall dynamical behavior of the CGL equation. However some differences are evident: One is the orientation of the shock lines, perpendicular to the boundaries. The other is that defects can be ejected through the boundaries, thus favoring states dominated by a single spiral in situations where under periodic boundary conditions a *glassy* state with several spiral domains would be formed.

Since the CGL equation appears naturally in a variety of contexts, we believe that the phenomena found in our preliminary explorations are likely to be relevant in many theoretical and experimental situations. Some of the phenomena reported here have intrinsic interest and deserve further analysis.

Chapter 7

Self-organized evolution in financial systems.

One of the universal characteristics that evidence the analysis of financial-price data is a scale-free distribution of intra-day returns. Different models have been proposed to explain these characteristics and can be divided in two different groups: physically motivated models based on the interaction of a large number of units, and models based on multi-agent interactions. Here we propose a simple financial market model which includes the dispersal of information and formation of opinion clusters, as a fundamental ingredient to account for scale-free returns. Each cluster is assumed to act asynchronously with the same collective action of buying or selling, after which the opinion becomes irrelevant and disappears. The only parameter of the model is the ratio of trading activity vs. information dispersal a . For sufficiently low a the system organizes in clusters of all sizes (bounded by system size) and displays power-law distribution of returns for all the possible range. However for a sufficiently high, the activity is sufficient to inhibit large fluctuations, turning the returns distribution with fat-tails and asymptotic exponential cutoffs¹.

¹This Chapter corresponds to *Self-organized evolution in financial systems*, by V.M. Eguíluz, M.G. Zimmermann, submitted for publication (1999).

7.1 Introduction.

Financial stock market prices have been found to exhibit some universal characteristics similar to those observed in physical systems with large number of interacting units [139, 140]. One of such features is the fat-tail distribution of the logarithmic changes of the market price, the so-called *returns*. Empirical evidence points that the excess kurtosis should be of order 1-100, substantially different from the normal distribution which would give zero. Also for most assets it has been reported that the distribution have exponential tails [140].

Several models have been put forward which phenomenologically shows the fat-tail distributions. Among the more sophisticated approaches are dynamic multi-agent models [141, 142] based on the interaction of two distinct agents populations, (“noisy” and “fundamentalists” traders) which reproduces the desired distributions, but fails to account for the origin of the universal behavior. On the other hand it has been suggested that *herding behavior* may be sufficient to induce the desired distributions [143, 144]. This behaviour takes place when a group of traders coordinate their actions. This approach has been recently formalized by Cont & Bouchaud [145], as a static bond-percolation model. In their original formulation, bonds are initially randomly distributed in a network of agents, so that on average each agent has c bonds. Next, agents are able to buy/sell or wait and those in a connected component of the network are assumed to act likewise (herding). Assuming a simple rule between the trading volume (size of the cluster) and the price change, they show that power-law distribution in the price returns arise at a critical density $c^* = 1$, known as percolation threshold. For $c < 1$ the distributions shows instead an exponential cut-off. In this approach c is an external fixed parameter with a difficult economic justification. Also, and more important, why the market would choose the critical or a nearby value, is a point which deserves further study.

In this work we extend the model of Cont & Bouchaud proposing to focus onto the underlying information network the agents may be handling, as a possible foundation to account for the herding behavior. Our main assumption relies on how rumors are born, transmitted, or vanishes among a single population of agents. As a first approach to model this complicated social behavior we consider: (i) a random dispersal of a either a “buy!” or a “sell!” rumor, which guides and coordinates the agents actions between those who share the *same* information, and (ii) rumors die after they have been used. Finally we assume that the agents are completely governed by the information they posses, and cannot do otherwise. With these very simple ingredients we find that the distribution of the number of agents sharing the same information behaves as a power-law, when the trading activity is small against the rumor dispersal. Using a simple rule for the price change in terms of the order size (proportional to the cluster size) the price returns also exhibit the universal feature. On the other hand when the dispersal becomes faster a smooth transition to truncated exponential tails is observed. However a large portion of the distribution remains on the power-law.

In our approach rumors drive the connectivity of the network in a dynamic way, and the desired distributions are observed even when the time-average density $c(t)$ is far from the critical threshold. In Section 2 we present the model, while on Section 3

we present the numerical simulations. Finally in Section 4 we discuss our results and open perspectives.

7.2 Evolution of agent's information network.

Lets consider that the agent's trading actions are completely governed by the underlying information network they perceive. This accounts for the agent's bounded rationality, as he does not have perfect information: only part of the network will be available to him at any time. Lets assume that agents are allowed to *disperse* information. This can be in a form of rumor on the to-be-announced firms quarter results, on the suspicion of a mayor devaluation in an developing country, and even an agent's simple opinion on a particular stock shared with his personal contacts, which would result in a "buy!" or a "sell!" order to that agent. Mayor broadcasted news are excluded here, because they will influence all traders more or less equally. Therefore we are interested only in the dispersal of certain concealed information, which will be represented by a (bidirectional) *link* between the intervening agents. All agents who share the same information are connected in the information network, and constitute an information *cluster* or group of opinion. This can be easily accommodated in a random network, where agents are the nodes and the links the connections among them.

The other important dynamical process we introduce is the *aging of rumors*. Due to the random dispersal of information in the network, clusters grow and increase their connectivity until the information contained in the group is contrasted: the rumor "expires". The actual quarterly results are publicly announced, the devaluation in the developing country is decided, or your opinion is evaluated against facts. In all of these cases it is safe to assume that all the links corresponding to that rumor should disappear, inducing in turn the same action (buy! or sell!) to all traders in the cluster (recall we are assuming that the agent actions are completely determined by the information network).

A more detailed account could include for example an external source of information, where agents in the same cluster are constantly checking. Whenever the source clearly validates the rumor, all agents will drop almost instantaneously their links and perform the action. Another possible mechanism at an individual level, involves imitation. In this case agents are constantly and expectantly evaluating the concealed information they posses, in order to determine if its true or false. This tense situation will translate in an imitation process: whenever an individual agent drops his links (because he was impatient or he validated the rumor as above), all its neighbors will do likewise, propagating through the whole cluster. This will also be assumed to be very fast due to their expectant behaviour, resulting once again in the total annihilation of that information cluster together with the coordinated market action.

In this way the herding behaviour will be explicitly exhibited due to the underlying information network. The triggering might be an external source or the agent's own impatience. For simplicity, we only consider in the follows an *instantaneous*

disappearance of the links.

7.3 The model.

Initially the random network of N agents has no links, i.e. no information content. We use an asynchronous update of the network, selecting at each time step a random agent, which may exclusively make one of two possible actions: decides the rumor is true with probability a , or disperse information with probabilities $1 - a$. In the former case, the rumor expires by instantaneously dropping all the cluster links, and triggers all members of the cluster to put a market order for one stock. The latter case is done by selecting randomly another agent from the whole network and establishing a new link. If both agents had previously no links, a new rumor is born (randomly buy! or sell!). If one of the agents had no link, then it will join the opinion of the other agents cluster. If both agents already belonged to different clusters, merging of the clusters occurs. At this stage we do not take into account opinion conflicts: just one opinion in the new bigger cluster prevails.

When a buy or a sell order are to be executed, they are assumed to be posted to an external centralized market-maker, which actually performs the operations and sets the new price. Note that as all agents in the cluster act simultaneously, the size of the order is the cluster size. We use the following rule $P(t + 1) = P(t) \exp(s/\lambda)$ to update the price. s is the size of the agent's cluster, and λ is a measure of the liquidity of the market which controls the influence on the price changes due to the order size [146]. With this simple rule, the price returns $R(t) = \ln(P(t)) - \ln(P(t-1))$ is proportional to the order size. So how the distribution of sizes is affected by a is of fundamental importance for the observed returns distribution. Other nonlinear suggestions exist for the price update [147], which will modify slightly the exponents below. However we stress that power-law features observed in this model persist with this modification.

7.4 Price dynamics.

In our presentation the time unit corresponds on average to the addition of a new link or information unit to the network per iteration. Therefore $1/a$ controls the rate of rumor dispersal vs. trading activity, and appears as the only adjustable parameter of the model. For $a = 1$ only trading activity takes place. Starting with some randomly dispersed links, the evolution will asymptotically approach that of single agents trading in the market, and no herding behaviour. On the other hand, for small a , dispersal of information occurs on most of the time steps, increasing the internal connectivity. Intuitively in this limit the network will evolve in a cascade of phenomena. Initially the empty network has time to build many clusters, then eventually merge them into even bigger clusters, and finally it will be dominated by a single big cluster. When an order arrives, an agent of this super-cluster will surely be chosen, inducing a large impact on the market. Although an extreme scenario, we

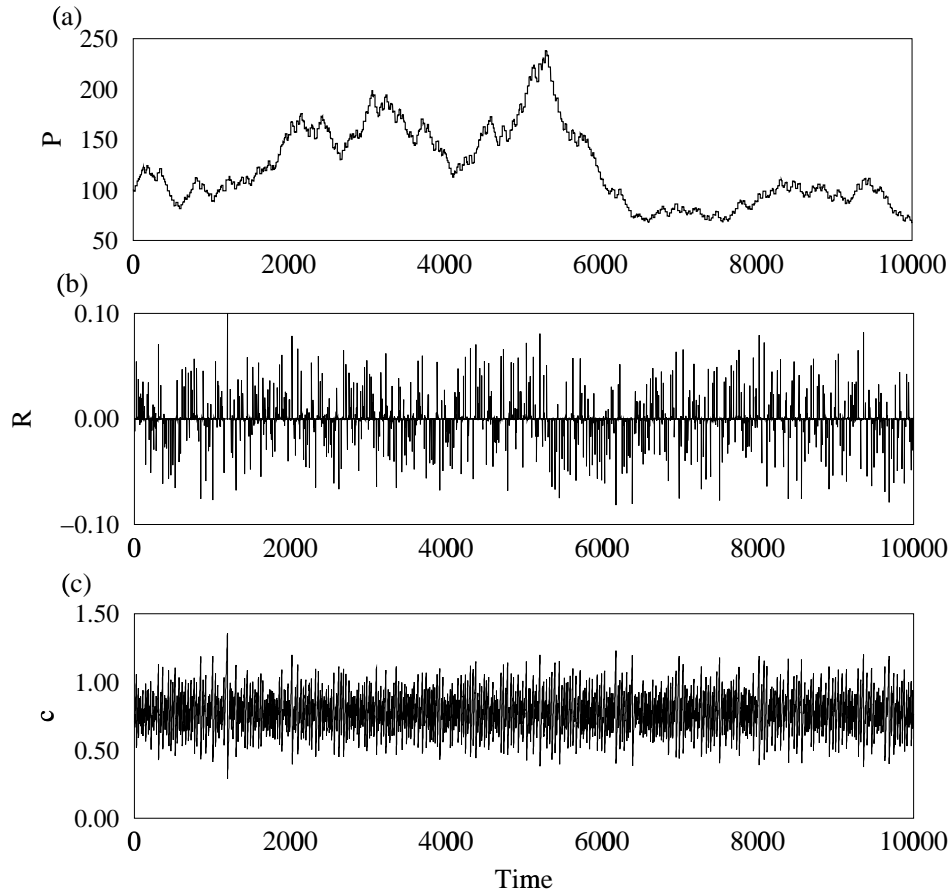


Figure 7.1: (a) Time series of the typical evolution of the market price $P(t)$, (b) the returns corresponding $R(t) = \ln P(t) - \ln P(t-1)$, and (c) the connectivity $c(t)$. The mean value of the connectivity is $\langle c \rangle = 0.78$ and the standard deviation $\sigma = 0.14$. Number of agents $N = 10^4$, herding parameter $a = 0.01$.

can estimate that this should occur when $a \ll O(1/N)$. From the above discussion we would like to label parameter a as the “herding parameter”: for $a = 1$ no herding occurs, while for $a < 1$ herding is observed.

To obtain more quantitative results for intermediate values of a , we have performed numerical simulations for a population of $N = 10^4$ agents. In Fig. (7.1a), we show a typical evolution of the market price $P(t)$ following our model. The value of the herding parameter $a = 0.01$, corresponds in average to a buy or sell order every 100 iterations, or in other words the rumors propagation velocity is 99 links per order. The corresponding returns $R(t)$ are shown in Fig. (7.1b). The evolution of the connectivity $c(t)$ (average number of links per agent) is shown in Fig. (7.1c), with a corresponding time average $\langle c \rangle = 0.75$ and some fluctuations overshooting the critical value $c^* = 1$.

In Fig. (7.2) we show the distribution of returns for three different herding parameters $a = 0.30$, 0.10 and 0.01 . Power laws $\text{prob}(R) \approx R^{-\alpha}$ are fitted to the well averaged region, with the exponent varying from 1.5 to 1.6. Note that in all

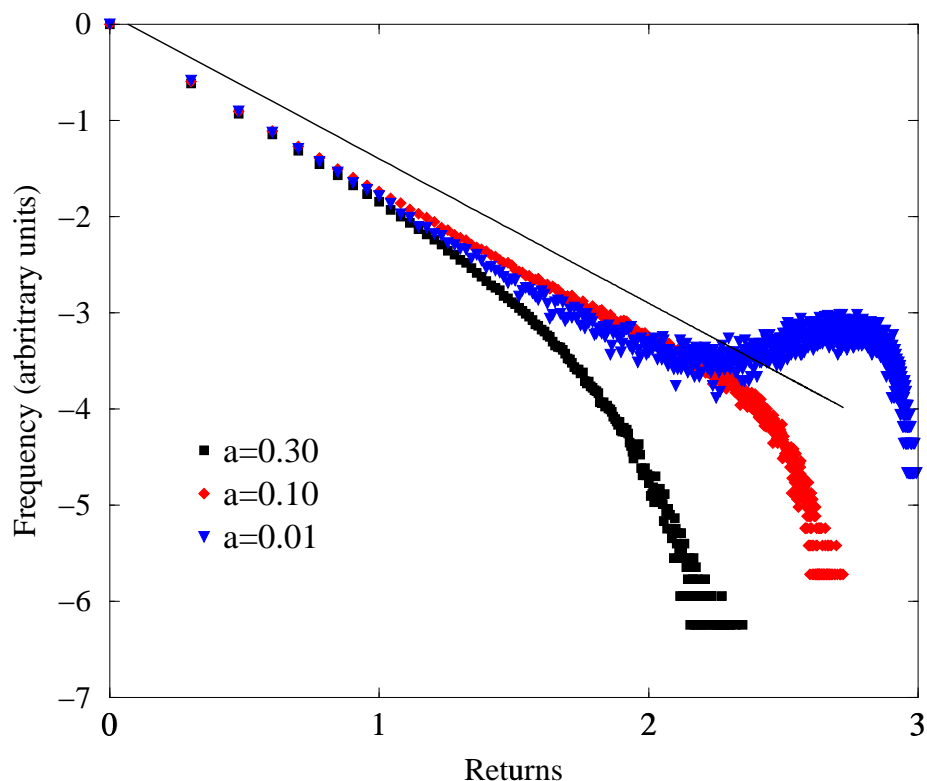


Figure 7.2: Log-log plot of the distribution (in arbitrary units) of returns R for different herding parameters (squares) $a = 0.30$, (diamond) $a = 0.10$, and (triangle) $a = 0.01$. The solid line shows a power-law R^α with exponent $\alpha = -1.5$.

cases one observes power-law decay in a range of returns. For sufficiently small a 's, a relative increase in the probability of extremely high returns is observed, giving a significant weight to “large” events of the order of the system size. In this case the time-average $c(t)$ lies very close to the critical threshold. Decreasing a there is a continuous crossover to an exponential cut-off, where the time average $c(t)$ is far from c^* . We conjecture there is an intermediate value of a where a power-law will be fitted for the whole range.

The distribution of returns is related in this model to the distribution of cluster. In fact, if β is the exponent for the distribution of cluster sizes and α is the exponent for the distribution of returns, then the distribution of returns is equal to the distribution of cluster times the probability to chose a given cluster that is proportional to its size: $\text{prob}(R) \approx R^{-\alpha} \approx ss^{-\beta}$. Heuristically, the exponents are related by $\alpha = \beta - 1$. We plot in Fig. (7.3) the averaged distribution of clusters. The solid line represents a power law with exponent $\beta = 2.5$. This result agree with the previous calculation and with theoretical results on stationary random graphs that predict an exponent of $5/2$ at the critical point [145]. Recently, this exponent was found by D’Hulst and

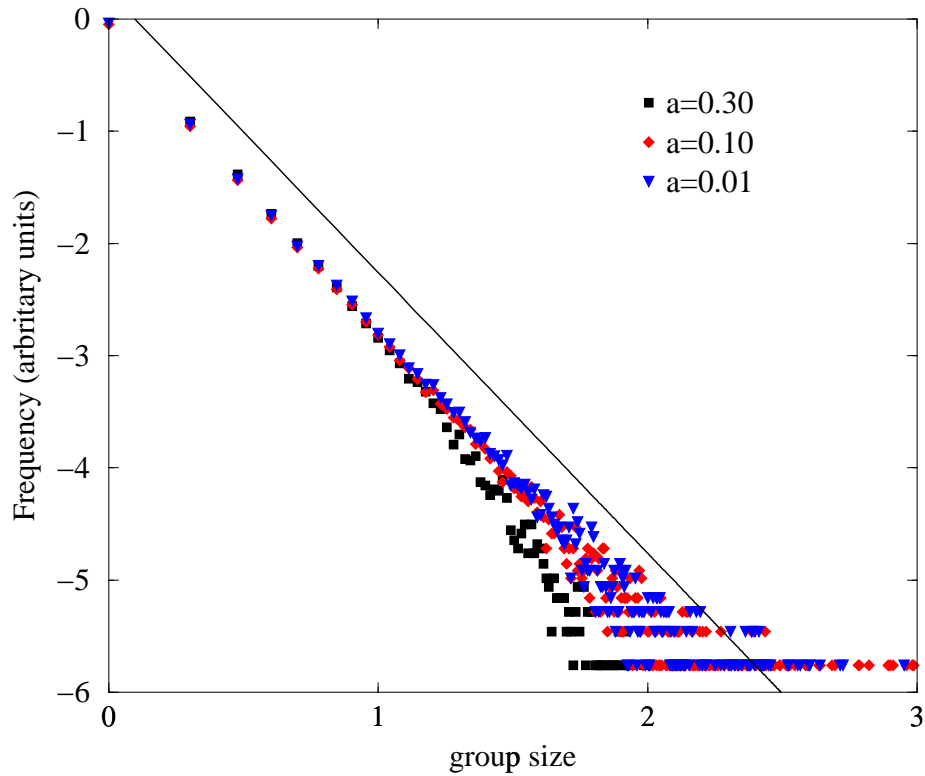


Figure 7.3: Log-log plot of the averaged distribution of cluster sizes for (squares) $a = 0.30$, (diamond) $a = 0.10$ and (triangle) $a = 0.01$. Solid line shows a power law $s^{-\beta}$ with exponent $\beta = 2.5$.

Rodgers [148] in a mean-field analysis of our model². They also extended the model by allowing multiple rumors to be dispersed at a single time-step, finding the exponent is robust.

7.5 Discussion.

Recently Stauffer & Sornette [149] proposed a similar herding model inspired also in Cont & Bouchaud [145], in order to account for a fluctuating connectivity. First they consider a site-percolation model, where agents sit on a lattice with possibly empty sites. Next they propose a mechanism which randomly “sweeps” the connectivity parameter c . This mechanism effectively works to produce a fluctuating connectivity and still have the desired distributions. We, however, try to focus in giving a simple basis for the origin of these fluctuations, based on the information the traders might be handling.

²The analysis presented in [148] does not reproduce the transition shown in Fig. (7.2). in our opinion, this is because they forget a term in their evolution equation

It is interesting to compare the approach to bounded rationality present in our traders, to that of the multi-agent models [141, 142] based on the interaction of two distinct agents populations, the so-called “noisy” and “fundamentalists” traders. While the former group tries to make short term capital gains based on the actual trend of the price of the asset, the latter group uses an estimation of the fundamental value of the asset to decide on his future actions. This estimation arises from a continuous random exogenous source, which simulates the news arrival process [142]. It has been observed [141] that using a single population of “noisy” traders the returns do not exhibit the expected power-laws regimes. It is only when both populations interact, that the universal features are achieved. Our agents population, instead, comes as a hybrid population between “noisy” and “fundamentalist” traders. On the one hand they are “noisy” in the sense they may symmetrically buy or sell, without any fundamental estimation of the assets value. On the other hand the rumor aging process may arise due to an external source of information, as for the “fundamentalist” traders.

Also in these multi-agents models [141, 142] it has been reported that at times where large variations in the price are observed, most of the traders belong to the “noisy” population. The small remaining “fundamentalist” are needed to recover the market after large crashes, for they will surely buy when the price has collapsed. It is not difficult to incorporate this effect in our description, by adding a feedback mechanism between the actual price trend and the rumors the agents have. In this way it may be possible to model a financial market with a single agents population which behaves responding to the information network.

Our approach to model herding behavior has several open modifications worth mentioning:

- At this stage of the model, there is no acceleration mechanism for the price by which “speculative bubbles” may form [150]. We could relax the assumption of a sequential addition of a single rumor, and instead let a fraction of the agents of a cluster disperse his opinion on the same time step. There would be clearly an acceleration of the rumor dispersal as the size of the cluster increases, which could modify the statistics of the returns.
- Also at times when a rumor ages, one could consider that only a fraction r of the traders in the chosen cluster will be impatient enough, drop their links and trade. Note that for a initially random network the limit $r = 0$ and $a = 1$ would contain the CB model exactly. We have numerically studied the case $r = 1/s$, where s is the size of the chosen cluster, and found that the distribution of cluster sizes has the same behavior as in figure...
- Also one can include a global parameter which controls the mood (“optimistic” or “pessimistic”) of the market, similar to Lux & Marchesi [142]. Consider a single agent or cluster which is receiving a dispersed rumor. If the global market is optimistic one would most probably adopt the receiving rumor. Otherwise if the global market is pessimistic, then he may choose the contrary opinion and not merge.

- A more realistic handling of the merging of clusters would be desirable. For example one could consider the process by which when two clusters merge, the one who adopts the others opinion will be fragmented in smaller clusters, because the new incoming opinion is not welcomed. This could be done by introducing a new parameter f , which would correspond to the fraction of links destroyed in the cluster. If the cluster had a very high connectivity, this would correspond to strong believe in their opinion and would be harder to fragment it.

We have presented a model for the propagation of information in a financial market, based on the formalization by Cont & Bouchaud [145] of the herding behaviour. We suppose that the propagation of information within the network follows a random process, and the traders can be classified into groups (clusters) having the same opinion. In our description the size and number of clusters evolves in time reflecting the information content of the market. This is controlled by the rate of rumor dispersal $1/a$. For high rumor speed, herding behavior is very strong and the probability of creation of a large cluster becomes notoriously high, leaving the system in a highly propensive state for crashes to occur. However for low rumor speed, the market always behaves with larger than normally distributed returns, but otherwise exponential tails.

Appendix A

Numerical simulations in arbitrary domains

In this Appendix I describe the numerical code used to solve the time evolution of the complex field $A(\mathbf{x}, t)$ in the complex Ginzburg-Landau equation in two dimensions for general geometries with null Dirichlet boundary conditions.

The CGLE can be written in the following way

$$\partial_t A = A + (1 + i\alpha)\nabla^2 A - (1 + i\beta)|A|^2 A \quad (\text{A.1})$$

where $A(\mathbf{x}, t)$ is a two-dimensional complex field, and α, β are real parameters. The evolution equation is defined inside the two-dimensional domain of integration \mathcal{D} . The specification of the boundary conditions is necessary to have a full description of the problem. Typical boundary conditions are *periodic*, *Dirichlet* and *Neumann* boundary conditions. Periodic boundary conditions imply the equivalence of the ending points, and a rectangular domain subjected to periodic boundary conditions is equivalent to solve the problem in a torus. Neumann boundary conditions consist in giving the value of the normal derivative (e.g. null derivative) of the field at the boundary, and it can take other names as null flux boundary conditions (if the derivative is zero). Finally, Dirichlet boundary conditions indicates that the value of the field at the boundary is known. Thus, null Dirichlet boundary conditions indicate that the value of the field is zero at the boundary. More complicated boundary conditions can be specified. However, in this Appendix, I will focus on null Dirichlet boundary conditions in general geometries (see Fig. A.1).

The first step is to discretize the space using a rectangular grid. In the following I assume that the discretization in both spatial dimensions is the same $\Delta x = \Delta y$. If the discretizations are different some of the formulas used below need to be rewritten. Each point in the lattice can be written in the form $P_{i,j} = P(i\Delta x, j\Delta y)$, and the value of the field in that point $A_{i,j} = A(i\Delta x, j\Delta y, t)$. Thus the Laplacian takes the discrete form

$$(\nabla^2 A)_{i,j} = \frac{A_{i+1,j} + A_{i,j+1} + A_{i-1,j} + A_{i,j-1} - 4A_{i,j}}{(\Delta x)^2} . \quad (\text{A.2})$$

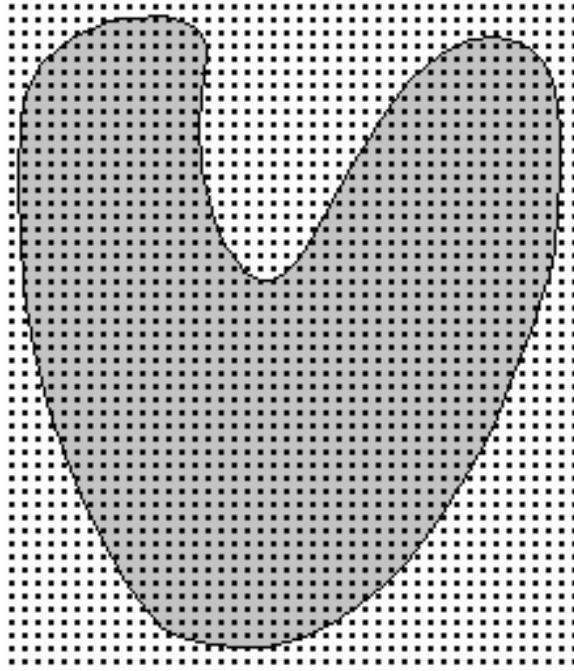


Figure A.1: Domain of integration is the shaded region. The lattice points that are inside the domain (i.e. in the shaded region) will follow the evolution equation (A.1); lattice points outside the domain will remain at value zero $A = 0$.

The discrete version of the complex Ginzburg-Landau equation takes the form

$$\partial_t R_{i,j} = R_{i,j} + \nabla^2 R_{i,j} - \alpha \nabla^2 I_{i,j} - (R_{i,j}^2 + I_{i,j}^2)(R_{i,j} - \beta I_{i,j}) \quad (\text{A.3})$$

$$\partial_t I_{i,j} = I_{i,j} + \nabla^2 I_{i,j} + \alpha \nabla^2 R_{i,j} - (R_{i,j}^2 + I_{i,j}^2)(I_{i,j} + \beta R_{i,j}) \quad (\text{A.4})$$

where $R(\mathbf{x}, t)$ and $I(\mathbf{x}, t)$ are the real and imaginary part of the complex field $A(\mathbf{x}, t)$.

Equations (A.3) and (A.4) are solved using a Runge-Kutta method.

The method explained above will work properly (with the correct time and space discretization) in a rectangular domain with periodic boundary conditions where the ending points connect.

Let's first study the case of a rectangular domain with the field zero at the boundaries. In this case the equation is discretized in the same way for all the internal points. The points that belong to the boundary are simply fixed to zero, $A_{i,j} = 0$, for all $P_{i,j}$ that belong to the boundary.

In the case of a boundary that does not fit in a rectangular grid, we proceed in the following way. Take the domain and superimpose a rectangular lattice with the appropriate spacing. All the points that are inside the domain, *internal*, will follow the evolution equations (A.3)-(A.4). However, the points that are at the boundary or outside the domain will remain fixed to zero, as in the previous case of a rectangular domain with null Dirichlet boundary conditions. In this way, what we are doing is to approximate the boundary by rectangular mosaics. In order to have an accurate solution, we should have a good resolution of the boundary.

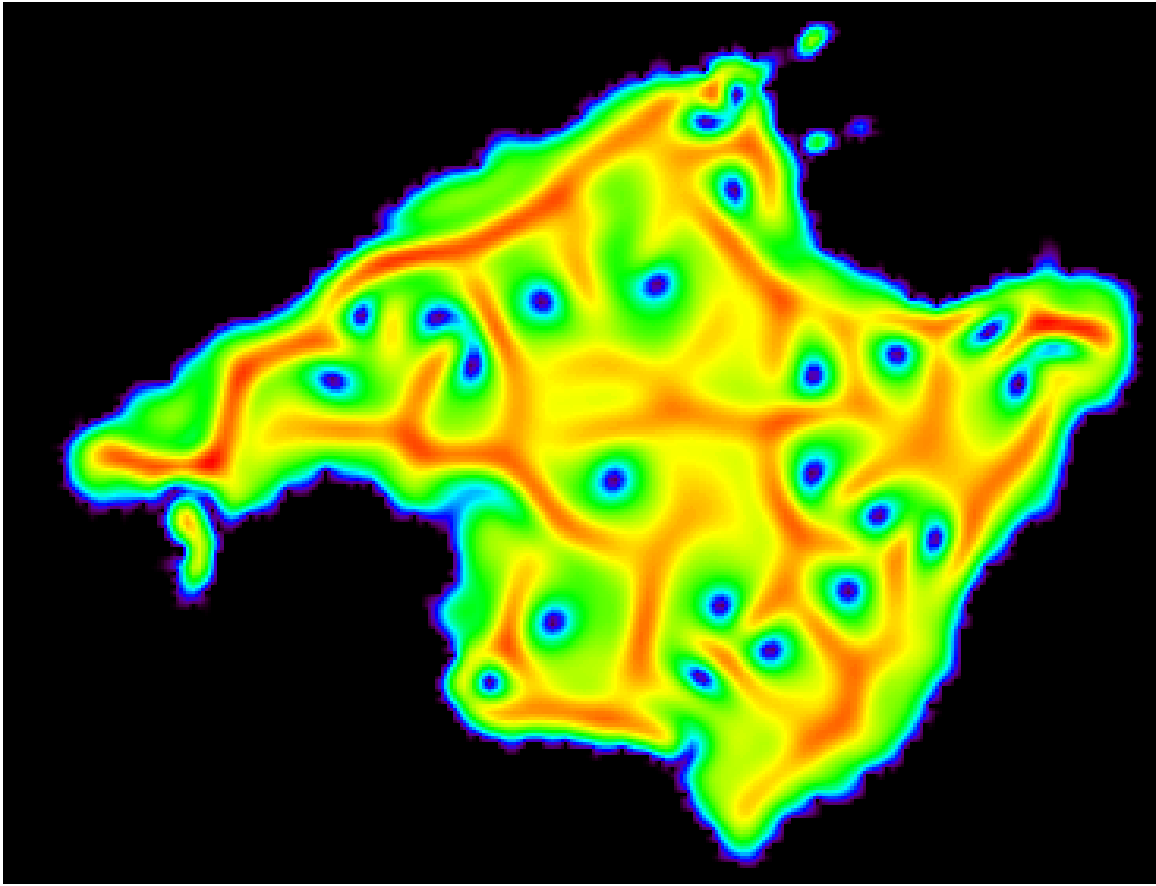


Figure A.2: Snapshot of the modulus of the complex field under the time evolution of the CGLE in a domain with the shape of the Majorca Island with Dirichlet boundary conditions. Color scale runs from black (minimum) to red (maximum).

With this method we can solve the evolutionary equation for any geometry and for Null Dirichlet boundary conditions.

As an example of the flexibility of our approach we show in Fig. (A.2) a simulation of the CGLE in a domain with the shape of the Majorca Island with Dirichlet boundary conditions.

Bibliography

- [1] H.K. Dunn and S.D. White, ‘Statistical measurements on conventional speech’, *J. Acoust. Soc. Am.* **11**, 278–288 (1940).
- [2] C.D. Geisler, in *From sound to synapse*, Oxford University Press, New York (1998).
- [3] Y. Choe, M.O. Magnasco, and J. Hudspeth, ‘A model for amplification of hair-bundle motion by cyclical binding of Ca^{2+} to mechanoelectrical-transduction channels’, *Proc. Natl. Acad. Sci. USA* **95**, 15321–15326 (1998).
- [4] T. Gold, ‘The physical basis of the action of the cochlea’, *Proc. Roy. Soc. B* **135**, 492–498 (1948).
- [5] J.H.E. Cartwright, D. González, and O. Piro, ‘Nonlinear dynamics of the perceived pitch of complex sounds’, *Phys. Rev. Lett.* **82**, 5389–5392 (1999).
- [6] A.J. Hudspeth, ‘The hair cells of the inner ear’, *Sci. Am.* **248**, 54–64 (1983).
- [7] C.-J. Yu, A.G. Richter, A. Datta, M.K. Durbin, and P. Dutta, ‘Observation of molecular layering in thin liquid films using X-ray reflectivity’, *Phys. Rev. Lett.* **82**, 2326 (1999).
- [8] J. Koplik, J. Banavar, and J.F. Willemsen, ‘Molecular dynamics of fluid flow at solid surfaces’, *Phys. Fluids A* **1**, 781–794 (1989).
- [9] B.J. Gluckman, P. Marcq, J. Bridger, and J.P. Gollub, ‘Time averaging of chaotic spatiotemporal wave patterns’, *Phys. Rev. Lett.* **71**, 2034–2037 (1993).
- [10] T. Bohr, M.H. Jensen, G. Paladin, and A. Vulpiani, in *Dynamical systems approach to turbulence*, Cambridge University Press, Cambridge (1998).
- [11] H.L.F. Helmholtz, in *On the Sensations of Tone as a Physiological Basis for the Theory of Music*, Dover Publications, New York (1954).
- [12] G. von Békésy, in *Experiments in Hearing*, McGraw-Hill Book Co., New York (1960).
- [13] M.A. Ruggero and N.C. Rich, ‘Furosemide Alters Organ of Corti Mechanics: Evidence for Feedback of Outer Hair Cells upon the Basilar Membrane’, *J. Neurosci.* **11**, 1057 (1991).

- [14] M.A. Ruggero, 'Responses to sound of the basilar membrane of the mammalian cochlea', *Curr. Opin. Neurobiol.* **2**, 449–456 (1992).
- [15] M.A. Ruggero, L. Robles, and N.C. Rich, 'Two-Tone Suppression in the Basilar Membrane of the Cochlea: Mechanical Basis of Auditory-Nerve Rate Suppression', *J. Neurophysiol.* **68**, 1087 (1992).
- [16] F. Jaramillo, V.S. Markin, and A.J. Hudspeth, 'Auditory illusions and the single hair cell', *Nature* **364**, 527–529 (1993).
- [17] D.L. González and O. Piro, 'Chaos in a nonlinear driven oscillator with exact solution', *Phys. Rev. Lett.* **50**, 870 (1983).
- [18] G.A. Cecchi, D.L. González, M.O. Magnasco, G.B. Mindlin, O. Piro, and A. Santillan, 'Periodically kicked hard oscillators', *Chaos* **3**, 51–62 (1993).
- [19] V.M. Eguíluz, in preparation.
- [20] A.C. Crawford and R. Fettiplace, 'The frequency selectivity of auditory nerve fibres and hair cells in the cochlea of the turtle', *J. Physiol.* **306**, 79–125 (1980).
- [21] A.J. Hudspeth and R.S. Lewis, 'Kinetic analysis of voltage- and ion-dependent conductances in saccular hair cells of the bull-frog, *Rana Catesbeiana*', *J. Physiol.* **400**, 237–274 (1988).
- [22] A.J. Hudspeth and R.S. Lewis, 'A model for electrical resonance and frequency tuning in saccular hair cells of the bull-frog, *Rana Catesbeiana*', *J. Physiol.* **400**, 275–297 (1988).
- [23] A. Neiman, X. Pei, D. Russell, W. Wojtenek, L. Wilkens, F. Moss, H. A. Braun, M.T. Huber, and K. Voigt, 'Synchronization of the noisy electrosensitive cells in the paddlefish', *Phys. Rev. Lett.* **82**, 660–663 (1999).
- [24] A.C. Crawford and R. Fettiplace, 'The mechanical properties of ciliary bundles of turtle cochlear cells', *J. Physiol.* **364**, 359–379 (1985).
- [25] J. Howard and A.J. Hudspeth, 'Mechanical relaxation of the hair bundle mediates adaptation in mechano-electrical transduction by the bullfrog's saccular hair cell', *Proc. Natl. Acad. Sci. USA* **84**, 3064–3068 (1987).
- [26] M.E. Benser, R.E. Marquis, and A.J. Hudspeth, 'Rapid, active hair bundle movements in hair cells from the bullfrog's sacculus', *J. Neurosci.* **16**, 5629–5643 (1996).
- [27] A.J. Hudspeth, 'Mechanical amplification of stimuli by hair cells', *Curr. Opin. Neurobiol.* **7**, 480–486 (1997).
- [28] A.J. Ricci, Y.-C. Wu, and R. Fettiplace, 'The endogenous calcium buffer and the time course of transducer adaptation in auditory hair cells', *J. Neurosci.* **18**, 8261 (1998).

- [29] W. E. Brownell, C. R. Bader, D. Bertrand, and Y. de Ribaupierre, 'Evoked mechanical responses of isolated cochlear outer hair cells', *Science* **227**, 194–196 (1985).
- [30] J.F. Ashmore, 'A fast motile response in guinea-pig outer hair cells: the cellular basis of the cochlear amplifier', *J. Physiol.* **388**, 323–247 (1987).
- [31] C. Kitiyakara and N.J. Guzman, 'Malignant Hypertension and Hypertensive Emergencies', *J. Am. Soc. Nephrol.* **9**, 133 (1998).
- [32] F. Gustafsson, 'Hypertensive arteriolar necrosis revisited', *Blood Pressure* **6**, 71–77 (1997).
- [33] F.B. Byrom, *Lancet* **2**, 201 (1954).
- [34] F.B. Byrom, *Prog. Cardiovasc. Dis.* **1**, 31 (1974).
- [35] J. Giese, *Acta Pathol. Microbiol. Scand.* **62**, 497 (1964).
- [36] J. Giese, in *The Pathogenesis of Hypertensive Vascular Disease*, Munksgaard, Copenhagen (1966).
- [37] L.J. Beilin and F.S. Goldby, *Clin. Sci. Mol. Med.* **52**, 111 (1977).
- [38] G.A. Meininger, K.L. Fehr, M.B. Yates, J.L. Borders, and H.J. Granger, *Hypertension* **8**, 66 (1986).
- [39] Y.C. Fung, in *Biomechanics. Mechanical Properties of Living Tissues*, Springer-Verlag, New York (1990).
- [40] Y.C. Fung, in *Biomechanics. Motion, Flow, Stress, and Growth*, Springer-Verlag, New York (1990).
- [41] J. Plateau, in *Statique Experimentale et Theorique des Liquides Soumis aux Seules Forces Moleculaires*, Gautier-Villars, Paris (1873).
- [42] Lord Rayleigh, 'On the instability of a cylinder of viscous liquid under capillary force', *Philos. Mag.* **34**, 145–154 (1892).
- [43] R. Bar-Ziv and E. Moses, 'Instability and "pearling" states produced in tubular membranes by competition of curvature and tension', *Phys. Rev. Lett.* **73**, 1392–1395 (1994).
- [44] P. Nelson and T. Powers, 'Dynamical Theory of the Pearling Instability in Cylindrical Vesicles', *Phys. Rev. Lett.* **74**, 3384–3387 (1996).
- [45] R.E. Goldstein, P. Nelson, T. Powers, and U. Seifert, 'Front propagation in the pearling instability of tubular vesicles', *J. Phys. II France* **6**, 767 (1996).
- [46] R.W. Gore, *Circ. Res.* **34**, 581 (1974).

- [47] M.J. Davis and R.W. Gore, ‘Length-tension relationship of vascular smooth muscle in single arterioles’, *Am. J. Physiol.* **256**, H630–H640 (1989).
- [48] R. Feldberg, M. Colding-Jørgensen, and N.-H. Holstein-Rathlou, ‘Analysis of interaction between TGF and the myogenic response in renal blood flow autoregulation’, *Am. J. Physiol.* **269**, F581–F593 (1995).
- [49] H. Bai-Lin, in *Chaos*, World Scientific, Singapore (1990).
- [50] E. Ott, in *Chaos in dynamical systems*, Cambridge University Press, Cambridge (1993).
- [51] K. Alligood, T. Sauer, and J.A. Yorke, in *Chaos: an introduction to dynamical systems*, Springer Verlag, New York (1997).
- [52] M.C. Cross and P.C. Hohenberg, ‘Spatiotemporal chaos’, *Science* **263**, 1569–1570 (1994).
- [53] M.C. Cross and P.C. Hohenberg, ‘Pattern formation outside of equilibrium’, *Rev. Mod. Phys.* **65**, 851–1112 (1993).
- [54] P. Couillet, C. Elphick, and D. Repaux, ‘Nature of spatial chaos’, *Phys. Rev. Lett.* **58**, 431–434 (1987).
- [55] M.I. Rabinovich, A.L. Fabrikant, and L.Sh. Tsimring, ‘Finite dimensional spatial disorder’, *Sov. Phys. Usp.* **35**, 629 (1992).
- [56] R. Montagne, E. Hernández-García, and M. San Miguel, ‘Winding Number Instability in the Phase-Turbulence Regime of the Complex Ginzburg-Landau Equation’, *Phys. Rev. Lett.* **77**, 267–270 (1996).
- [57] R. Montagne, E. Hernández-García, A. Amengual, and M. San Miguel, ‘Wound-up phase turbulence in the complex Ginzburg-Landau equation’, *Phys. Rev. E* **56**, 151–167 (1997).
- [58] H.-C. Chang, ‘Wave evolution on a falling film’, *Annu. Rev. Fluid Mech.* **26**, 103–136 (1994).
- [59] C. Elphick, E. Meron, and E.A. Spiegel, ‘Spatiotemporal complexity in traveling patterns’, *Phys. Rev. Lett.* **61**, 496–499 (1988).
- [60] C. Elphick, E. Meron, and E.A. Spiegel, ‘Patterns of Propagating Pulses’, *SIAM J. Appl. Math.* **50**, 490 (1990).
- [61] C. Elphick, E. Meron, J. Rinzel, and E.A. Spiegel, ‘Impulse Patterning and Relaxational Propagation in Excitable Media’, *J. Theor. Biol.* **146**, 249 (1990).
- [62] N.J. Balmforth, ‘Solitary waves and homoclinic orbits’, *Annu. Rev. Fluid Mech.* **27**, 335–373 (1996).

- [63] D. Ruelle, ‘Five turbulent problems’, *Physica D* **7**, 40–44 (1983).
- [64] A.C. Newell and Y. Pomeau, ‘Turbulent crystals in macroscopic systems’, *J. Phys. A* **26**, L429 (1993).
- [65] P. Bak, ‘Commensurate phases, incommensurate phases and the devil’s staircase’, *Rep. Prog. Phys.* **45**, 587–629 (1982).
- [66] M. Lowe, J.P. Gollub, and T.C. Lubensky, ‘Commensurate incommensurate structures in a nonequilibrium system’, *Phys. Rev. Lett.* **51**, 786 (1983).
- [67] M. Lowe, B.S. Albert, and J.P. Gollub, *J. Fluid Mech.* **173**, 253 (1986).
- [68] P. Coulet, ‘Commensurate-incommensurate transition in nonequilibrium systems’, *Phys. Rev. Lett.* **56**, 724–727 (1986).
- [69] S.W. Jones, O.M. Thomas, and H. Aref, ‘Chaotic advection by laminar flow in a twisted pipe’, *J. Fluid Mech.* **209**, 335–357 (1989).
- [70] Y. LeGuer, C. Castelain, and H. Peerhossaini, Experimental study of chaotic advection in a twisted duct flow, unpublished.
- [71] J.H.E. Cartwright, M. Feingold, and O. Piro, ‘An introduction to chaotic advection’, in *Mixing: chaos, and turbulence*, H. Chaté and E. Villermaux Eds., Kluwer, Dordrecht (1999).
- [72] E. Hernández-García, M. San Miguel, R. Toral, and J. Viñals, ‘Noise and pattern selection in the one-dimensional Swift-Hohenberg equation’, *Physica D* **61**, 159–165 (1992).
- [73] K.A. Gorskov, L.N. Korzinov, M.I. Rabinovich, and L.S. Tsimring, ‘Random pinning of localized states and the birth of deterministic disorder within gradient models’, *J. Stat. Phys.* **74**, 1033–1045 (1994).
- [74] M.A. Malkov, ‘Spatial chaos in weakly dispersive and viscous media: a non-perturbative theory of the driven KdV-Burgers equation’, *Physica D* **95**, 62–80 (1996).
- [75] V.S. Afraimovich, A.B. Ezersky, M.I. Rabinovich, M.A. Shereshevsky, and A.L. Zheleznyak, ‘Dynamical description of spatial disorder’, *Physica D* **58**, 331–338 (1992).
- [76] J.D. Gunton, M. San Miguel, and P.S. Sahni, ‘The dynamics of first order phase transitions, in *Phase transitions and critical phenomena*, Academic Press, New York (1983).
- [77] J.D. Murray, in *Mathematical Biology*, Springer Verlag, Berlin (1993).

- [78] R. Montagne, E. Hernández-García, and M. San Miguel, ‘Numerical study of a Lyapunov functional for the complex Ginzburg-Landau equation’, *Physica D* **96**, 47–65 (1996).
- [79] M. San Miguel, R. Montagne, A. Amengual, and E. Hernández-García, ‘Multiple front propagation in a potential non-gradient system, in *Instabilities and Nonequilibrium Structures V*, E. Tirapegui and W. Zeller Eds., Kluwer Academic Publishers, Dordrecht (1996).
- [80] P. Collet, ‘Thermodynamic limit of the Ginzburg-Landau equations’, *Nonlinearity* **7**, 1175–1190 (1994).
- [81] A. Doelman, W. Eckhaus, R. Kuske, and R. Schillen, ‘Nonlinear dynamics and pattern formation in the natural environment, in *Pattern formation in systems on spatially periodic domains*, A. Doelman and A. van Harten Eds., Longman, (1995).
- [82] A.H. Nayfeh and B. Balachandran, in *Applied nonlinear dynamics*, Wiley-Interscience, New York (1995).
- [83] H. Poincaré, in *Mémoire sur les courbes définies par les équations différentielles I-IV, Oeuvre I*, Gauthier-Villar, Paris (1880-1890).
- [84] H. Poincaré, ‘Sur les équations de la dynamique et le problème de trois corps’, *Acta Math.* **13**, 1–270 (1890).
- [85] H. Poincaré, in *Les methodes nouvelles de la mecanbique celeste*, Gauthier-Villar, Paris (1899).
- [86] E. Lorenz, ‘Deterministic nonperiodic flow’, *J. Atmos. Sci.* **20**, 130–141 (1963).
- [87] D. Ruelle and F. Takens, ‘On the nature of turbulence’, *Comm. Math. Phys.* **20**, 167–192 (1971).
- [88] H.D.I. Abarbanel, R. Brown, J.J. Sidorowich, and L.S. Tsimring, ‘The analysis of observed data in physical systems’, *Rev. Mod. Phys.* **65**, 1331 (1993).
- [89] M. Dellnitz, M. Golubitsky, and I. Melbourne, ‘Mechanisms of symmetry creation’, in *Bifurcation and symmetry*, pag. 99–109, Birkhäuser Verlag, Basel (1992).
- [90] V.M. Eguíluz, P. Alstrøm, E. Hernández-García, and O. Piro, ‘Average patterns of spatiotemporal chaos: a boundary effect’, *Phys. Rev. E* **59**, 2822–2825 (1999).
- [91] G. Ahlers and R.P. Behringer, ‘The Rayleigh-Bénard instability and the evolution of turbulence’, *Prog. Theor. Phys. Supp.* **64**, 186 (1978).
- [92] S. Ciliberto and P. Bigazzi, ‘Spatio-temporal intermittency in Rayleigh-Bénard convection’, *Phys. Rev. Lett.* **60**, 286 (1988).

- [93] F. Daviaud, M. Bonetti, and M. Dubois, 'Transition to turbulence via spatio-temporal intermittency in one-dimensional Rayleigh-Bénard convection', *Phys. Rev. A* **42**, 3388 (1990).
- [94] F. Zhong, R. Ecke, and V. Steinberg, 'Rotating Rayleigh-Bénard convection: the Küpers-Lortz transition', *Physica D* **51**, 596 (1991).
- [95] Q. Ouyang and H.L. Swinney, 'Transition to chemical turbulence', *Chaos* **1**, 411 (1991).
- [96] J.P. Gollub and R. Ramshankar, 'Spatio-temporal chaos in interfacial waves', in *New perspectives in turbulence*, pag. 165, Springer-Verlag, New York (1991).
- [97] N.B. Tuffillaro, R. Ramshankar, and J.P. Gollub, 'Order-disorder transition in capillary ripples', *Phys. Rev. Lett.* **62**, 422 (1989).
- [98] E. Braun, S. Rasenat, and V. Steinberg, 'The mechanism of transition to weak turbulence in extended anisotropic systems', *Europhys. Lett.* **15**, 597 (1991).
- [99] S. Nasuno, S. Takeuchi, and Y. Sawada, 'Motion and interaction of dislocations in electrohydrodynamic convection of nematic liquid crystals', *Phys. Rev. A* **40**, 3457 (1989).
- [100] I. Rehberg, S. Rasenat, and V. Steinberg, 'Travelling waves and defect-initiated turbulence in electroconvecting nematics', *Phys. Rev. Lett.* **62**, 756 (1989).
- [101] M. Dennin, G. Ahlers, and D.S. Cannell, 'Spatiotemporal Chaos in Electroconvection', *Science* **272**, 388 (1996).
- [102] P. Kolodner, J.A. Glazier, and H. Williams, 'Dispersive chaos in one-dimensional travelling-wave convection', *Phys. Rev. Lett.* **65**, 1579 (1990).
- [103] V. Steinberg, J. Fineberg, E. Moses, and I. Rehberg, 'Pattern selection and transition to turbulence in propagating waves', *Physica D* **37**, 359 (1989).
- [104] M. Rabaud, S. Michalland, and Y. Couder, 'Dynamical regimes of directional viscous fingering: spatio-temporal chaos and wave propagation', *Phys. Rev. Lett.* **64**, 184 (1990).
- [105] J.J. Hegseth, S.D. Andereck, F. Hayot, and Y. Pomeau, 'Spiral turbulence and phase dynamics', *Phys. Rev. Lett.* **62**, 257 (1989).
- [106] P.C. Hohenberg and B. Shraiman, 'Chaotic behavior of an extended system', *Physica D* **37**, 109 (1989).
- [107] E. Bosch, H. Lambermont, and W. van de Water, 'Average patterns in Faraday waves', *Phys. Rev. E* **49**, R3580–R3583 (1994).
- [108] L. Ning, Y. Hu, R.E. Ecke, and G. Ahlers, 'Spatial and temporal averages in chaotic patterns', *Phys. Rev. Lett.* **71**, 2216–2219 (1993).

- [109] S. Rudroff and I. Rehberg, ‘Pattern formation and spatiotemporal chaos in the presence of boundaries’, *Phys. Rev. E* **55**, 2742–2749 (1997).
- [110] P. Chossat and M. Golubitsky, ‘Symmetry-increasing bifurcation of chaotic attractors’, *Physica D* **32**, 423–436 (1988).
- [111] M. Dellnitz, M. Golubitsky, and I. Melbourne, ‘The structure of symmetric attractors’, *Arch. Rat. Mech. Anal.* **123**, 75 (1993).
- [112] P. Colet, M. San Miguel, M. Brambilla, and L.A. Lugiato, ‘Fluctuations in transverse laser patterns’, *Phys. Rev. A* **43**, 3862–3876 (1991).
- [113] C.B. Arnold, B.J. Bluckman, and J.P. Gollub, ‘Statistical Averages of Chaotically evolving patterns’, in *Spatio-temporal patterns*, pag. 545, Addison-Wesley, (1995).
- [114] M. Faraday, ‘On the forms and states assumed by fluids in contact with vibrating-elastic surfaces’, *Philos. Trans. R. Soc. London* **52**, 319 (1831).
- [115] Lord Rayleigh, ‘On the crispations of fluid resting upon a vibrating support’, *Phil. Mag.* **16**, 50 (1883).
- [116] T.B. Benjamin and F. Ursell, *Proc. R. Soc. London, Ser. A* **225**, 505 (1954).
- [117] B.J. Gluckman, C.B. Arnold, and J.P. Gollub, ‘Statistical studies of chaotic wave patterns’, *Phys. Rev. E* **51**, 1128 (1995).
- [118] W.S. Edwards and S. Fauve, ‘Patterns and quasi-patterns in the Faraday experiment’, *J. Fluid Mech.* **278**, 123–148 (1994).
- [119] P. Chen and J. Viñals, ‘Pattern Selection in Faraday Waves’, *Phys. Rev. Lett.* **79**, 2670 (1997).
- [120] W. Merzkirch, in *Flow visualization*, Academic, Orlando (1987).
- [121] Y. Kuramoto and T. Tsuzuki, ‘Persistent propagation of concentration waves in dissipative media far from thermal equilibrium’, *Prog. Theor. Phys.* **55**, 356 (1976).
- [122] G.I. Sivashinsky and D.M. Michelson, *Prog. Theor. Phys.* **63**, 2112 (1980).
- [123] G.I. Sivashinsky, ‘Instabilities, pattern formation, and turbulence in flames’, *Ann. Rev. Fluid Mech.* **15**, 179–199 (1983).
- [124] M. Gorman, private communication.
- [125] G.I. Sivashinsky, ‘Nonlinear analysis of hydrodynamic instability in laminar flames. Part I. Derivation of basic equations’, *Acta Astronautica* **4**, 1177 (1977).
- [126] S. Zaleski and P. Lallemand, ‘Scaling laws and intermittency in phase turbulence’, *J. Phys. Lett. (Paris)* **46**, L793–L797 (1985).

- [127] D.A. Egolf and H.S. Greenside, 'Spatial variation of correlation times for 1D phase turbulence', *Phys. Lett. A* **185**, 395–400 (1994).
- [128] W. van Saarloos, 'The complex Ginzburg-Landau equation for beginners', in *Spatio-temporal patterns in non-equilibrium complex systems*, pag. 19–31, Addison-Wesley, Reading, MA (1994).
- [129] B.I. Shraiman, A. Pumir, W. van Saarloos, M.C. Hohenberg, H. Chaté, and M. Hohen, 'Spatiotemporal chaos in the one-dimensional complex Ginzburg-Landau equation', *Physica D* **57**, 241 (1992).
- [130] H. Chaté, 'Disordered regimes of the one-dimensional complex Ginzburg-Landau equation', in *Spatio-Temporal Patterns in Non-equilibrium Complex Systems*, pag. 33–50, Addison-Wesley, Reading, MA (1994).
- [131] H. Chaté and P. Manneville, 'Phase diagram of the two-dimensional complex Ginzburg-Landau equation', *Physica A* **224**, 348–368 (1996).
- [132] M.C. Cross, P.G. Daniels, P.C. Hohenberg, and E.D. Siggia, 'Effect of distant sidewalls on wave-number selection in Rayleigh-Bénard convection', *Phys. Rev. Lett.* **45**, 898 (1980).
- [133] M.C. Cross, P.G. Daniels, P.C. Hohenberg, and E.D. Siggia, 'Phase-winding solutions in a finite container above the convective threshold', *J. Fluid Mech.* **127**, 155 (1983).
- [134] L. Sirovich, J.D. Rodriguez, and B. Knight, 'Two boundary value problems for the Ginzburg-Landau equation', *Physica D* **43**, 63–76 (1990).
- [135] P.S. Hagan, 'Spiral waves in reaction-diffusion equations', *SIAM J. Appl. Math.* **42**, 762–786 (1982).
- [136] K. Nozaki and N. Bekki, *Phys. Lett. A* **110**, 133 (1985).
- [137] V.M. Eguíluz, E. Hernández-García, and O. Piro, in preparation.
- [138] I.S. Aranson, L. Kramer, and A. Weber, 'Theory of interaction and bound states of spiral waves in oscillatory media', *Phys. Rev. E* **47**, 3231–3241 (1993).
- [139] J.P. Bouchaud and M. Potters, in *Theory of Financial Risk*, Cambridge University Press, (2000).
- [140] R.N. Mantegna and E. Stanley, 'Scaling behavior in the dynamics of an economic index', *Nature* **376**, 46–49 (1995).
- [141] P. Bak, M. Paczuski, and M. Shubik, 'Price variations in a stock market with many agents', *Physica A* **246**, 430–453 (1997).
- [142] T. Lux and M. Marchesi, 'Scaling and criticality in a stochastic multi-agent model of a financial market', *Nature* **397**, 498–500 (1999).

- [143] R. Topol, 'Bubbles and volatility of stock prices: effect of mimetic contagion', *Economic Journal* **101**, 768–800 (1991).
- [144] A. Bannerjee, 'The economics of rumours', *Rev. of Economic Studies* **60**, 309–327 (1993).
- [145] R. Cont and J.P. Bouchaud, 'Herd behavior and aggregate fluctuations in financial markets', *Macroeconomic Dynamics*, in press (1999).
- [146] J.D. Farmer, 'Market force, ecology and evolution', preprint adap-org/9812005 (1998).
- [147] Y.-C. Zhang, 'Toward a theory of marginally efficient markets', *Physica A* **269**, 30–44 (1998).
- [148] R. D'Hulst and G.J. Rodgers, 'Exact solution for a model of crowding and information transmission in a financial markets', preprint cond-mat/9908481 (1999).
- [149] D. Stauffer and D. Sornette, 'Self-organized percolation model for stock market fluctuations', *Physica A* **271**, 496–506 (1999).
- [150] B.M. Roehner and D. Sornette, 'The sharp peak-flat trough pattern and critical speculation', *Eur. Phys. J. B* **4**, 387–399 (1998).

Curriculum Vitae

Víctor Martínez Eguíluz

Date of birth: September 7, 1972

Place of birth: San Sebastián, Spain

Education

- ‘Suficiencia Investigadora’ from the University of the Balearic Islands (Spain), June 1999.
- Degree in Physics, specialization in Solid State Physics, from the University of the Basque Country (Spain), June 1995.

List of Publications

Refereed papers

- *Average patterns of spatio-temporal chaos: a boundary effect*, by V.M. Eguíluz, E. Hernández-García, O. Piro. *Phys. Rev. E* **59**, 2822 (1999).
- *Instability and ‘Sausage-String’ appearance in blood vessels during high blood pressure*, by P. Alstrøm, V.M. Eguíluz, M. Colding-Jørgensen, F. Gustafsson, N.-H. Holstein-Rathlou. *Phys. Rev. Lett.* **82**, 1995 (1999).
- *Boundary effects in the complex Ginzburg-Landau equation* V.M. Eguíluz, E. Hernández-García, O. Piro. Accepted in *Int. J. Bifurcation Chaos* (1999).
- *Dynamics of elastic excitable media*, by J.H.E. Cartwright, E. Hernández-García, V.M. Eguíluz, O. Piro. Accepted in *Int. J. Bifurcation Chaos* (1999).
- *Frozen spatial chaos induced by boundaries*, by V.M. Eguíluz, E. Hernández-García, O. Piro, S. Balle. To appear in *Phys. Rev E* (1999).
- *The complex Ginzburg-Landau equation in the presence of walls and corners*, by V.M. Eguíluz, E. Hernández-García, O. Piro. In preparation.

- *Essential nonlinearities in hearing*, by V.M. Eguíluz, M. Ospeck, Y. Choe, A.J. Husdpth, M.O. Magnasco. Submitted to publication.
- *Self-organized evolution in financial markets*, by V.M. Eguíluz, M.G. Zimmermann. Submitted to publication.
- *Collusive and competitive behavior of firms*, by V.M. Eguíluz, M.G. Zimmermann, A. Spadaro, M. San Miguel. In preparation.

Chapters of books

- *Boundary induced frozen chaos*, by V.M. Eguíluz, E. Hernández-García, O. Piro. In *FISES'97, Proceedings of the VIII Spanish Meeting on Statistical Physics*, J.A. Cuesta and A. Sánchez, eds. Ed. CIEMAT (Madrid, 1998).
- *'Sausage-String' patterns in blood vessels at high blood pressures*, by P. Alstrøm, V.M. Eguíluz, F. Gustafsson, N.-H. Holstein-Rathlou. Accepted in *Proceedings of Statistical Mechanics of Biocomplexity*, Springer Verlag (Berlin, 1999)
- *Boundary-forced spatial chaos*, by V.M. Eguíluz, E. Hernandez-Garcia, O. Piro. Submitted to the *Proceedings of 'Instabilities and Nonequilibrium Structures VII'*, E. Tirapegui and D. Villarroel Eds., Kluwer (Dordrecht, 1999).

Others

- *Cover illustration*, by V.M. Eguíluz, E. Hernández-García, O. Piro. To appear in *Int. J. Bifurcation Chaos* (1999).

- **Press releases:**

The paper "*Instability and 'Sausage-String' appearance in blood vessels during high blood pressure*", *Phys. Rev. Lett.* **82**, 1995 (1999), was the subject of two articles that appeared in the media: (i) one appeared in the News section of the electronic publication **PhysicsWeb** (Institute of Physics) (URL: <http://www.physicsweb.org/>), with the title '*Physics solves blood vessel mystery*', October 16th, 1998; (ii) and in the section **Daily inSight** (Academic Press & Science) (URL: <http://www.academicpress.com>) with the title '*The secret of blood sausages*', March 10th, 1999. (See pags. 39-40)